Hydrodynamics of High Speed Planing Hulls with Partially Ventilated Bottom and Hydrofoils

by

Zvi Sheingart

Bachelor of Science in Mechanical Engineering
Technion Israel,(2002)
Master of Engineering in Mechanical Engineering
Technion Israel,(2006)

Submitted to the Department of Mechanical Engineering
in partial fulfillment of the requirements for the degrees of
Master of Science in Naval Architecture and Marine Engineering
and
Master of Science in Mechanical Engineering
at the
MASSACHUSETTS INSTITUTE OF TECHNOLOGY
February 2014

Author .....
Department of Mechanical Engineering
January 15, 2014

Certified by .....
Chryssostomos Chryssostomidis, Director of MIT Sea Grant
Doherty Professor of Ocean Science and Engineering
Professor of Ocean and Mechanical Engineering
Thesis Supervisor

Certified by .....
Stefano Brizzolara, Assistant Director for Research at MIT Sea Grant
Research Scientist, Department of Mechanical Engineering
Thesis Advisor

Accepted by .....
David E. Hardt
Professor of Mechanical Engineering
Chairman, Departmental Committee on Graduate Students

Hydrodynamics of High Speed Planing Hulls with Partially Ventilated Bottom and Hydrofoils

By
Zvi Sheingart

Submitted to the Department of Mechanical Engineering
on January 15, 2014, in partial fulfillment of the requirements for the degrees of
Master of Science in Naval Architecture and Marine Engineering
and
Master of Science in Mechanical Engineering

Abstract

The influence of a cambered shaped bottom step on the performance of sea going V-stepped planing hulls is investigated using numerical methods. The shape of the step was designed to decrease the Drag/Lift ratio of the hull in full planing regime ($Fr_{\nabla} = 6$). A numerical method, complementary to the existing empirical method developed by Clement for design of a cambered step has been developed. The numerical approach described in this thesis extends the empirical Clement's method for stepped hull design to hard chine hulls with higher deadrise. The stern trim stabilizer has been replaced by supercavitating hydrofoils. Several foil/step configurations were numerically tested. RANSE code is used to evaluate the performance of new hull design with a stepped bottom. Prototypes of the hull have been modeled in 3D using Rhino, NURBS surface modeler. Two validation cases have been considered to validate the RANSE models used for the numerical prediction of hydrodynamic characteristics: Geritsma's 25° deadrise hull series and original Clement's 12.5° deadrise hull (DTMB Model 5115). Numerical results showed good agreement with experimental data, except for the pre-planing regime, where an influence of the towing rig on the CG rise was not negligible. The baseline for the design of the hybrid stepped hull chosen to be Geritsma's 25° hull with length to maximum beam ratio of 4.09.

The thesis confirms the applicability of Clement's method on deep-V seagoing hulls. Total reduction of 3% in Drag/Lift ratio has been achieved, but can be further reduced. All the RANSE calculations were performed using Star-CCM+® software package on the 400 cores HPC cluster of MIT i-Ship lab.

Thesis supervisor: Chryssostomos Chryssostomidis

(Professor of Mechanical and Ocean Engineering)

Acknowledgments

This thesis was written in the Innovative Ship Design Lab, MIT i-Ship during 2013, under the MIT Sea Grant College Program. I would like to express my deepest gratitude to the director of the MIT Sea Grant College Program and my thesis advisor, Professor Chryssostomos Chryssostomidis, for giving me the opportunity and resources to participate in cutting edge research and design of fast planing craft.

I would like to thank Professor Stefano Brizzolara for his guidance and support during this period. His enthusiasm, knowledge and experience provided me the energy and advice to overcome the obstacles to successful completion of the research. Thank you for always being there, it has been a great privilege to work with you.

I am grateful to Captain Mark Thomas and Commander Jerod Ketcham, USN, for their mentorship and guidance during my course of study at MIT. For bringing a broad perspective and practical approach to problem solving, that attitude will accompany my future professional career.

In addition, I would like to thank the Israeli Navy for sponsoring my graduate studies at MIT.

Last but not the least I would like to thank my wife Lena and our sons Yehonathan and Daniel for their unconditional love and support.

This thesis is dedicated to my father, whose leadership lighted my way in difficult times.

Table of Contents

List of Figures

List of Tables

Chapter 1 - Introduction

The maximum speed of seagoing vessels increased significantly during the last century. While the merchant fleets maintain relatively low speeds governed by considerations of economic efficiency (fuel consumption and environmental impact), the special purpose craft are designed to develop maximum speed. The designation of such craft may vary significantly. Whenever recreational craft, offshore supply vessels or patrol interceptor boats are under consideration, the operating envelope at sea is bounded by factors such as survivability to capsizing, ride quality, dynamic stability, structural and power margins [1]. The current section reviews historical development of fast vessels during the past one and a half century in light of emerging technologies applied to propulsion and structural design, and improvements in construction techniques.

The steamer USS Sassacus commissioned during 1863 at Boston Navy Yard developed 14.5 knots with hull length of 205 feet, according to the US Naval History Heritage Command website. Considered a fast ship at the time her non dimensional speed was about Froude number 0.3, which is below the hull speed for a displacement vessel. Thirty four years later (June 19 1897), sea trial results of one of the first documented powerboats to overcome the hull speed were published in *New York Times*. The steam launch 'Ellide' developed 37 knots with a waterline length of 24.4[m]. As can be seen, the hull speed U_H is proportional to hull length and overcoming it indicates transition from displacement to semi-displacement regime. A simplified explanation of why the hull speed was a barrier for surface vessels for many years is presented in [2] and summarized below for two dimensional sinusoidal waves.

A major resistance component for displacement ship is a wave making resistance D_w, given by equation (1.1) with fluid density ρ , gravity constant g and wave amplitude A. Dealing with the two dimensional case, the units of D_w are [N/m].

$$D_w = \frac{1}{4}\rho g A^2 \tag{1.1}$$

Considering simplified case the wave amplitude is a superposition of bow and stern waves given by (1.2). k is a wave number, l is a distance between bow and stern, x is longitudinal coordinate. Amplitude of disturbance waves is assumed to be equal and of magnitude a, amplitude of envelope wave is A:

$$\begin{aligned} &\eta_{bow} + \eta_{stern} = a\cos(kx) - a\cos\left(k\left(x+l\right)\right) \\ &A = \left|\eta_{bow} + \eta_{stern}\right| = 2a\left|\sin\left(kl/2\right)\right| \end{aligned} \tag{1.2}$$

The stationary wave system with respect to the ship is obtained when wave speed is equal to ship's speed U. Dispersion relation in deep water is given by equation (1.3). The second part of

(1.3) represents the dependence between ship length and speed, this equation is well known in its rearranged form as (1.4) when U is expressed in knots and l in feet.

$$U = \sqrt{g/k} \qquad l = \frac{2\pi U^2}{g} \tag{1.3}$$

$$U_H = 1.34\sqrt{l} \tag{1.4}$$

$$D_w \cong \rho g a^2 \sin^2\left(\frac{kl}{2}\right) = \rho g a^2 \sin^2\left(\frac{gl}{2U^2}\right) = \rho g a^2 \sin^2\left(\frac{1}{2Fr_L^{\,2}}\right) \tag{1.5}$$

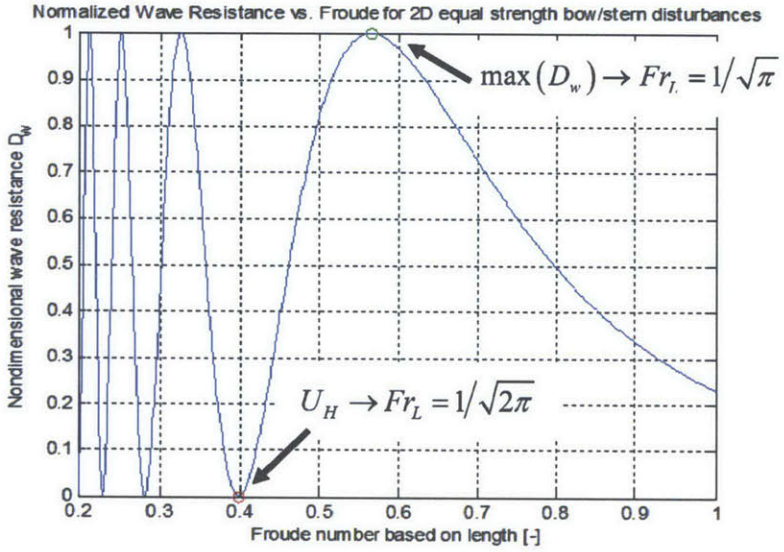

Figure 1. Simplified Wave Resistance variation vs. Fr number - 2D case.

Substituting the first part of (1.3) into (1.2) and then (1.2) into (1.1) one obtains equation (1.5), which links the wave resistance to the Froude number based on ship length.

Dividing D_w with $\rho g a^2$ to convert it to non-dimensional form and examining its behavior as a function of the Froude number as presented in Figure 1, important conclusion may be drawn.

At low Fr_L numbers D_w oscillates rapidly; therfore the waves are short relative to the ship, there are significant wave cancelations and D_w is small. At $Fr_L = 1/\sqrt{2\pi}$ which corresponds to the hull speed U_H, D_w vanishes and then grows rapidly to maximal value at $Fr_L = 1/\sqrt{\pi}$. Obviously in the 3D case wave propagation is more complicated, bow and stern waves have different amplitudes, wave resistance doesn't vanish at a hull speed but the tendency presented above is preserved. Analysis of wave making resistance with respect to the 3D case is covered by [3] and recently slight corrections to the method are suggested by [4].

The simplified example shows that in order to exceed the hull speed by more than 3 times, the steam launch 'Ellide' had to have exceptional hull design to reduce wake and novice propulsion system. Following his success steam boat designer Charles Mosher developed the twin shaft yacht 'Arrow' shown in Figure 2.

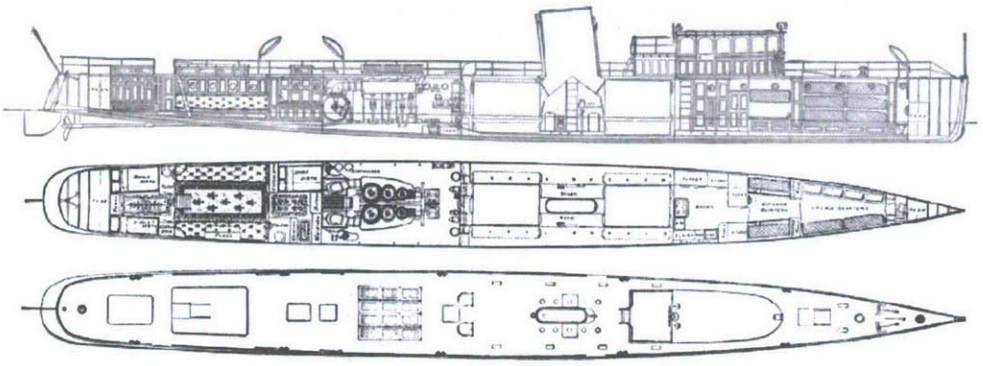

Figure 2. Steamer "Arrow" topside arrangement. (*Scientific American* v.50 1900).

With hull length of 130' 4" she developed above 40 knots operating at $Fr_L \approx 1-1.1$,propelled by two 4000hp steam engines. Detailed description of propulsion plant, hull structure and topside arrangement was published in *Scientific American* v.50 1900. The data is available in the public domain, digitized by Google Inc. Although application of advanced technology broke the barrier of hull speed, it still remains a limit for economical transportation [5].

After breaking the hull speed barrier with steam engines and light aluminum hulls new challenges arose at the beginning of 19th century. The fast destroyer HMS Daring built in 1893 by Thornycroft & Co. was operating at $Fr_L \approx 0.6-0.7$ and developed severe cavitation problem discussed in detail in [6]. One way of reducing the cavitation phenomena on propeller blades is to reduce hull resistance at given speed. This can be done mainly, by achieving smaller stern wave, introducing appendages that provide hydrodynamic support, proper coating and reducing structural weight. Reduced hull resistance lowers the pressure drop on the propeller disk required to propel the vessel, thereby reducing the cavitation. Modifying the shape of the planing area to maximize lift and reduce drag is a core of the current work.

Exploiting the fact that flat plate skimming on free surface provides high hydrodynamic lift, flat bottomed fast vessels emerged during 1900-1915. The Royal Navy made acquisition of 25-foot and 40-foot Coastal Motor Boats manufactured by Thornycroft & Co. The boats were successfully deployed and participated in WWI as torpedo carriers, insertion craft for special missions. In 1919 the boats participated in attack on the Soviet Baltic fleet, sinking cruiser 'Oleg' and damaging several other battleships, according to Imperial War Museum at Duxford's website. 40-foot CMB hull is presented in Figure 3, reused with permission under non-commercial license, © IWM (MAR 563).

Figure 3. 40 ft CMB Hull in Imperial War Museum.

Planing surface efficiency, and efficiency of aircraft wings or a hydrofoils depends on aspect ratio defined as beam over length of the surface. A high aspect ratio lifting surface provides higher lift than a lower aspect ratio surface. The penalty for the high lift is a lower stall angles for high aspect ratio surfaces. Typical trim angle attained by vessels while planing is usually less than $10°$; therefore the stall angle is out of design consideration. In order to create high aspect ratio surfaces the designer often introduces steps in longitudinal or transversal directions. The first stepped motorboats appeared in France by 1905 and are shown in Figure 4, as published by 1909 magazine *La Nature Revue des Sciences* v.37 and digitized by *Le Conservatoire numérique des Arts & Métiers*, (Conservatoire numérique http://cnum.cnam.fr).

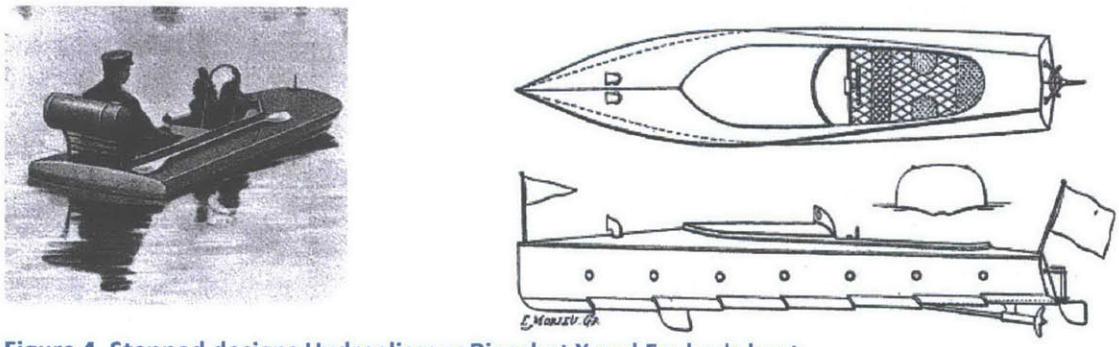

Figure 4. Stepped designs Hydroglisseur Ricochet X and Fauber's boat.

The longitudinal steps improve pitch motion while the transversal steps are used to increase roll stability, which is very important for sea going planing vessels. [7]. For example, transversal steps became an integral part in design of coast guard response boats and navy RIB's (Rigid Inflatable Boat).

During transition to planing regime, the initial wetted area of the vessel decreases as the boat is lifted by hydrodynamic forces. At high speed planing ($Fr_\nabla \approx 6$) about 85% of initially wetted surface rises out the water [1]. As a result, successful design ensures that the flow is separated from the hull in a reliable manner at locations prescribed by the designer. This approach is in contrast to the displacement hull design when the flow separation is undesirable as it introduces additional drag. Additional decrease of drag may be achieved by installing additional lifting surfaces on the hull.

Cornell University newspaper *Daily Sun*, reported on May 12, 1927 that 'Fantail' planing boat designed by Danish inventor Johannes Plum reached 55 knots with a payload of 1.8 metric tons. The boat was equipped with internal combustion engine of high power/weight ratio and adjustable stern stabilizer. It is evident that in order to compare different designs, the efficiency coefficient must be introduced. Transport Efficiency E_T is defined as the ratio between total propulsive efficiency η and resistance to weight ratio of a bare hull. E_T is given by equation (1.6). W is the weight of the vessel, R is a bare hull resistance and $P_{Delivered}$ is a power delivered to the propulsor.

$$E_T = \frac{W[N]\,U[m/s]}{P_{Delivered}[kW]} = \frac{\eta}{(R/W)_{Bare-hull}} \tag{1.6}$$

Plotting E_T vs. Fr_∇ different designs can be compared. Such comparison charts are presented in references [1], [7], [8]. The current work will focus on reduction of $(R/W)_{Bare-hull}$ ratio for a given hull.

For planing vessels it is common to express the displacement W in non-dimensional form, normalizing planing area A_p by displaced volume $\nabla = W/\rho$, expression (1.7). Heavy planing boats have non-dimensional displacement of 5-5.5, normally loaded 7, and light weight racing vessels above 8.5.

$$A_P/\sqrt[3]{\nabla^2} \tag{1.7}$$

As the boat becomes heavier more trim is required to achieve equilibrium in a planing regime. Plum's stabilizer was a complicated mechanical device that allowed to control the trim of 'Fantail'. This precise control maximized the advantage of high aspect ratio planing surface located in the forward part of the vessel. Plum evolved his stabilizer for several decades; first patented in 1927 the last version of the stabilizer was patented in 1965 [9]. The stabilizer can be adjusted to different values of W. Due to its mechanical complexity and applicability to relatively small boats, Plum's stabilizer was not widely implemented on planing craft.

Following the British success of WWI Thornycroft MTB design, the US Navy ordered a large number of patrol planing boats (PT-class) from Elco (350), Higgins (199) and Huckins (18) companies during 1940s. The boats were about 80 foot long wooden hull with 3 Packard 1200hp engines developed speed of 41 knots [7]. The boats served as a torpedo carriers, gunboats in WWII and afterwards. This fleet evolved into (PCF-class) aluminum 50 foot boats constructed by Swift Ships Co. Swift Boats operated in Vietnam War on Vietnamese coastal area and rivers. The boats had single hard chine, deep-V configuration with constant deadrise. Lack of any moving appendages, trim tabs, and roll stabilizers made the craft incredibly reliable. The last Swift Ship (PCF-class) boat retired in 2011 from the Maltese Navy according

to *Times of Malta* newspaper, online edition January 10, 2012. At the same period the Soviet Navy acquired more than 100 (Komar-class) planing vessels equipped with anti-ship guided missiles.

During the 1970s and 1980s much emphasis in planing craft was placed on improving habitability and seaworthiness. Warped hulls were introduced to achieve higher lift to drag ratio and reduced vertical acceleration impacts. The novice designs included two chines for slamming mitigation [10], [11]. The development of planing craft proceeded in Norway (Nasty-class) by Boat Services Ltd, Germany (Jaguar-class) by Lürssen Shipbuilding, and USSR (Osa-class) by R&D Almaz-Antey Group. In low draft planing vessels, the cavitation problems were reduced by surface piercing propellers [12], these propellers exhibit high efficiency in rough water, in bigger vessels water jet propulsors became common [13]. Savitsky and Gore [14] in their work present a genealogical tree for fast/planing hull evolution. The tree is superimposed on a 2D grid. The X axis indicates the country of development and the Y axis the year of launch. It spans a period from Parsons' experimental vessel Turbinia (1894) to U.S. Navy CPIC-X boat (1974), the prototype of modern Cyclone-class coastal patrol craft. More extensive information on historical planing craft appears in [15], a list of currently existing planing vessels and programs can be found in [16].

In light of this historical review, future trends in planing craft development may be highlighted. Out of 195 existing sovereign countries about 160 became independent during past century, while most of them have access to sea or long river lines. According to UN Convention on the Law of the Sea from December 10, 1982 extent of the territorial water is 12 nautical miles. This range is ideal for fast patrol boats operating in planing regime or on hydrofoils. The economical water extent up to 200 nautical miles, with increasing demand for offshore energy, became populated with offshore platforms. This development increased demand for fast reliable and seaworthy offshore supply vessels.

In an economy driven world when major destroyer programs are terminated (DDG-1000), low cost planing vessels remains economically attractive. Modern computer tools such as used in the current work drive down the development cost of modern planing hulls. Overall drag reduction achieved by current design allows reducing fuel consumption and therefore environmental impact. Lighter loads on the propulsive train will reduce wearing of the equipment and maintenance costs.

Chapter 2 will describe the validation of RANSE setup for evaluation of Dynaplane resistance. Major parameters such as the resistance, CG rise, trim angle will be compared.

Chapter 3 will briefly introduce the Clement's method and its application on Model 188 Gerritsma's hull.

Chapter 4 will discuss the improvements to Clement's method based on RANSE simulations and application of aircraft theory for wing/tail stability.

Concluding remarks and future work will be presented in chapter 5.

Chapter 2 - Validation of RANSE setup for evaluation of Dynaplane resistance.

Experimental investigations on the hydrodynamic characteristics of hard chine planing hulls have been conducted extensively by different Model Basin facilities. The studies of planing hulls conducted at DTMB in US, after the early studies at NACA and Davidson Lab, [17], [18] , [19], [20], KTH in Sweden [21], Delft Univ. and MARIN basin in Netherlands [22], [23], DST Duisburg and HSVA in Germany [24], TsAGI in Russia [25]. Although the results of experimental studies strongly depend on equipment calibration, measurement techniques and model precision, they are always physical. Many assumptions must be made in order to describe numerically the physical environment during CFD case setup; so one may easily produce unrealistic non-physical results. The main decision parameters in CFD case setup are: size of computational domain, boundary conditions, space and time discretization models, computational grid structure and density, initial conditions, convergence criteria, turbulence models and etc. In the current chapter experimental results for two different cases are used in order to validate the RANSE setup.

The first case is based on experimental results of Model 188 [22] with velocity range of $0.5 < Fr_{\nabla} < 3$, deep-V hull with 25° deadrise angle. After getting considerable agreement between the computational results and CFD runs, the computational runs extended to higher Froude numbers in range of $3 < Fr_{\nabla} < 6$. The second validation case includes calculation of resistance and trim angle for classical Dynaplane design of E. Clement as described in [26], hull model number 5115 with stern Plum stabilizer [9]. This hull has much lower deadrise angle of 12.5° and possesses a swept back cambered wing designed by Clement's method. The validation was performed for wider velocity range of $0.5 < Fr_{\nabla} < 6$ as more experimental results were available. It is important to notice that the hulls for both validation cases were based on existing hull series Model 188 of Gerritsma 25° series and model 4667-1 from Clement's & Blount series [20] respectively. Both models have the same length to beam coefficient of 4.09.

Resistance and trim angle of Model 188 – Validation Case I

In order to validate the results for hull 188 the Rhino 3D model of the hull was constructed at model scale. The main characteristics of the hull and comparison between CAD and physical model are shown in Table 1. All lengths are given in decimeters, areas in decimeters square. Coordinate system assigned: X-axis positive forward along ship length, Y-axis positive to port side, and Z-axis positive up, origin at intersection between the keel and aft perpendicular. The definition of comparison parameters as follows:

A_P – Projected planing bottom area, projected on X-Y plane as defined in Figure 6.

L_P – Length between perpendiculars in static condition.

B_{PA} – Mean breadth over chines.

B_{PX} – Maximum breadth over chines.

B_{PT} – Transom breadth over chines.

C_{AP} – Centroid of planing area, given as a fraction of length between perpendiculars, measured from the aft perpendicular.

The size and shape of the planing area is most important for hydrodynamics analysis, therefore all of the parameters above and their ratios deals with planing area configuration.

	Model 188	Rhino	Error [%]
A_P	45	44.835	0.4
L_P	15	15	0.0
B_{PA}	3	2.989	1.1
B_{PX}	3.67	3.63	4.0
B_{PT}	2.35	2.44	-3.8
L_P/B_{PA}	5	5.02	-0.4
L_P/B_{PX}	4.087	4.132	-1.1
B_{PX}/B_{PA}	1.22	1.21	0.7
B_{PT}/B_{PX}	0.64	0.67	-5.0
C_{AP}	48.8	48.01	1.6

Table 1. Comparison between physical hull model and Rhino 3D model.

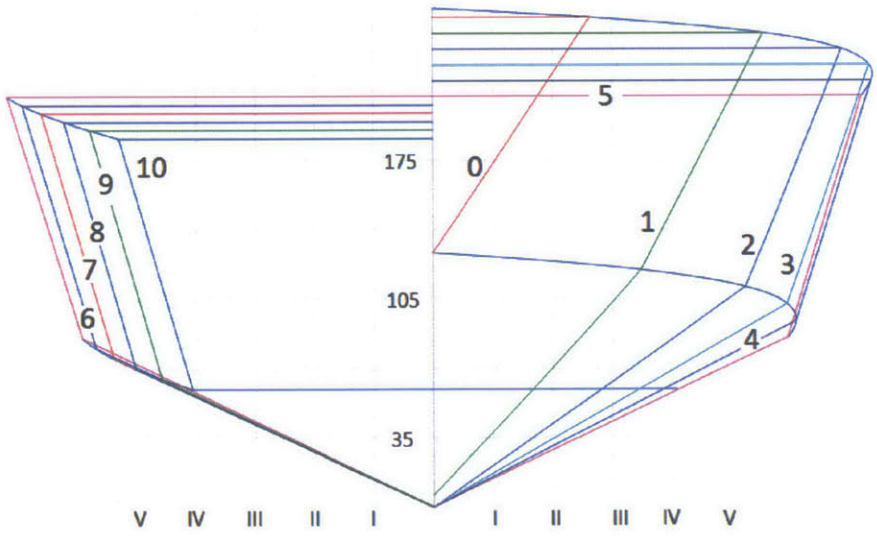

Figure 5. Gerritsma's Model 188 plan view (Y-Z plane) .

Figure 5 shows the plan view of the model, the model characteristics are high deadrise angle of 25° and hard chine configuration. The distance between longitudinal stations is 1 decimeter, the distance between buttocks lines 0.5 decimeters, denoted with roman notation. Buttocks and waterline views are presented in Figure 6.

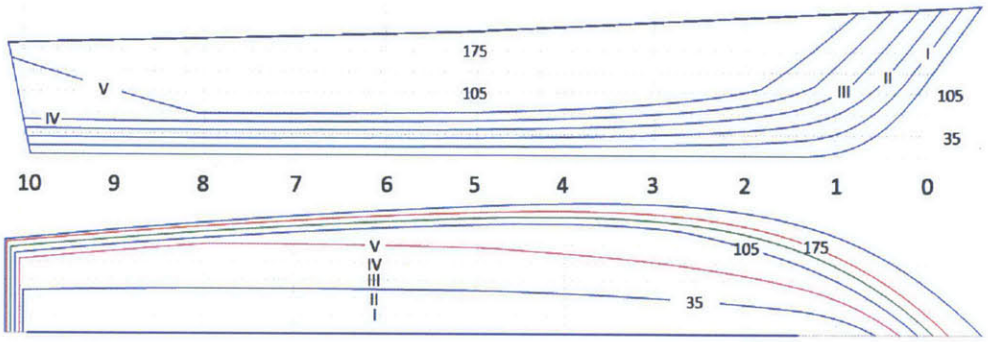

Figure 6. Buttocks (X-Z) and Waterplane (X-Y) lines.

The planing surface is bounded by a hard chine line, the projection of chine contour on X-Y and X-Z planes presented in Figure 7.

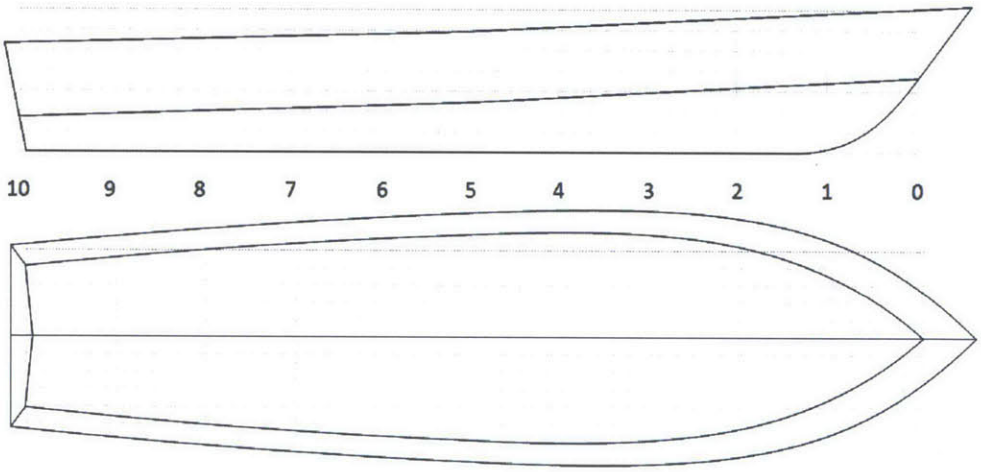

Figure 7. Side and bottom view model 188.

Additional parameters of the model:

∇ – Displaced volume in cubic meters.

AP – Aft perpendicular located at station 10.

FP – Forward perpendicular located at station 0.

During the experiment it was assumed that the shaft line passes through the station 10, 34[mm] below the keel. The inclination of the shaft line is 10° positive toward the bow. As the model during the test did not have self-propulsion this line indicates the towing line. In the numerical model it was assumed that the vertical center of gravity (VCG) of the vessel is located on the intersection of shaft line and the LCG. For the current validation case LCG of 672[mm] from AP was chosen. The displacement of the vessel during the experiment was 23.4[kg]. After geometrical model is defined, it is essential to evaluate the initial conditions of the planing hull for CFD simulation. One choice could be static equilibrium position, but as the model undergoes substantial sinkage and trim, it may apply large mesh deformations. A much better choice would be a position of equilibrium obtained by the Savitsky method for each speed. However, as the experimental results compare the trim and sinkage to static equilibrium position of the vessel, the static trim and sinkage was obtained using Hydromax software. Table 1 summarizes the major hydrostatic data for model 188.

	Hydrostatic Property	Value
1.	Draft Amidships [m]	0.095
2.	Displacement [kg]	23.4
3.	Draft at FP [m]	0.101
4.	Draft at AP [m]	0.089
5.	Draft at LCF [m]	0.095
6.	Trim by bow [m]	0.012
7.	Trim by bow [deg]	0.5
8.	Prismatic Coeff.	0.821
9.	Block Coeff.	0.424
10.	LCB from st10 [m]	0.672
11.	LCF from st10 [m]	0.692
12.	KB [m]	0.063
13.	KG [m]	0.083
14.	BM_t [m]	0.168
15.	BM_L [m]	2.838
16.	GM_t [m]	0.148
17.	GM_L [m]	2.817
18.	KM_t [m]	0.231
19.	KM_L [m]	2.9

Table 2. Model 188 Hydrostatic data.

Resistance prediction of Model 188 using theoretical method.

During the experiment of Model 188 both the displacement values and LCG location varied in order to evaluate the trends of hull planing behavior. Four displacements with four LCG locations calculated at 11 different speeds provide 176 runs. CFD simulation of the complete case requires months of computation time even on HPC cluster. On the other hand the semi-empirical method developed by Savitsky & Hadler [17], [18] may be used to estimate the hydrodynamic characteristics in a few seconds. Calibrating the method with experimental results will give us an important tool for calculation of resistance to displacement ratio and trim angle of a given planing hull with varying LCG, displacement and deadrise angle. The calibrated tool will be used to estimate the trim angle and resistance in higher Froude numbers, and will be used as a sanity check for the results obtained with CFD during different stages of validation, also at higher speed. The method is applicable in planing regime $Fr_L \geq 0.6, Fr_\nabla \geq 1.4$. The theoretical method was implemented using a Mathcad spreadsheet. Main parameters are summarized in Table 3 and graphically presented in Figure 8.

Parameter	Value	Description
LCG[mm]	735, 672, 612, 552	from AP, 0,4,8,12% aft of C_{AP}
Δ[kg]	37.7, 23.4, 16.3, 12.2	$\frac{A_P}{\sqrt[3]{\nabla^2}}$= 4,5.5,7,8.5
β[°]	25	Deadrise angle
ε[°]	10	Shaft inclination relative to keel
V_s [m/s]	1,1.44..8.8	20 equally spaced points in range of Fr_∇= 0.6-6
f	0	Shaft/tow line lever arm to CG
f_e [mm]	multiple, depends on V_s	Hydrodynamic force lever arm
f_f [mm]	85	Bottom friction lever arm to CG
f_a [mm]	no appendages	Appendages lever arm to CG
Fr_L	1.4-13.7	$V_s/\sqrt{gL_P}$
Fr_∇	0.6-6	$V_s/\sqrt{g\sqrt[3]{\nabla}}$

Table 3. Main parameters in Savitsky method.

Introducing the planing coefficients, speed coefficient C_v and prismatic surface lift coefficient $C_{L\beta}$:

$$C_v = \frac{V_s}{\sqrt{gB_{PA}}} \quad C_{L\beta} = \frac{\Delta g}{0.5\rho V_s^{\,2} B_{PA}^{\,2}} \tag{2.1}$$

Solving nonlinear equation to find lift coefficient for the flat plate C_{L0}:

$$C_{L\beta} = C_{L0} - 0.0065\beta C_{L0}{}^{0.6} \tag{2.2}$$

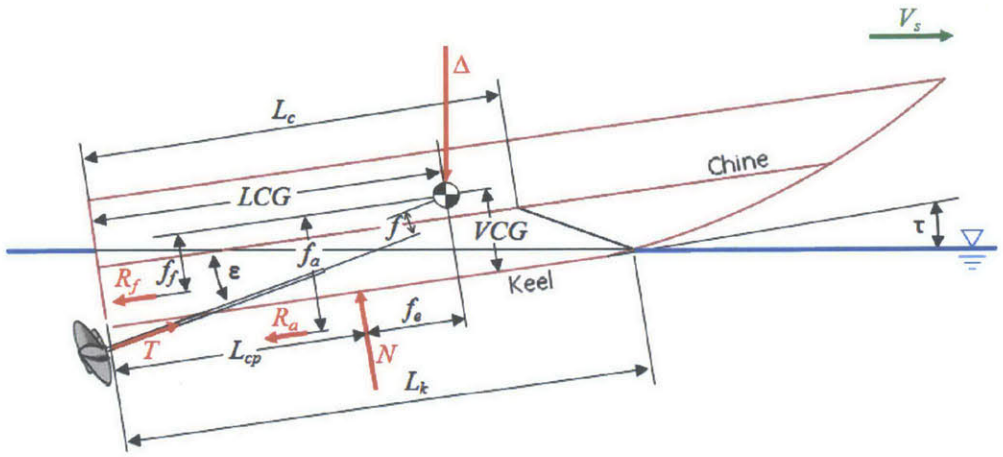

Figure 8. Schematic representation of forces acting on planing hull.

For solution of this non-linear equation, Mathcad's "Solve Block" was used with "Find" evaluation function, using V_s as a parameter. It is important to notice that in (2.2) and (2.3) deadrise angle β and trim angle τ are expressed in degrees. Next the mean wetted length beam ratio λ is evaluated:

$$C_{L0} = \tau^{1.1}\left(0.012\lambda^{0.5} + 0.0055\frac{\lambda^{2.5}}{C_v}\right) \tag{2.3}$$

Equation (2.3) was solved for λ using another "Solve Block" with τ and V_s as parameters. Mean wetted length L_m now can be evaluated using equation (2.4)

$$L_m = B_{PA}\lambda \tag{2.4}$$

As shown in (2.5) the mean wetted length L_m is an average between keel wetted length and chine wetted length. Both of these quantities are illustrated in Figure 8. The mean wetted length is essential for calculation of Reynolds number *Re* and estimation of friction forces.

$$L_m = \frac{L_c + L_k}{2} \tag{2.5}$$

Friction Forces

Experimentally it was shown [18] that the mean wetted length for prismatic hulls is influenced by spray generation, therefore some addition to λ is required. This addition is presented in Figure 9. In current study of Model 188 the deadrise angle is constant $25°$ along the hull length, and the graph can be reduced to a 2D plot, as shown in Figure 10.

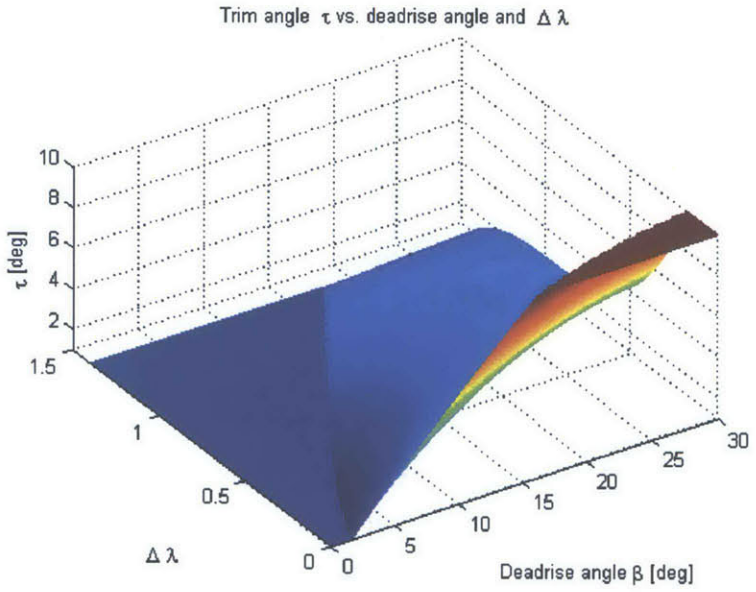

Figure 9. Influence of the deadrise and increase in mean wetted length to beam ratio due to spray, on the running trim angle.

Friction coefficient C_f was calculated using ITTC formula as follows:

$$C_f = \frac{0.075}{(\log(\mathrm{Re}) - 2)^2} \tag{2.6}$$

The Reynolds number is relative to the mean wetted length L_m as described in equation (2.7):

$$\mathrm{Re} = \frac{V_s L_m}{\nu_{fw}} \tag{2.7}$$

The kinematic viscosity for the calculation was obtained from ITTC 7.5-02-01-03 procedure at experiment conditions $\nu_{fw} = 0.9574 \cdot 10^{-6} \left[m^2/s \right]$.

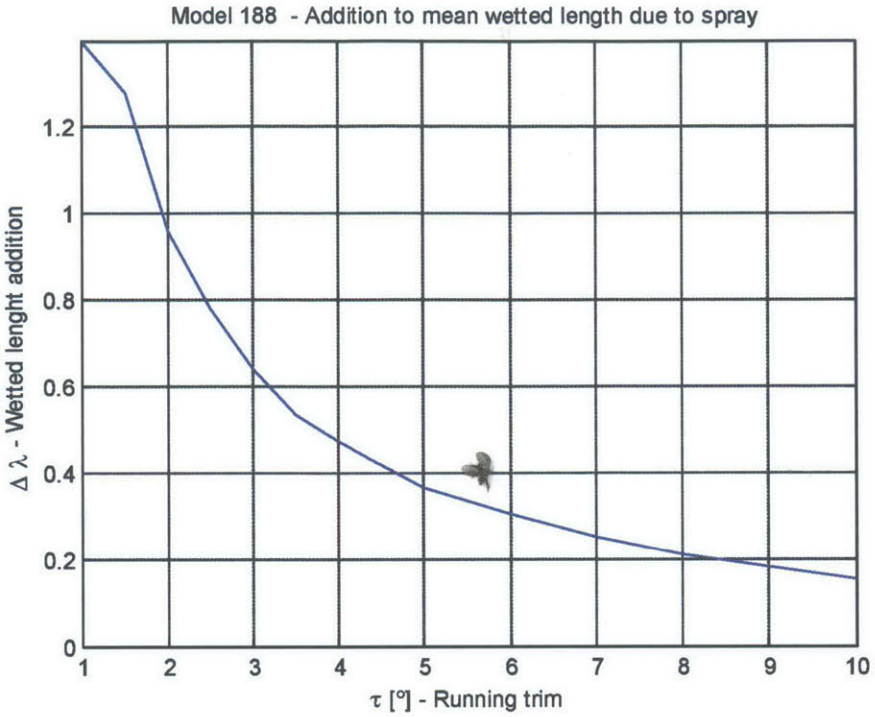

Figure 10. Mean wetted length addition vs. trim.

The roughness allowance was neglected in the validation case, as we assumed that the surface is hydraulically smooth as defined in [27], since the size of the model is relatively small. Using C_f with corrected wetted area, the friction force R_f and its lever arm around the center of gravity (CG) can be calculated using equations (2.8) and (2.9)

$$R_f = C_f \frac{1}{2} \rho V_s^2 (\lambda + \Delta\lambda) \frac{B_{PA}^2}{\cos(\beta)} \tag{2.8}$$

$$f_f = VCG - \frac{B_{PA}}{4} \tan(\beta) = 4.8[cm] \tag{2.9}$$

The vertical distance between keel and chine is $\frac{B_{PA}}{2}\tan(\beta)$ and the method assumes that friction force is acting at half of that distance from the keel.

In a similar way force due to foils/rudder can be estimated with $C_{frudder}$ calculated with ITTC equation (2.6) using associated foil/rudder length and corrected local speed. Equation (2.10) estimates the forces due to foils/rudder.

$$R_{rudder} = C_{frudder} \frac{1}{2} \rho V_s^2 S_r \left(1 + 2\left(t/c\right) + 60\left(t/c\right)^4\right) \tag{2.10}$$

In equation (2.10) S_r denotes wetted rudder area and $\left(t/c\right)$ the thickness to cord ratio. Exposed shafts introduce additional resistance R_{shaft} . This resistance can be evaluated using equation (2.11):

$$R_{shaft} = \frac{1}{2} \rho V_s^2 L_{shaft} D_{shaft} \left(1.1 \sin^3(\varepsilon) + \pi C_{fshaft}\right) \tag{2.11}$$

Friction coefficient C_{fshaft} is evaluated using (2.6) with Re based on exposed shaft length L_{shaft}. Diameter of the inclined shaft is D_{shaft} and inclination angle ε[deg]. The appendages create total resistance $R_a = R_{shaft} + R_{rudder}$ acting at a distance f_a from the VCG as shown in Figure 8.

In the current validation study no appendages were installed, but the stabilizing hydrofoils will be added in a later stage of the design.

Hydrodynamic Forces

The center of pressure location (LCP) is defined by equation (2.12). In this empirical relation the first term in the parentheses denotes the influence of hydrodynamic forces and the second term the influence of the buoyancy forces.

$$LCP = L_m \left(0.75 - \frac{1}{5.21 C_v^2 / \lambda^2 + 2.39}\right) \tag{2.12}$$

The hydrodynamic force N acts at LCP and, by definition, creates positive moment about CG, when the hull tends to turn bow down. The lever arm for this moment f_e is defined in equation (2.13):

$$f_e = LCG - LCP \tag{2.13}$$

Bow down moment consists of moments due to hydrodynamic forces on the hull, frictional viscous forces on the hull, presence of the appendages (struts, rudders and hydrofoils). All the forces in the validation case create a bow down moment about CG, as the towing line passes through the VCG. At given carriage speed the location of LCP and trim angle changes until the equilibrium is achieved.

$$M_{hyd} = g\Delta \left(\frac{f_e \cos(\tau + \varepsilon)}{\cos(\varepsilon)} - \frac{f \sin(\tau)}{\cos(\varepsilon)}\right) \tag{2.14}$$

$$M_{fric} = R_f\left(f_f - f_e\tan(\varepsilon) - \frac{f}{\cos(\varepsilon)}\right) \tag{2.15}$$

$$M_{append} = R_a\left(f_a - f_e\tan(\varepsilon) - \frac{f}{\cos(\varepsilon)}\right) \tag{2.16}$$

The equilibrium is achieved when the total moment is zero:

$$M_{tot}(\tau, \mathrm{V}_s, \mathrm{LCG}, \Delta) = M_{hyd} + M_{fric} + M_{append} = 0 \tag{2.17}$$

Equation (2.17) is solved for running trim angle τ_0 using Mathcad "solve block" with displacement, LCG and speed as parameters. The syntax of the MathCad command is presented in equation (2.18). This solve block triggers all other solve blocks defined earlier in order to assemble and evaluate all unknown coefficients.

$$\tau_0(V_s, LCG, \Delta) := Find(\tau) \tag{2.18}$$

This approach automates the iterative procedure of Hadler, as described in [28].When τ_0 is known, the total resistance and power can be evaluated using equation (2.19), the sinkage of the transom defined by equation (2.20):

$$R_t = g\Delta\sin(\tau_0) + \mathrm{R}_f\frac{\cos(\tau_0 + \varepsilon)}{\cos(\varepsilon)} \tag{2.19}$$

$$L_k = \lambda B_{PA} + \frac{B_{PA}\tan(\beta)}{2\pi\tan(\tau_0)},\ Draft = L_k\sin(\tau_0) \tag{2.20}$$

The planing efficiency may be defined as normalized resistance $R_t/g\Delta$. The effective towing power is defined in equation (2.21):

$$P_E = V_s R_t \tag{2.21}$$

This theoretical model works well in prediction of resistance and running trim angle for self-propulsive vessel. Usually, and specifically in our case, the model is towed by carriage along the tank, slightly simplifying the forces acting on the vessel as shown in Figure 11. The thrust force T, acting along shaft line corresponds to the carriage force T_c.

In the general case, the towing force T_c acts at distance f_c from VCG. In our case this force acts at the intersection of LCG and shaft line, 8.3[cm] above the keel.

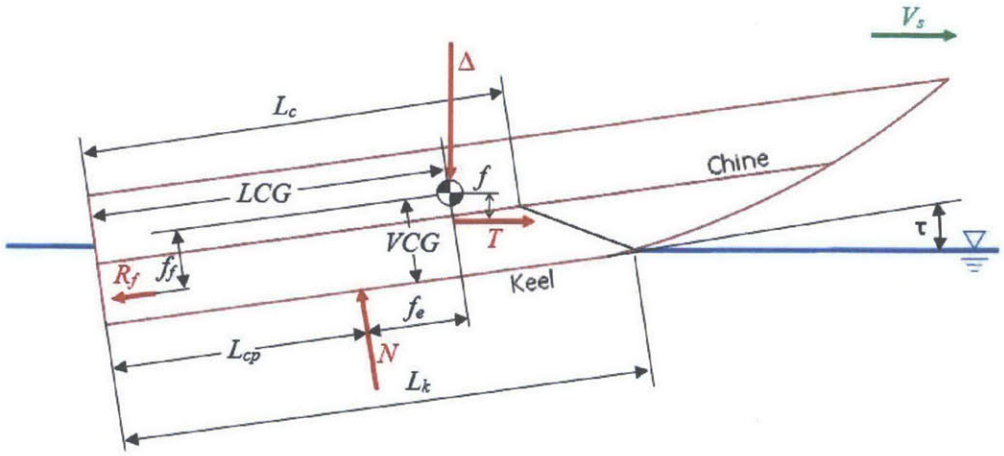

Figure 11. Free Body Diagram of towed body.

Since the equations of equilibrium can be rewritten as follows:

Vertical equilibrium:
$$\Delta = N\cos(\tau) - R_f \sin(\tau) \tag{2.22}$$

Horizontal equilibrium:
$$T_c = R_f \cos(\tau) + N\sin(\tau) \tag{2.23}$$

$$f_c = (VCG - 0.083)\cos(\tau) \tag{2.24}$$

Moment:
$$M_{tot}(\tau, V_s, \mathrm{VCG}, \mathrm{LCG}, \Delta) = Nf_e + R_f f_f - T_c f_c = 0 \tag{2.25}$$

Substituting equations (2.22),(2.23),(2.24) into (2.25) and evaluating for T_c:

$$\left(\frac{\Delta + R_f \sin(\tau)}{\cos(\tau)}\right) f_e + R_f f_f - \left(R_f \cos(\tau) + (\Delta + R_f \sin(\tau)\tan(\tau))\right) f_c = 0$$

$$\left(\frac{\Delta + R_f \sin(\tau)}{\cos(\tau)}\right) f_e + R_f f_f - (VCG - 0.083)\left(R_f + \Delta\sin(\tau)\right) = 0 \tag{2.26}$$

$$R_t = T_c = R_f\left(\cos(\tau_0) + \sin(\tau_0)\tan(\tau_0)\right) + \Delta\tan(\tau_0)$$

As can be seen from equation (2.26) the total resistance depends mostly on hull friction R_f, initial displacement and equilibrium trim angle τ_0. The sinkage and effective towing power in both cases are defined by equations (2.20) and (2.21) respectively.

The non-linear system of equations (2.25) is solved iteratively in MathCad instead of system (2.17).

Numerical Model

The numerical simulation was performed using CD-Adapco RANS solver, Star-CCM+, as implicit unsteady case with use of Dynamic Fluid Body Interaction module, VOF (Volume of fluid) scheme and segregated flow. The solver was chosen because of its ability to implement High Resolution Interface Capturing scheme (HRIC) for a free surface, it has predefined field functions for marine applications which reduce the possibility of error in user inputs. Moreover, difficult topology may be resolved by using overset meshes (Chimera grids). Customizable Application Programming Interface (API) exists for automating preprocessing and post processing stages of the design based on Java programming language. The current section discusses the numerical setup and explains the considerations behind the choices that were made to prepare the simulation model.

Geometry of computational domain

The size of computational domain was chosen to incorporate the dynamic phenomena and minimize effects of boundary reflections, yet not to exceed available computational resources. The numerical model exploits the symmetry of the flow and motions. The symmetry plane passes throw centerline plane; allowed motions are pitch and heave only.

The triangulated CAD model exported from Rhino was subtracted from a rectangular block, creating new boundaries (hull) at intersection of these two parts. The new boundaries were linked together into a rigid body and the moving boundary conditions were assigned. The morphing module was activated to allow mesh deformation around the hull.

The maximum speed of the vessel during the validation study is $U = 5.025[m/s]$. The phase speed of generated wave is equal to vessel speed, therefore the length of generated wave λ (assuming deep water, i.e. no influence from the bottom) is defined by the dispersion relation equation(2.27):

$$\lambda \approx 2\pi \frac{U^2}{g} = 16.2[m] \qquad (2.27)$$

The computational domain has rectangular shape as shown in Figure 12, with extend of $1.5\lambda = 24.3[m]$ behind the hull. The origin is located at intersection of AP and the keel.

The transverse extend of the domain is $1.5\lambda \tan(19°28') \approx 8.6[m]$, in order to keep the Kelvin's wake inside the computational domain. The hull was initially rotated to running trim angle τ. Starting from the already inclined hull reduces the dynamic trim motion and consequently reduces the mesh deformations required for achieving the equilibrium and shortens the computational time.

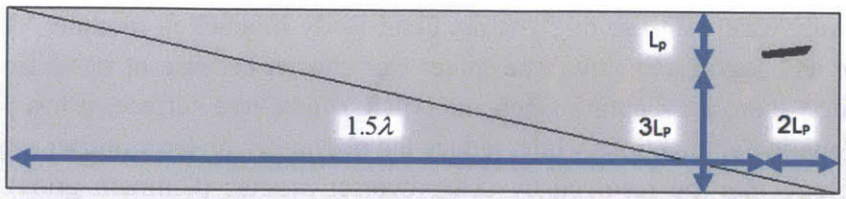

Figure 12. Computation domain.

The running trim angle was calculated using the Savitsky-Hadler method as described in previous section by equations (2.17), (2.18). The sinkage at transom was calculated using (2.20). The distance between the free surface and the bottom is $3L_P$ in order to prevent shallow water effects.

Space discretization – Computational Mesh

Cartesian mesh was chosen to discretize the computational domain due to its ability of alignment to undisturbed free surface. If the mesh is not aligned with free surface, the volume fraction is interpolated within the cell smearing the sharp interface between fluid and air phase. This fact causes unrealistic partially wetted bottom of the vessel and substantial inaccuracy in friction drag prediction. A prism layer was used around the hull to capture the boundary layer. The size of the first cell was chosen to maintain y+ of 30, as defined by equation (2.28)

$$y^+ = \frac{u^* y}{\nu_{fw}} = 30 \text{ with } u^* = \sqrt{\frac{\tau_w}{\rho}} \tag{2.28}$$

Fresh water density represented by ρ, wall shear stress was estimated as $\tau_w = C_f \rho V_s^2 / 2$, with C_f evaluated by equation (2.6). For maximum speed achieved during the validation $V_s = 5.025[m/s]$, the thickness of the first layer was 0.142[mm]. Turbulence models influence the flow differently inside and outside the boundary layer. Star-CCM+ applies wall function to identify the boundary layer. If y+ is smaller than 1, it means that the mesh is fine enough to resolve the boundary layer and no wall function is applied. If y+ is larger than 50 the boundary layer is not captured accurately, the code cannot attenuate the turbulence inside the laminar flow inside the boundary layer. The distribution of wall y+ parameter for computational cells attached to hull is shown in Figure 13.

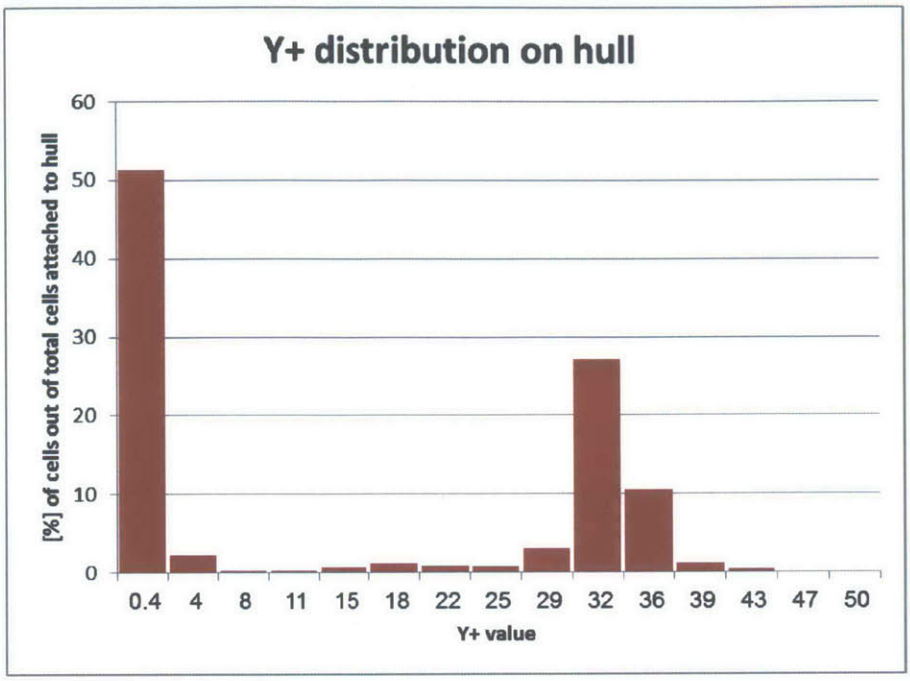

Figure 13. Distribution of y+ parameter on hull.

The results above were obtained after the computation converged. It is evident that approximation of the y+ with equation (2.28) provides fair results. The results apply to the entire hull including the air exposed structure, about 51% of all cells. The wall y+ for these cells is less than 5. Total number of cells attached to the hull was 32278. The entire domain spans a volume of $1420[m^3]$ water and air, discretizing it with 0.142[mm] side length cells requires $4956 \cdot 10^{11}$ cells. This number is beyond the available computational resources. The entire domain was discretized by 2.2M cells with local refinements near the free surface and the model's transom. Mesh density and its distribution subjected to sensitivity check. Computational runs were performed on coarse, medium and fine meshes with mesh size of 0.4M, 2.2M and 14M cells for $Fr_{\nabla} = 4$. Table 4 present the influence of mesh size on the resistance and trim angle. The 14M cells mesh was chosen as baseline for error estimation, as this mesh should provide most accurate results.

Million Cells	$R_t/g\Delta$	Error[%]	Trim[°]	Error[%]
0.4	0.212	5.9	4.8	1.4
2.2	0.204	2.0	4.9	0.4
14	0.200	-	4.9	-

Table 4. Mesh size sensitivity.

For all subsequent runs, mesh of 2.2M was selected for practical reasons bearing in mind the values of discretization errors, as presented above. The time step for validation case was chosen as $6 \cdot 10^{-4}[s]$. This choice was made to satisfy the CFL condition, as described in multiphase formulation section.

Temporal discretization – time step

The problem under investigation is transient with time varying boundary motions, however for each speed only the final state is important. For all runs implicit unsteady simulation was used with 1st order time discretization scheme and 3 inner iteration loops.

Solver algorithm

The Navier-Stokes equations (2.29) describe the flow phenomena under consideration. The first equation is the continuity equation for incompressible flow and the second represents the conservation of momentum. These equations are solved iteratively in each step of the computation. Due to incompressibility of the flow, there is no need to solve equation of state. The process is isothermal therefore the energy equation is not solved as well. Vector $u_i = [u, v, w]$ represents the components of fluid velocity, vector $x_i = [x_1, x_2, x_3]$ represents unit vectors in x,y,z direction respectively. Star-CCM+ utilize the Semi-Implicit Method for Pressure-Linked Equations developed by Patankar and Spalding (SIMPLE) to solve N-S equations [29]:

$$\begin{aligned} &\frac{\partial u_i}{\partial x_i} = 0 \\ &\frac{\partial u_i}{\partial t} + u_j \frac{\partial u_i}{\partial x_j} = \frac{1}{\rho}\frac{\partial p}{\partial x_j} - \frac{\mu}{\rho}\frac{\partial}{\partial x_j}\left(\frac{\partial u_i}{\partial x_j} + \frac{\partial u_j}{\partial x_i}\right) \end{aligned} \tag{2.29}$$

For uncompressible flow, velocity vector field u_i must be solved, the equations are coupled with values of unknown scalar pressure field p. The SIMPLE method decouples this dependence by guess and correction of the pressure field. As equation (2.29) deals only with gradients of pressure field p and the solution is performed on discrete grid points, some numerical complications arise. For example, the uniform pressure distribution and non-continues check board pressure distribution will influence the momentum equations in the same way. To overcome this numerical obstacle, a staggered grid is used in which the pressure field and velocity field are evaluated in different locations. The SIMPLE algorithm is well described in [30] and is summarized here. For complete understanding of the procedure reading of chapter 4,5,6 in [29] and 6,8 in [30] is recommended:

1. Guess scalar pressure field p^*. (The real field $p=p^*+p'$, p' is pressure correction).
2. Solve momentum equations to obtain u^*. ($u=u^*+u'$, u' is velocity correction term).

3. Through momentum equations p' can be related to u'. Substituting $u'=u-u^*$ into momentum equation relates u to p', creating velocity correction equation. In this step the discretized momentum equation is being simplified by omitting the term that denotes momentum change due to velocity change in neighboring cells. This manipulation simplifies the solution of p' and it does not impact the final result, as at convergence $p'=0$ and $p=p^*$. Due to this simplification, the algorithm named "Semi-Implicit".
4. Substitute the velocity correction equation into the integral form of discretized continuity equation. All the velocities are expressed in p'. Solve for p'.
5. Using p' as input in momentum discretized equations and solve for u'.
6. Evaluate u by adding u' to u^*.
7. Solve discretized equations for other transport parameters that affect velocity field such as turbulence energy and dissipation, volume fraction, temperature.
8. The corrected pressure $p=p^*+p'$ becomes new p^*, repeat the algorithm from 2nd step until convergence. It is useful to correct the p^* by a portion of p' at each step to avoid explosion of the solution. $p = p^* + \alpha p'$. In current work the under-relaxation factor $\alpha = 0.8$ was used.

Turbulence model

The flow regime around the model is turbulent with $\mathrm{Re} = (6-7)\cdot 10^6$. The turbulence introduces generation of random eddies with fluctuating flow properties outside the boundary layer. The eddies in turbulent flow have different velocities and characteristic lengths, the energy needed for fluctuation and eddies creation gained from the mean flow and passes between eddies of different length scales [31]. Resolving the eddies with direct numeric simulation is computationally expensive, therefore Reynolds Averaged Navier-Stokes equations are introduced. Assuming the flow is stationary over time, and uniform on average in all directions [32], the time scale $\tau \ll T$.

$$u_i = \overline{u}_i + u_i'$$
$$\overline{u}_i = \frac{1}{\tau}\int_0^{\tau} u_i dt \tag{2.30}$$

The key concept in the RANS method is to separate the velocity unknowns into constant or slowly varying part $\overline{u}_i$ and fluctuating part u_i'. The fluctuating part has zero time average, therefore the solution of small eddies is omitted. The continuity and momentum conservation equations (2.29) can be rewritten as follows:

$$\frac{\partial \overline{u_i}}{\partial x_i} = 0$$
$$\frac{\partial \overline{u_i}}{\partial t} + \overline{u}_j \frac{\partial \overline{u_i}}{\partial x_j} = \frac{1}{\rho}\frac{\partial p}{\partial x_j} - \frac{1}{\rho}\frac{\partial}{\partial x_j}\left(\overline{\tau_{ij}} - \rho\overline{u_i' u_j'}\right) \tag{2.31}$$

In equation (2.31) the term $\overline{\tau_{ij}} = \mu\left(\frac{\partial \overline{u_i}}{\partial x_j} + \frac{\partial \overline{u_j}}{\partial x_i}\right) = S_{ij}$ denotes the mean flow strain rate tensor with viscosity μ. Continuity, x,y,z momentum equations (2.31) can be solved with 4 unknowns (u,v,w,p) before introducing the Reynolds-stress tensor $-\rho\overline{u_i' u_j'}$. The additional term introduces 6 new unknowns, therefore empirical turbulence model is needed to close the problem and solve the flow.

The total energy of the flow per unit mass is defined as $E = \frac{1}{2}\left(u^2 + v^2 + w^2\right)$. The energy of fluctuating eddies in a similar way is $k = \frac{1}{2}\left(\overline{u'^2} + \overline{v'^2} + \overline{w'^2}\right)$, it is easy to see that turbulent kinetic energy is related to a trace of Reynolds stress tensor $\tau_{ii} = -\rho\overline{u_i' u_i'} = -2\rho k$. Boussinesq approximation relates the mean strain tensor to Reynolds stress tensor using eddy viscosity μ_T as defined in (2.32). Denote the trace correction term $-(2/3)\rho k\delta_{ij}$, as $S_{ii} = 0$ to satisfy the continuity equation (2.29) [32].

$$\tau_{ij} = -\rho\overline{u_i' u_j'} = 2\mu_T S_{ij} - \frac{2}{3}\rho k\delta_{ij} \tag{2.32}$$

From dimensional analysis turbulence kinetic energy k and turbulence dissipation rate ε can fully describe the behavior of turbulent flow [33]:

$$\text{Eddies time scale } \tau \propto k/\varepsilon$$
$$\text{Eddies length scale } l_e \propto k^{3/2}/\varepsilon \tag{2.33}$$
$$\text{Eddies kinematic viscosity } \nu_T = \mu_T/\rho \propto k^2/\varepsilon$$

Constructing and solving equations for k and ε allows to resolve turbulence effects without prior knowledge of the flow. The transport equation of total kinetic energy of the fluids is obtained using following steps: Multiplying each of momentum equations (2.29) by u,v,w, summing and averaging them in time. The transport equation of mean kinetic energy is obtained by multiplying each of momentum equations (2.31) by $\overline{u},\overline{v},\overline{w}$ and summing them. The

difference between these transport equations gives the transport equation of turbulence kinetic energy. This equation is presented here in differential notation:

$$\rho\frac{\partial k}{\partial t}+\rho\bar{u}_j\frac{\partial k}{\partial x_j}=\tau_{ij}\frac{\partial \bar{u}_i}{\partial x_j}-\rho\varepsilon+\frac{\partial}{\partial x_j}\left[\mu\frac{\partial k}{\partial x_j}-\frac{1}{2}\rho\overline{u_i'u_i'u_j'}-\overline{p'u_j'}\right]$$
$$\varepsilon=\frac{\mu}{\rho}\overline{\frac{\partial u_i'}{\partial x_k}\frac{\partial u_i'}{\partial x_k}} \tag{2.34}$$

The seven terms in (2.34) govern the behavior of turbulence energy and it distribution in the flow. The terms highlighted in red need to be defined empirically. The first two terms are material derivative of k following the particle. The third term is a production terms which controls the energy transfer to turbulence from the mean flow. The next term controls the energy dissipation, the rate at which the kinetic energy of the flow passes into internal energy of the fluid. Without supply of energy to the turbulence, the turbulence will rapidly decay due to dissipation. Gravity waves for example are not dissipative and therefore are not turbulent [31]. The last 3 terms represent a molecular diffusion and diffusion due to turbulence which denotes the rate of mixing of the molecules due to presence of eddies and a scalar pressure field. Assuming that all diffusion terms have similar behavior, the expression in parenthesis can be rewritten:

$$\left[\mu\frac{\partial k}{\partial x_j}-\frac{1}{2}\rho\overline{u_i'u_i'u_j'}-\overline{p'u_j'}\right]=\left(\mu+\frac{\mu_T}{\sigma_k}\right)\frac{\partial k}{\partial x_j} \tag{2.35}$$

The empirical constant σ_k is chosen to be 1, (2.34) becomes:

$$\rho\frac{\partial k}{\partial t}+\rho\bar{u}_j\frac{\partial k}{\partial x_j}=\tau_{ij}\frac{\partial \bar{u}_i}{\partial x_j}-\rho\varepsilon+\frac{\partial}{\partial x_j}\left[(\mu+\mu_T)\frac{\partial k}{\partial x_j}\right] \tag{2.36}$$

Star-CCM+ solves the turbulence equations in finite volume, therefore the integral notation of (2.36) is used. dV denotes integration over the cell, dA denotes flux over cells boundaries:

$$\rho\frac{\partial}{\partial t}\int_V kdV+\rho\int_A ku_i dA=\int_V \mathrm{G}_k\mathrm{dV}-\rho\int_V(\varepsilon-\varepsilon_0)dV+\int_A(\mu+\mu_T)\left(\frac{\partial k}{\partial x_j}\right)dA \tag{2.37}$$

ε_0 is ambient value that counteract dissipation decay. Experimentally found to be of order $10^{-4}U^3/\delta$ with U typical velocity at boundary layer edge and δ is the thickness of boundary layer [34]. The turbulent viscosity is computed as:

$$\mu_T = \rho C_\mu \frac{k^2}{\varepsilon}$$

$$C_\mu = \left(4 + \left[\sqrt{6} \cos\left(\frac{1}{3} a \cos\left(\frac{\sqrt{6} S_{ij} S_{jk} S_{ki}}{\left(S_{ij} S_{ij} \right)^{3/2}} \right) \right) \right] \left(\sqrt{S_{ij} S_{ji} - W_{ij} W_{ji}} \right) \frac{k}{\varepsilon} \right)^{-1} \tag{2.38}$$

In (2.38) vorticity tensor $W_{ij} = e_{ijk}\omega_k$ is formed by multiplying the Levi-Cevita symbol e_{ijk} with vorticity vector $\omega_k = \nabla \times u$. Reference [35] provides the development of (2.38) in detail.

The turbulence production term G_k is evaluated by substituting (2.32) into third term of (2.34):

$$G_k = 2\mu_T S_{ij} S_{ji} - \frac{2}{3}\rho k \frac{\partial u_i}{\partial x_i} - \frac{2}{3}\mu_T \left(\frac{\partial u_i}{\partial x_i} \right)^2 \tag{2.39}$$

Turbulent kinetic energy (2.37) is coupled with turbulence dissipation rate ε. The transport equation for dissipation rate must be obtained in order to proceed with the solution. Combining the dissipation term of (2.34) with (2.31) and taking time average, equation for ε is obtained. This expression is similar to (2.34) with ε instead of k. The four red highlighted terms in (2.34) are replaced with 11 new unknowns [32]. Estimating these terms one by one is practically impossible. Preserving the non-highlighted terms from (2.34), the dissipation equation can be rewritten:

$$\rho \frac{\partial \varepsilon}{\partial t} + \rho \overline{u}_j \frac{\partial \varepsilon}{\partial x_j} = C_{\varepsilon 1} \frac{\varepsilon}{k} \tau_{ij} \frac{\partial \overline{u}_i}{\partial x_j} - C_{\varepsilon 2} \rho \frac{\varepsilon^2}{k} + \frac{\partial}{\partial x_j} \left[\left(\mu + \frac{\mu_T}{\sigma_\varepsilon} \right) \frac{\partial \varepsilon}{\partial x_j} \right] \tag{2.40}$$

This equation has 3 closure coefficients $C_{\varepsilon 1}, C_{\varepsilon 2}, \sigma_\varepsilon$ that must be defined to close the problem. The third term in (2.40) is dissipation production term, or rate of dissipation "build up". The fourth term controls the destruction of dissipation. The turbulence would vanish without supply of new energy from mean flow and so do the dynamics of dissipation. One must consider both construction and destruction terms per unit time, therefore these terms are normalized by large eddy turn-over time k/ε [31]. Star-CCM+ implements the integral form of (2.40) with some modifications as follows:

$$\begin{aligned} &\rho \frac{\partial}{\partial t} \int_V \varepsilon dV + \rho \int_A \varepsilon u_i dA = \\ &= \int_V C_{\varepsilon 1} \sqrt{2 S_{ij} S_{ji}}\, \varepsilon \, \mathrm{dV} - \int_V C_{\varepsilon 2} \rho \frac{\varepsilon}{k + \sqrt{\nu \varepsilon}} (\varepsilon - \varepsilon_0) dV + \int_A \left(\mu + \frac{\mu_T}{\sigma_\varepsilon} \right) \left(\frac{\partial \varepsilon}{\partial x_j} \right) dA \end{aligned} \tag{2.41}$$

Closure coefficients are: $\sigma_\varepsilon = 1.2$, $C_{\varepsilon 2} = 1.9$, $C_{\varepsilon 1} = \max\left(0.43, \frac{k\sqrt{2S_{ij}S_{ji}}}{5\varepsilon + k\sqrt{2S_{ij}S_{ji}}}\right)$.

The development of equation (2.41) is provided in detail in [36] by NASA turbulence research center. It important to mention that the advantage of the model (2.41) over classical formulation (2.40) is that the model is well behaved at large strain rates $|S|\frac{k}{\varepsilon} = \sqrt{2S_{ij}S_{ji}}\frac{k}{\varepsilon} > 3.7$, while the classical model fails to do so. Moreover it does not over predict turbulence levels near stagnation points due to the presence of ambient source term ε_0.

The complex turbulence model presented above is combined with a simple, one equation algebraic model with single unknown k. The blend between the two models depends on the distance from the nearest wall. The algebraic model is defined by the following set of equations:

$$\mathrm{Re}_y = \frac{\sqrt{k}y}{\nu} \tag{2.42}$$

$$\mu_T = 0.23\mu\mathrm{Re}_y\left(1-\exp\left(-\frac{\mathrm{Re}_y}{70}\right)\right) \tag{2.43}$$

$$l_\varepsilon = 2.55y\left(1-\exp\left(-\frac{\mathrm{Re}_y}{5.11}\right)\right) \tag{2.44}$$

Re_y denotes turbulence Reynolds number, μ_T eddies viscosity and l_ε eddies mean length scale. At each point of calculation the distance y from the wall is known. Using (2.43), (2.44) and recalling the first part of (2.38) with constant $C_\mu = 0.09$ both dissipation rate ε and eddies mean scale l_ε can be expressed as a function of k only. Now equation (2.33) $l_\varepsilon = k^{3/2}/\varepsilon$ is solved to find k. This simple model is blended with the complex model using the following blend function:

$$\begin{aligned}\mu_T &= \lambda\mu_{T(\mathrm{k}-\varepsilon)} + (1-\lambda)\mu_{T(\mathrm{alg})}\\ \lambda &= \frac{1}{2}\left(1+\tanh\left(\frac{\mathrm{Re}_y - 60}{4.35}\right)\right)\end{aligned} \tag{2.45}$$

It is seen from (2.45) that for two layer formulation in Star-CCM+ below $\mathrm{Re}_y = 50$ simple algebraic model is used, above $\mathrm{Re}_y = 70$ full $k-\varepsilon$ model is used and between $\mathrm{Re}_y = 50-70$ a combination of the two models is implemented. The complete formulation of the turbulence model includes density and viscosity expansion for multiphase flow, relative velocity due to

moving grid, additional source terms. In order to convey the essential formulation of the turbulence model these additional parts were omitted from the current chapter.

Multiphase formulation

While solving Volume of Fluid (VOF) formulation Star-CCM+ assumes that both the liquid and solid phases shares the velocity and pressure fields. The interface between the phases is sharp and in the current study no phase changes are allowed. The air cannot dissolve in water and water cannot evaporate. By checking the Cavitation number at the end of each run, one must assure that the fluid pressure did not drop beyond the saturation limit. Although the study deals with high speed flow, the hull is partially ventilated and hydrofoils are surface piercing, therefore the cavitation is not expected. Volume fraction is represented by unknown $c_i = V_i/V$, for water and liquid phases $c_{air} + c_{water} = V_{air}/V + V_{water}/V = 1$ The density and viscosity can be expanded as follows:

$$\rho = \sum_i \rho_i c_i \ , \quad \mu = \sum_i \mu_i c_i \tag{2.46}$$

The convection equation for volume fraction is presented in (2.47). The physical meaning of (2.47) is that the change of fluid within the cell is equal to the sum of fluxes on the cell's boundaries.

$$\frac{\partial}{\partial t}\int_V c_i dV + \int_A c_i u_i \cdot n dA = 0 \tag{2.47}$$

The numerical solution for (2.47) can be obtained using different discretization schemes described in detail by [37]. Example of 1-D Upwind scheme for linear convection equation (2.47) is shown in (2.48). Property c is traveling at speed u in one direction, n indicates the iteration number or time step, j indicates the position on 1-D grid. Equation (2.48) is a 1st order Upwind scheme.

$$\frac{c_j^{n+1} - c_j^n}{\Delta t} + u\frac{c_j^n - c_{j-1}^n}{\Delta x} = 0 \tag{2.48}$$

Equation (2.49) describes a 2nd order Upwind scheme. The first equation acts as predictor and the 2nd equation is a corrector.

$$\begin{aligned} \overline{c_j^{n+1}} &= c_j^n - u\frac{\Delta t}{\Delta x}\left(c_{j+1}^n - c_j^n\right) \\ c_j^{n+1} &= \frac{1}{2}\left(c_j^n + \overline{c_j^{n+1}} - u\frac{\Delta t}{\Delta x}\left(\overline{c_j^{n+1}} - \overline{c_{j-1}^{n+1}}\right)\right) \end{aligned} \tag{2.49}$$

It is required that the error in solution of c for both schemes will be bounded as time increases. It assumed that the error obeys the same equation as the original scheme. The error is represented by arbitrary complex number $error(t,x) \approx e^{at}e^{ik_m x}$ and is substituted into (2.48) for stability check, $c_j^n = c_j^n + e^{at}e^{ik_m x}, c_j^{n+1} = c_j^{n+1} + e^{a(t+\Delta t)}e^{ik_m x}, c_{j-1}^n = c_{j-1}^n + e^{at}e^{ik_m (x-\Delta x)}, r = u\,\Delta t/\Delta x$:

$$e^{a(t+\Delta t)+ik_m x} - e^{at+ik_m x} + r\left(e^{at+ik_m x} - e^{at+ik_m (x+\Delta x)}\right) = 0 \tag{2.50}$$

Dividing (2.50) by the error, one obtains:

$$e^{a\Delta t} - 1 + r\left(1 - e^{-ik_m \Delta x}\right) = 0 \tag{2.51}$$

For a stable scheme, the error does not grow as the time increases:

$$\left|e^{a\Delta t}\right| = \left|1 - r + r\left(\cos\left(k_m \Delta x\right) - i\sin(k_m \Delta x)\right)\right| < 1 \tag{2.52}$$

Introducing $\beta = k_m \Delta x$ and simplifying (2.52):

$$\begin{aligned} &\left(1 - r + r\cos(\beta)\right)^2 + \left(r\sin(\beta)\right)^2 < 1 \\ &2\left(1 - \cos(\beta)\right)r^2 - 2\left(1 - \cos(\beta)\right)r < 0 \\ &0 < r = u\frac{\Delta t}{\Delta x} < 1 \end{aligned} \tag{2.53}$$

The sufficient condition for stability is bounded Courant number r, known also as Courant-Friedrichs-Levy (CFL) condition.

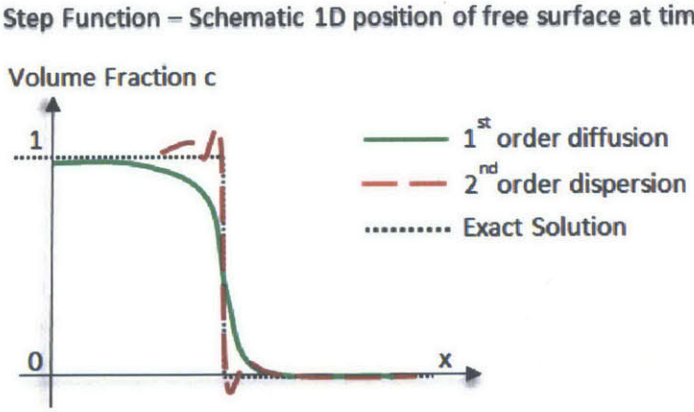

Figure 14. Typical behavior of unsteady-convection discretization schemes.

Similar stability analysis can be performed to equation (2.49), yielding the same results. The 1st order schemes are very robust but suffer from diffusivity, while 2nd order schemes are more accurate than 1st order schemes but introduce oscillations in the solution. Example of such

behavior is shown in Figure 14. It is clear that 2nd order scheme is preferred if one can limit the oscillations. Peric & Muzaferija [38] use complex limiter that bounds the values of c (High Resolution Interface Capturing scheme). The scheme does not allow negative volume fraction or volume fraction greater than one, yet sharp interface is preserved. It blends 1st order and higher order methods depending on local Courant number, and the normal to free surface. For 1st order scheme, additional check is activated that verifies that the amount of fluid being transferred from one cell to another does not exceed the available limit in donor cell.

It is important to notice that although the position and normal to the free surface $c_{water} = c_{air} = 0.5$ is evaluated at each time step, the free surface is not a boundary but rather a part of a continuum. No BC should be prescribed to the free surface in VOF formulation [38].

Wall reflection damping – virtual beach

Star-CCM+ implements damping model to avoid reflections from the walls by adding damping source term in z direction to (2.29). The term is proportional to fluid velocity in z direction w, and it is opposing the flow:

$$S_d = \rho\left(10 + 10|w|\right)\frac{e^{\left(\frac{x - x_{sd}}{x_{ed} - x_{sd}}\right)^2} - 1}{e - 1}w \tag{2.54}$$

x_{ed} – End of damping location, usually at the boundary.

x_{sd} – Start of damping location, in the current study 6[m] before outflow boundary. This damping model allows attenuate wave reflections on boundaries.

Boundary conditions

Six sides of the domain were assigned boundary conditions as follows:

1. Incoming flow (maximum X) – "velocity inlet".
2. Top, bottom, sides –"symmetry plane".
3. Outflow (minimum X) – "pressure outlet".

Half hull was treated as no-slip wall. 6DOF motion module was attached to hull boundary with heave and pitch motion enabled. Mass properties and moment of inertia were taken from Rhino 3D half model. In order to attenuate transient effects the activation of rigid body motion starts 1.5s after the simulation begins. The impact of fluid forces on the rigid body rises gradually (ramp time) from 0 to 100% at additional 1.5s. The simulation was stopped when certain rigid body motion values achieved a steady state (trim angle, CG sinkage, lifting force).

It is important to notice that for the outlet boundary the pressure profile must be defined. The pressure is atmospheric up to free surface, and then hydrostatically increases due to gravity. As

the exact location of free surface fluctuates due to outgoing wave it is a priori unknown. There is a possibility to extrapolate the pressure profile from inside the domain at previous time step, this feature helps to avoid singularities in the domain and increase robustness of the convergence.

Post processing

By default Star-CCM+ keeps fluid motion properties at the last time step, but it allows to record transient behavior of selected properties during the run. For the current study following properties were recorded for each run. Friction and pressure drag on the hull, lift force, pitch moment, CG location and orientation. For the last time step free surface elevation, stagnation line, VOF fraction on transversal sections amidships, at 0.6,0.7,0.8,0.9 LBP, were recorded.

Comparison between theoretical, experimental and CFD results.

Results of model tests for hull 188, which were conducted by Gerritsma, are given in terms of normalized resistance, trim angle, rise of CG, wetted length of the keel and chine wetted area. Experimental results are provided in velocity range $0.5 < Fr_{\nabla} < 3$. In the current section the comparison between R/D, CG rise and trim angle obtained with CFD vs. experiment will be presented. For the same characteristics we will compare the theoretical prediction to experiment for velocities $0.5 < Fr_{\nabla} < 3$. CFD results vs. theoretical prediction would be introduced for higher speeds.

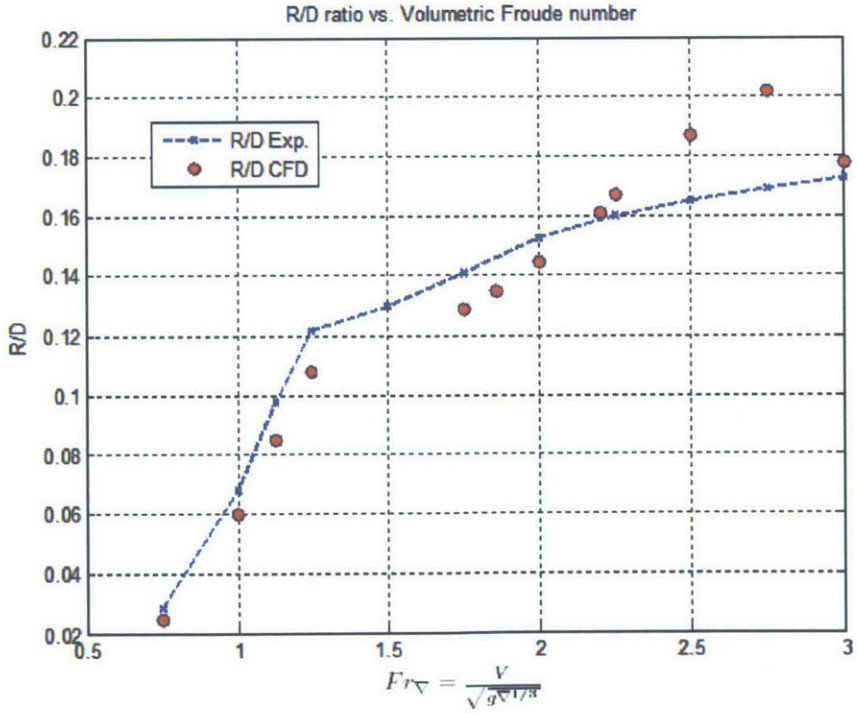

Figure 15. Normilized resistace validation.

Eleven CFD models were prepared and run in the same velocity range covering the displacement, semi-displacement, and early planing regime , $0.5 < Fr_{\nabla} < 3$. Other five CFD models were prepared and run in the full planing speed range $Fr_{\nabla} > 3$, and are presented later on. Resistance/Displacement ratio is shown vs. speed in Figure 15. Area under R/D curve represent a total non-dimensional power needed to thrust a ship at speeds $0.5 < Fr_{\nabla} < 3$. The error may be estimated as integral of absolute difference between 2 curves divided by area under experimental R/D_{exp} curve. In this case the error is 10%. By examining the rise of CG it is evident that although the trend is preserved, the exact dynamic sinkage motion is different, especially at higher Froude numbers. $2 < Fr_{\nabla} < 2.8$

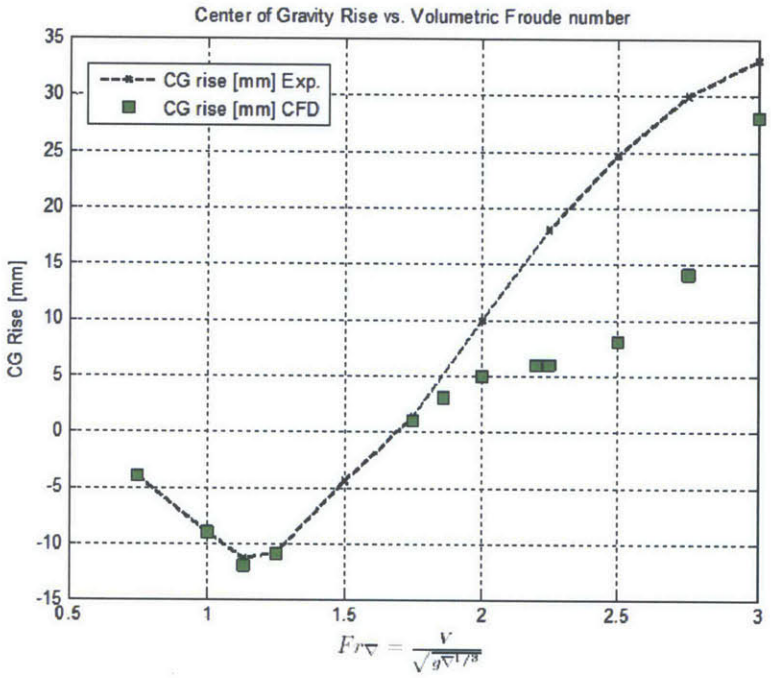

Figure 16. Rise of CG Model 188.

The ship experiences suction force (negative CG rise in Figure 16) at displacement regime as expected, while the positive rise of CG at planing speed is not as rapid as expected. The running trim angle obtained by CFD was corrected by adding $0.7°$ to each point. The reason for the correction is the uncertainty in the VCG between the experimental run and CFD simulation. In CFD run it was assumed that VCG is lying at the intersection of shaft line with the LCG station, while during the experiment the VCG of the vessel was probably higher (no measurements are reported in the original paper of Gerritsma [22]). The vertical shift in VCG during the experiment does not directly affect the total resistance, but slightly influences the moment equilibrium equation (2.25).

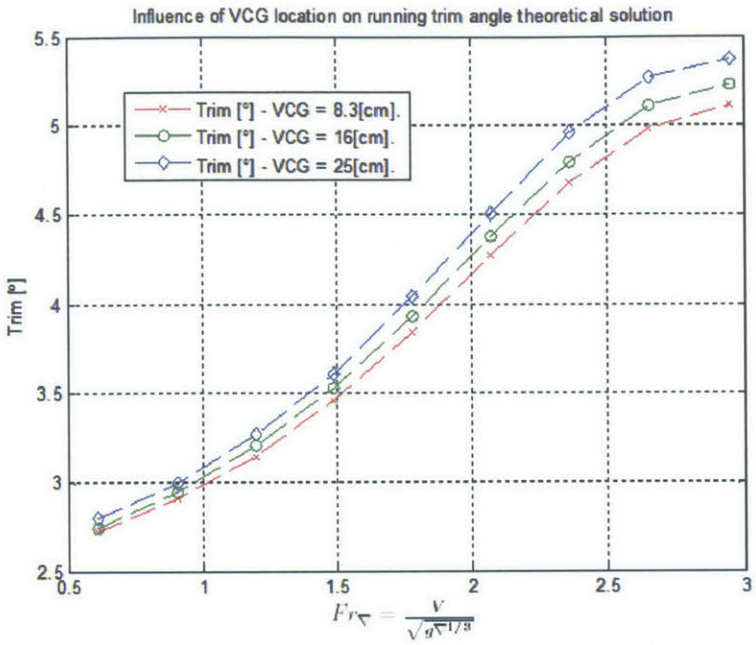

Figure 17. Influence of VCG on running trim angle.

Figure 18. Carriage configuration, model 188.

Figure 17 shows running trim angle vs. speed for the vessel with 3 different VCG above keel, obtained by analytical calculation, with the semi-empirical method described in previous chapter. It is clear that a vertical shift of CG induces an increase of running trim angle. The correction factor of 0.7° corresponds to a physical VCG location of about 0.5[m]. This

relatively high CG position can be explained by the carriage attachment to the hull used in the experiment. Prof. Gerritsma describes in great detail the towing rig configuration [39], which was 3D modelled and presented in Figure 18.

Horizontal forces are transferred to the model by two sliding grips acting on wooden box shown as transparent in Figure 18. When the desired speed is achieved the grips can slide laterally releasing the model. Metallic rod is connected by universal joint at LCG. The rod is passing through sliding cross that is connected to the carriage. Relative movements of the rod inside the cross are measured (heave), movements of the cross relative to the carriage are also measured (surge). Such assembly may significantly increase the VCG because of the weight of the rod.

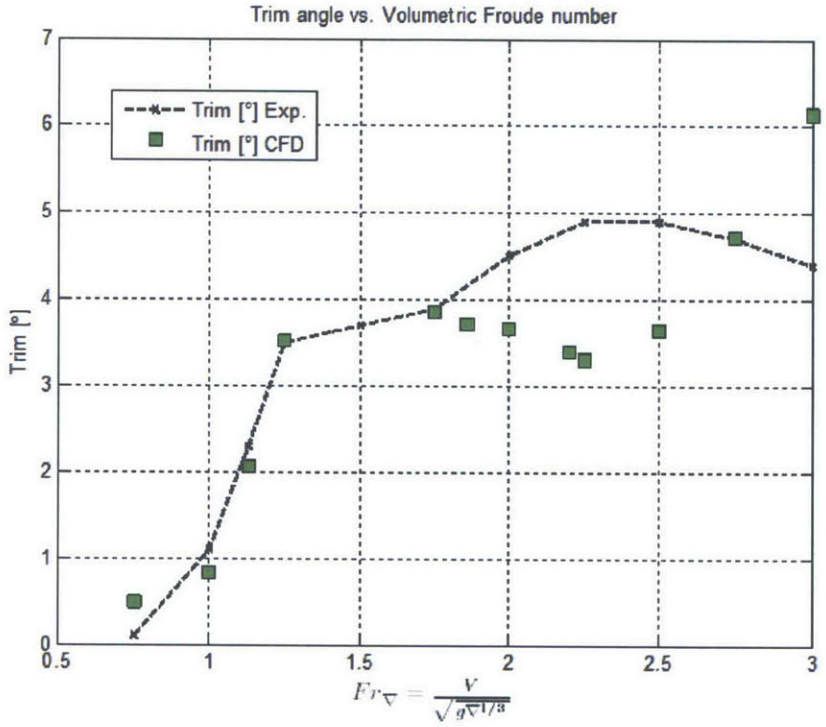

Figure 19. Running trim angle Model 188.

The Rhino 3D model of Figure 18 is based on 2D sketches provided by Gerritsma in [39]. The behavior of running trim angle is shown in Figure 19. It is not clear if this quite heavy towing rig could induce parasitic trim moments to the towed hull. It is seen that the transition between displacement and planing regime indicated by the stabilization and later reduction of the trim angle is captured. Results obtained with analytical method vs. experiment are shown in Figure 20. It is clear that the planing theory method developed earlier does not predict the resistance at displacement regime $Fr_\nabla < 1.25$, furthermore the error between experimental result and theoretical method in the range $1.25 < Fr_\nabla < 3$ is about 15%.

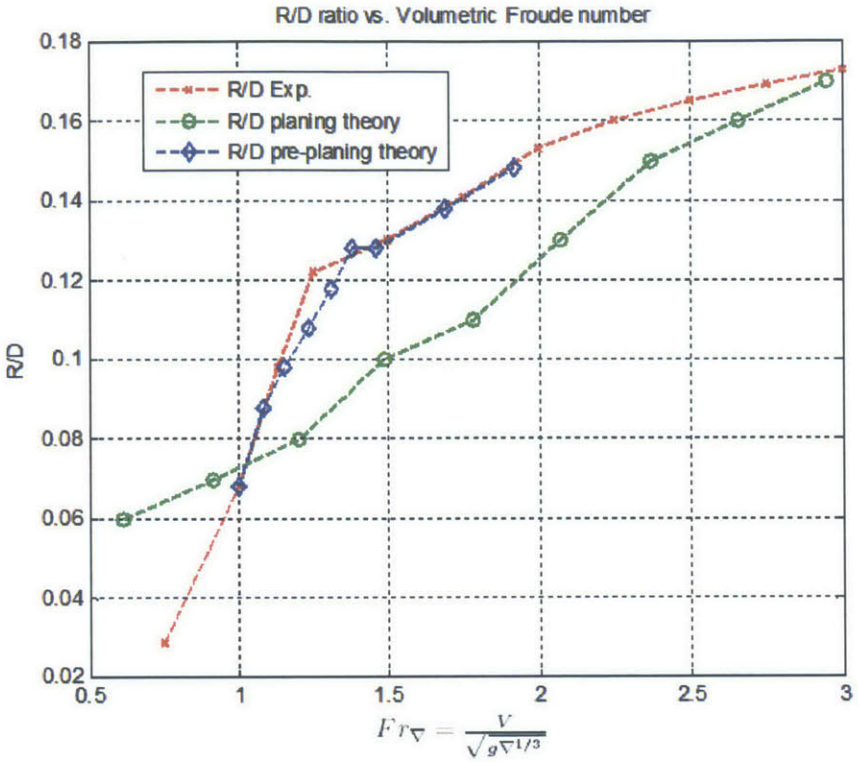

Figure 20. Theory vs. Experiment Model 188.

Savitsky & Brown addressed this issue in [40] by suggesting the use of a so-called pre-planing theory. The pre-planing model was developed by regression analysis incorporating 118 models and 7 hull series. Maxsurf ® suite Hullspeed module incorporated the regression model in [40]. The results obtained by Savitsky pre-planing method are shown in Figure 20. In the whole applicable range $1 < Fr_\nabla < 2$, as expected since one of the series considered in [40] was the Gerritsma hull series, the error in power prediction between experiment and theory does not exceed 2%.

This sanity check was useful to extend the validation of the CFD models to the higher speeds $3 < Fr_\nabla < 6$. In this full planing speed range we can compare CFD results vs. analytical method for both resistance to displacement ratio and running trim angle. The summary of the comparison is presented in Figure 21 and Figure 22. Good correlations between the two methods are noted. The integral error on the resistance prediction, as earlier defined, is about 2%. In conclusion, since the target design speed for the new concept design is $Fr_\nabla = 6$, we can consider the results obtained by the CFD models as sufficiently accurate.

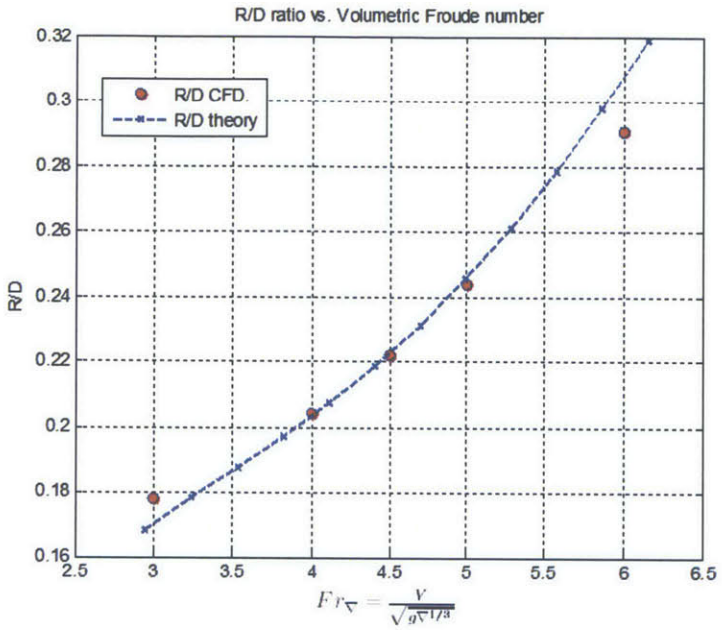

Figure 21. R/D theory vs. CFD model 188.

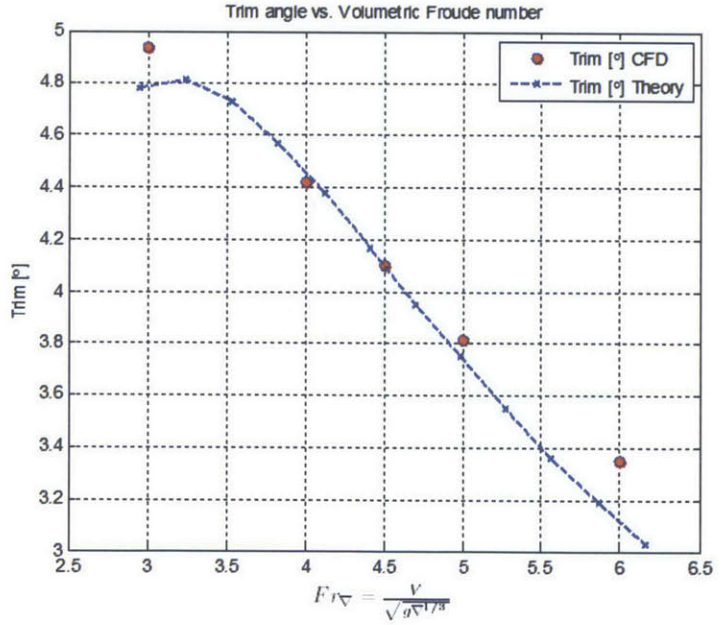

Figure 22. Theoretical trim angle vs. CFD results model 188.

Resistance and trim angle of Model 5115 – Validation Case II

Model 5115 was constructed as ventilated hull with stern stabilizer. It is essential to validate the CFD model with such configuration before applying CFD approach to new design. The model constructed using Rhino 3D with a characteristics as described in Table 5. B_{PT} is not a part of hydrodynamic properties of the vessel because the model includes aft round bilge construction to support the stabilizer.

	Model 5115	Rhino	Error [%]
A_P	119.3	118.9	0.3%
L_P	24.38	24.38	0.0%
B_{PA}	4.9	4.85	5.0%
B_{PX}	6	5.96	4.0%
L_P/B_{PA}	4.98	5.03	-0.9%
L_P/B_{PX}	4.06	4.091	-0.8%
B_{PX}/B_{PA}	0.75	1.23	-63.8%
B_{PT}/B_{PX}	48.7	48.8	-0.2%

Table 5. Comparison between physical hull 5115 ad Rhino model.

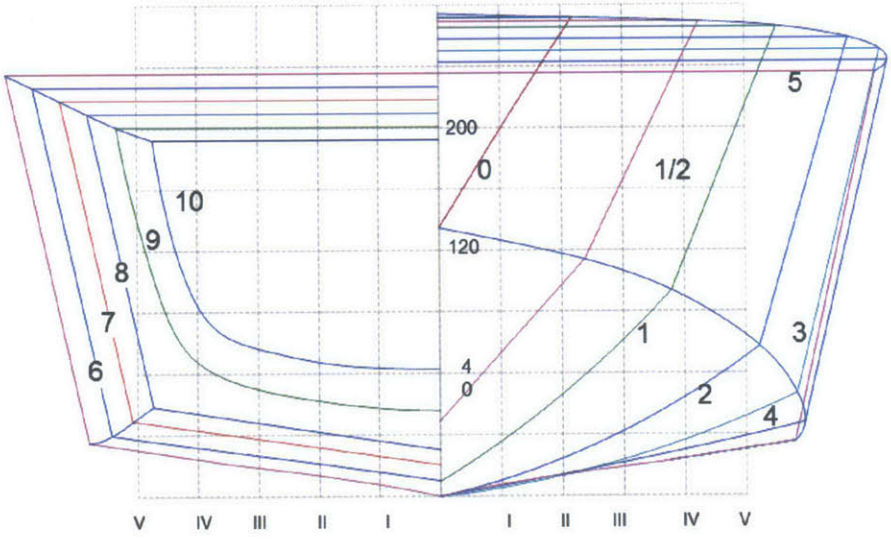

Figure 23. Plan view of model 5115.

Plan view of the model 5115 is shown in Figure 23. The model has relatively low deadrise angle which improves the planing performance in expanse of seaworthiness. Buttocks and water plane lines are presented in Figure 24. It can be seen that there is a cambered wing-shape step located between stations 5-6, moreover the hard chine hull changes to round bilge between station 8-9.

The second step allows to mount Plum stabilizer at the stern. In this configuration LCG is located 2.36 [m] from transom and the displacement of the vessel during the tests was 71.5 [kg].

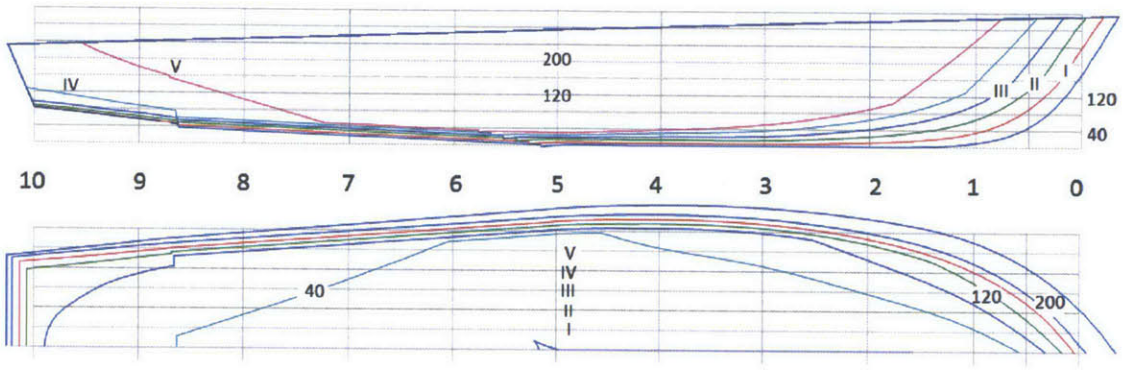

Figure 24. Buttocks and waterplane lines model 5115.

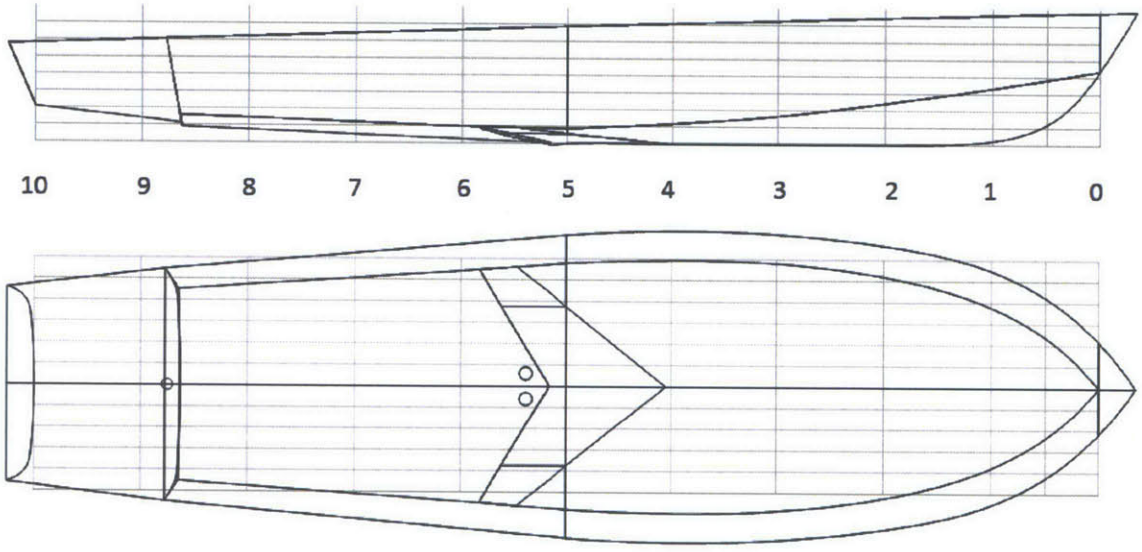

Figure 25. Side and Bottom view model 5115.

Two ventilation openings are located near the trailing edge of the wing. The ventilation allows detachment of the water surface aft of the lifting wing.

Numerical Model Hull 5115

The numerical model of hull 5115 was created by the same principles of model 188. The major difference between the two models is the scale of two models. The computational domain for hull 5115 was adopted to maintain the same non-dimensional parameters as for hull 188. (Time step and mesh size, mesh refinement pattern and alignment).

Comparison between experimental and CFD results.

Hull 5115 was validated at $Fr_{\nabla} = 1.86$ non planing regime. Beyond that point retractable tail – Plum stabilizer was activated. Exact geometry of the stabilizer was not published by Dynaplane inventor, therefore was not included in validation analysis. Estimating the geometry can produce additional discrepancies between CFD and model tests. The comparison between tested values provided by [41] and CFD results is summarized in Table 6.

	Basin tests	CFD	Error[%]
Drag [N]	89.41	89.34	0.08
CG Rise [cm]	1.8	0.9	50
Change of trim [°]	4.8	3.98	17

Table 6.Comparison between Model 5115 basin test and CFD.

The comparison shows good agreement between experimental results and CFD in drag prediction. However, the trim angle is predicted with accuracy of 17%, and CG rise only 50%. The high discrepancies may be explained by the relatively small values under consideration, and the attachment of the stabilizer, that even in retracted position provided some extra lift forces.

Chapter 3 - Dynaplane configuration and Clément's method

The classical method of Dynaplane design was developed by E. Clement during the midst of the past century [42]. The baseline for new Dynaplane design was to apply the existing method on Model 188. The application of the method on deep V hull is presented below:

Design embedded swept wing to support 90% of the displacement. Define non-dimensional lifting coefficient for given deadrise of 25° by (3.1). Parameters of model 188 are given: $\Delta = 23.4[kg]$, $V = 10.023[m/s]$, $B_{PX} = 36.7[cm]$, fresh water.

$$C_{lb\beta} = \frac{0.9\Delta g}{0.5\rho V^2 B_{PX}{}^2} = 0.03 \tag{3.1}$$

For typical swept wing with aspect ratio $AR = 2$ and root chord l_r to tip cord l_t ratio of 4 one obtains:

$$AR = \frac{2B_{PX}}{l_r + l_t} = 2\ , l_t = 0.2B_{PX} = 7.3[cm],\ l_r = 0.8B_{PX} = 29.4[cm] \tag{3.2}$$

Using trim angle given by CFD without the step $\tau(Fr_\nabla = 6) = 3.3°$ one can find the angle to the stagnation line by equation (3.3). Adding the empirical correction due to camber, the angle of stagnation line is given by (3.4)

$$\gamma = \tan^{-1}\left(\frac{\pi \tan(\tau)}{2\tan(\beta)}\right) = 11.1° \tag{3.3}$$

$$\gamma = \gamma + 5° = 16.1° \tag{3.4}$$

In order to construct wing shaped lifting surface with leading edge swept angle γ we need to know trailing edge sweep angle θ and mid-chord angle ϕ. This angles are given by (3.5) and (3.6):

$$\phi = \tan^{-1}\left[\frac{1 - \tan(\gamma)(l_r/B_{PX} - l_t/B_{PX})}{\tan(\gamma)}\right] = 70.6° \tag{3.5}$$

$$\theta = \tan^{-1}\left[2\tan(\phi) - \frac{1}{\tan(\gamma)}\right] = 66° \tag{3.6}$$

Longitudinal Center of Pressure of the wing is a function of section profile and it is usually given as a fraction of mean hydrodynamic chord (M.H.C). One needs to determine the

transversal position of (M.H.C.). Graphical method to find mean hydrodynamic chord position of the wing is given by [43] and is presented here in Figure 26.

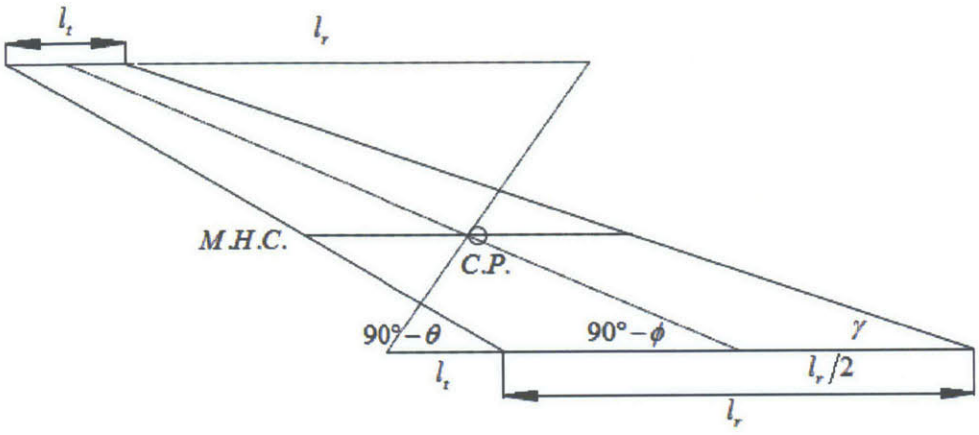

Figure 26. 2D Schematic representation of swept wing.

As the wing is symmetric about X-Z plane the C.P. is positioned on the centerline. After the wing projected area is defined the height and shape of the camber should be defined. Clément's method relies on experimental data of wings without deadrise angle, therefore the lifting coefficient $C_{lb\beta}$ must be corrected to flat wing using the equation (3.7). This implicit formula was solved using MathCad solve block, $C_{lb0} = 0.06$.

$$C_{lb\beta} = C_{lb0} - 0.0065\beta\left(\frac{180}{\pi}\right)C_{lb0}{}^{0.6} \tag{3.7}$$

The method introduces corrections to lift coefficient based on experiments made in Davidson Laboratory:

$$C_{lb0-DL} = C_{lb\beta}/C_{lb0} = 0.5 \tag{3.8}$$

From Figure 27 the correction coefficient for $\phi \approx 70°$ is about 0.6. The updated C_{lb0} can be evaluated using (3.9).

$$C_{lb0} \approx \frac{C_{lb\beta}}{0.6C_{lb0-DL}} \approx 0.1 \tag{3.9}$$

In Figure 27 the circles represent experimental points while lines were obtained from experience, interpolation/extrapolation:

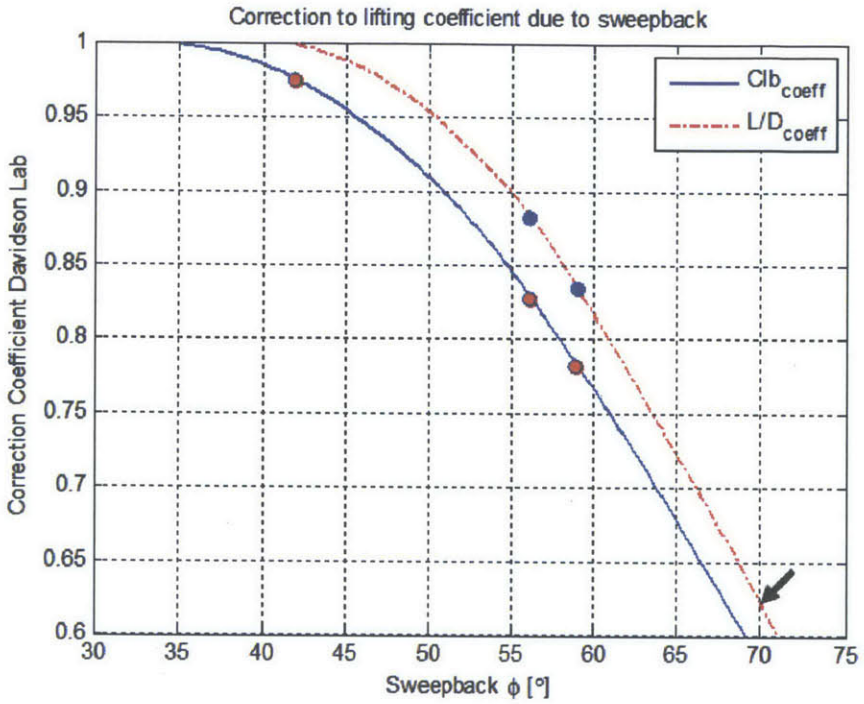

Figure 27. Correction to lifting coefficient due to sweepback.

Experimental data for Lift/Drag ratio vs. C_{lb0} obtained with 3-term Johnson's rectangular section is presented in Figure 28. The experiment was performed on a wing with $AR = 2$ and $\mathrm{Re} = 10^7$. From Figure 28 the $L/D_{Johnson} \approx 10.5$. This number may be corrected to sweptback wing with correction curve in Figure 27 (shown by arrow). The correction coefficient is 0.62. Additional correction coefficient of 0.925 suggested by the method is due to air drag:

$$L/D = 0.925 \cdot 0.62 \cdot L/D_{Johnson} = 6.02 \tag{3.10}$$

The high deadrise angle greatly affects the L/D ratio. Comparing the results to flat plate or Johnson 3-term profile without a deadrise, maximum L/D ratios of 11.5 and 18 respectively can be achieved [41].

In order to choose camber geometry and define the center of pressure of the wing additional parameter should be introduced. $C_{L,d}$ is 2D lifting coefficient for cambered hydrofoil at infinite depth and zero angle of attack.

This parameter can be obtained from Figure 29. Center of Pressure as fraction of M.H.C can be evaluated using Figure 30. For the current design $AR = 2, C_{L,d} = 0.2$ and $l_{cp}/l_{m.h.c.} = 0.52$. It is important to notice that experimental data presented in Figure 29 and Figure 30 was obtained at

trim angle of 2.5° while model 188 designed to operate without the step at running trim angle of 3.3°.

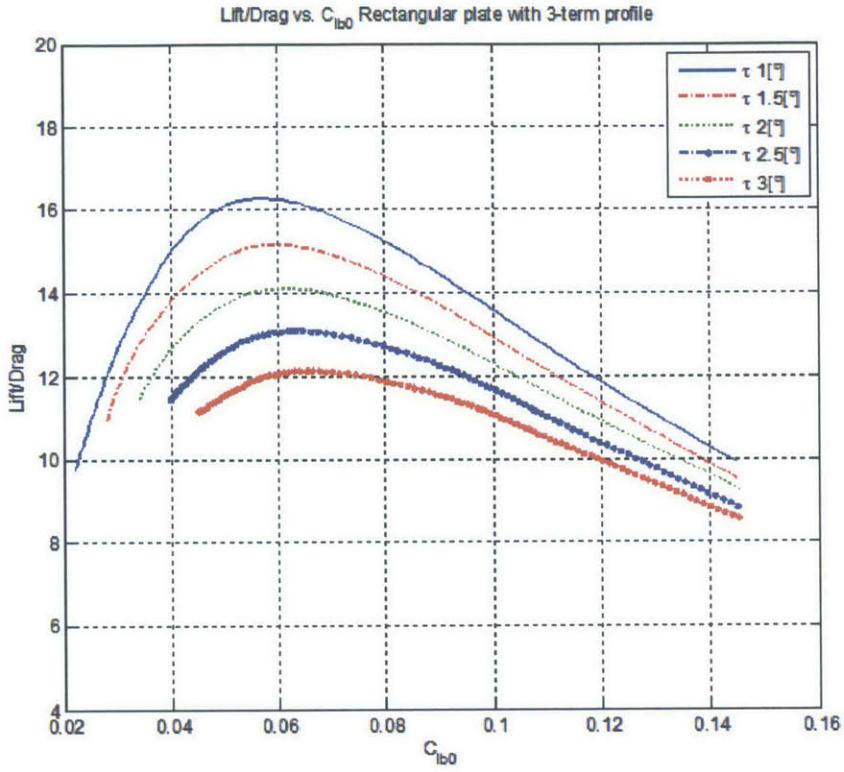

Figure 28. Experemental results for L/D ratio Johnson 3-term profile.

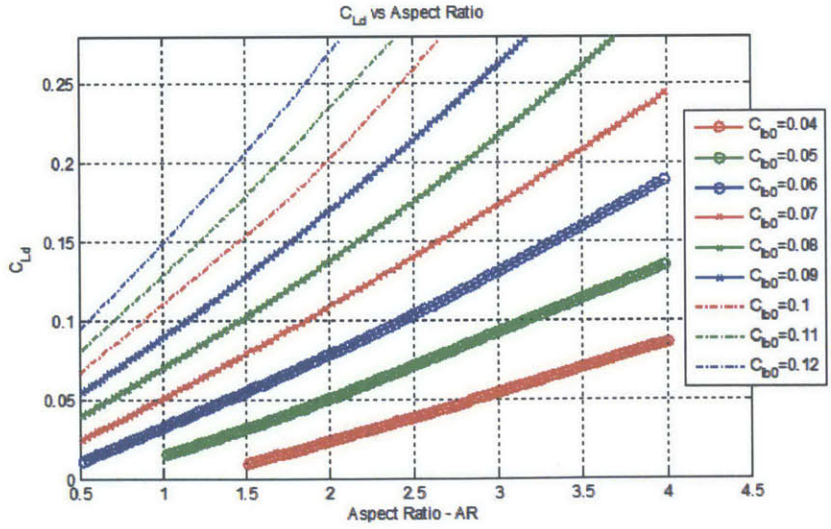

Figure 29. C_{ld} vs. Aspect Ratio - rectangular plate.

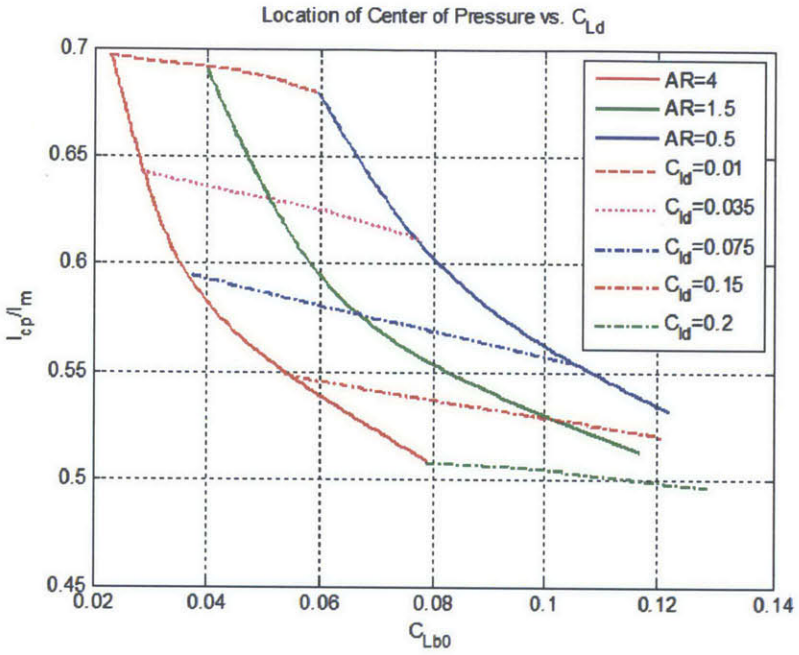

Figure 30. Location of Center of Pressure vs. C_{lb0} rectangular 3-term profile.

After $C_{L,d}$ is determined the exact profile of the camber can be obtained using Vergil Johnson 3-terms profile [44]. The camber section was defined in Rhino 3D using "surface from network of curves" command connecting 3 Johnson sections (at l_r, l_t and M.H.C.) with straight lines. The lines created by projecting leading and trailing edges of the wing Figure 26 on the bottom of the hull. Knowing the chord length c and $C_{L,d}$ the profile was defined by (3.11) with parameters x varying from 0 to 1, y represents the height of the camber.

$$y = \frac{C_{L,d}c}{7.5\pi}\left(-20\left(\frac{x}{c}\right)^{1.5} + 80\left(\frac{x}{c}\right)^{2} - 64\left(\frac{x}{c}\right)^{2.5}\right) \tag{3.11}$$

The final stage of the design includes longitudinal positioning of the wing. As the wing supports 90% of the displacement, moment equilibrium about Y axis at transom (3.12), indicates the distance from AP to Center of Pressure of the wing. Schematic view of model 188 with embedded wing is shown in Figure 32.

$$x_{CP} = \frac{\Delta LCG}{0.9\Delta} = 0.747[m] \tag{3.12}$$

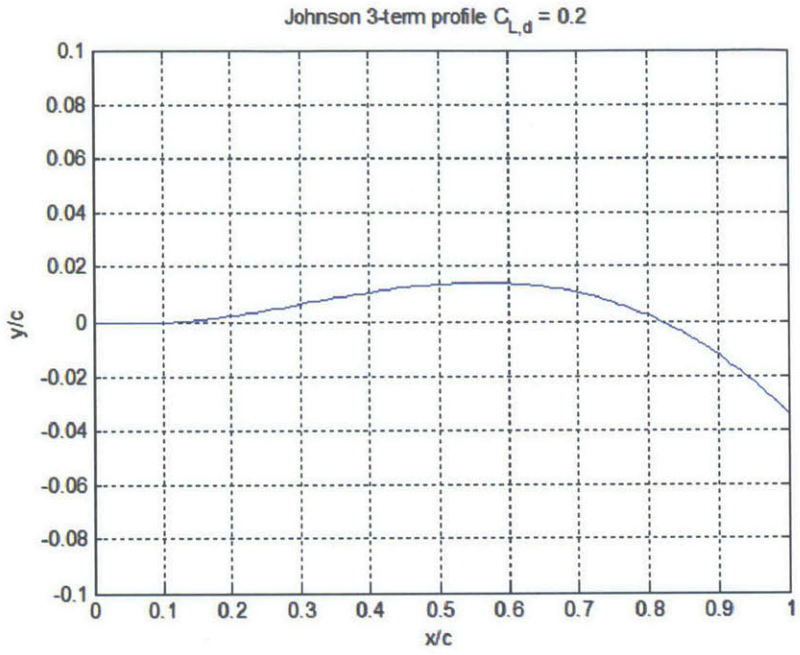

Figure 31. Johnson 3-term profile, Cld = 0.2.

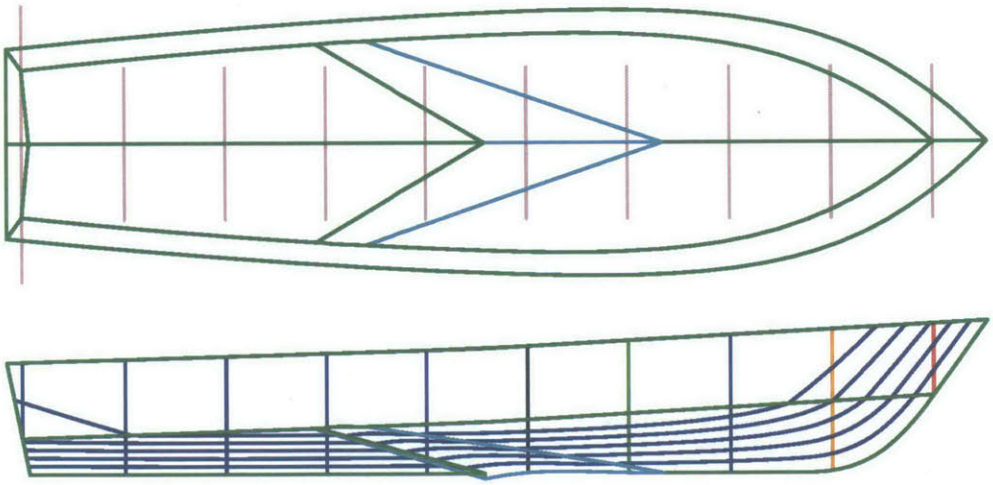

Figure 32. Model 188 with embedded wing.

During numerical simulations of the hull without the stern supporting hydrofoils, vertical external force $F_{ext} = 0.1\Delta$ was applied at transom. Full description of Clement's method and theoretical background is provided by [41]. The chapter herein only highlights the essential steps for its implementation on current design.

Chapter 4 - Reformulated method for Dynaplane design.

Numerical experiment performed with RANSE solver allows to extract geometrical properties of free surface, resultant of hydrodynamic force, spray characteristics for all runs described in chapter 2. The wake and spray of original planing hull are illustrated in Figure 33 and Figure 34.

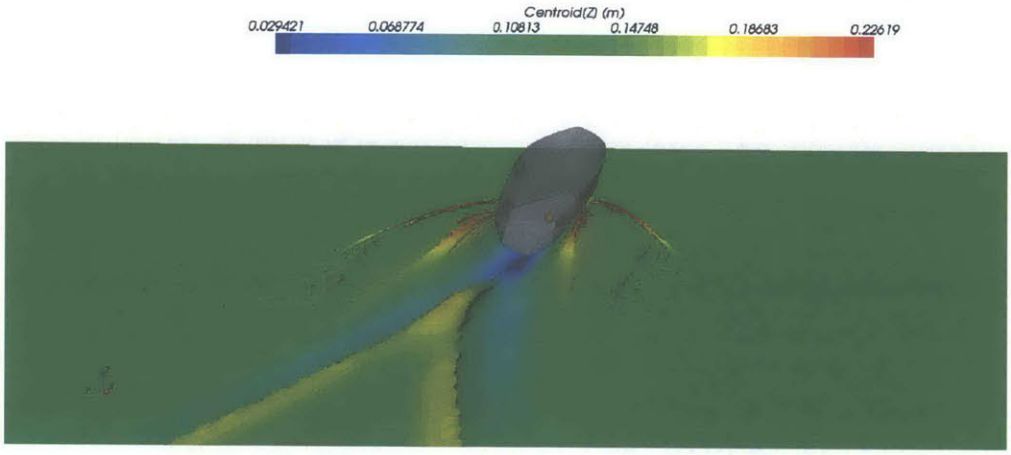

Figure 33. Typical wake profile Fr = 6.

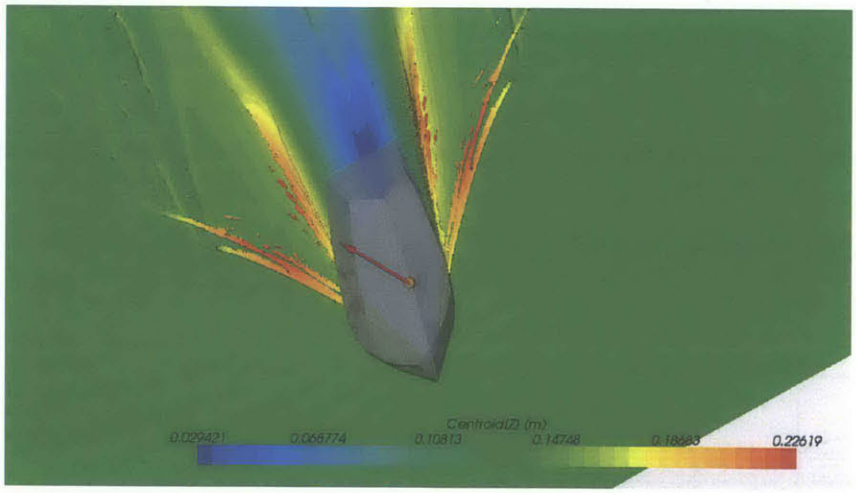

Figure 34. Resultant of hydrodynamic forces. Spray visualization.

Color scale indicates free surface elevation; hydrodynamic forces are shown as a red vector. These forces are applied to the CG of the vessel.

Spray separation can be studied by examining the transversal cuts after achieving steady state planing, as illustrated in Figure 35. The cuts are given at different longitudinal locations measured from AP and defined as fraction of L_P.

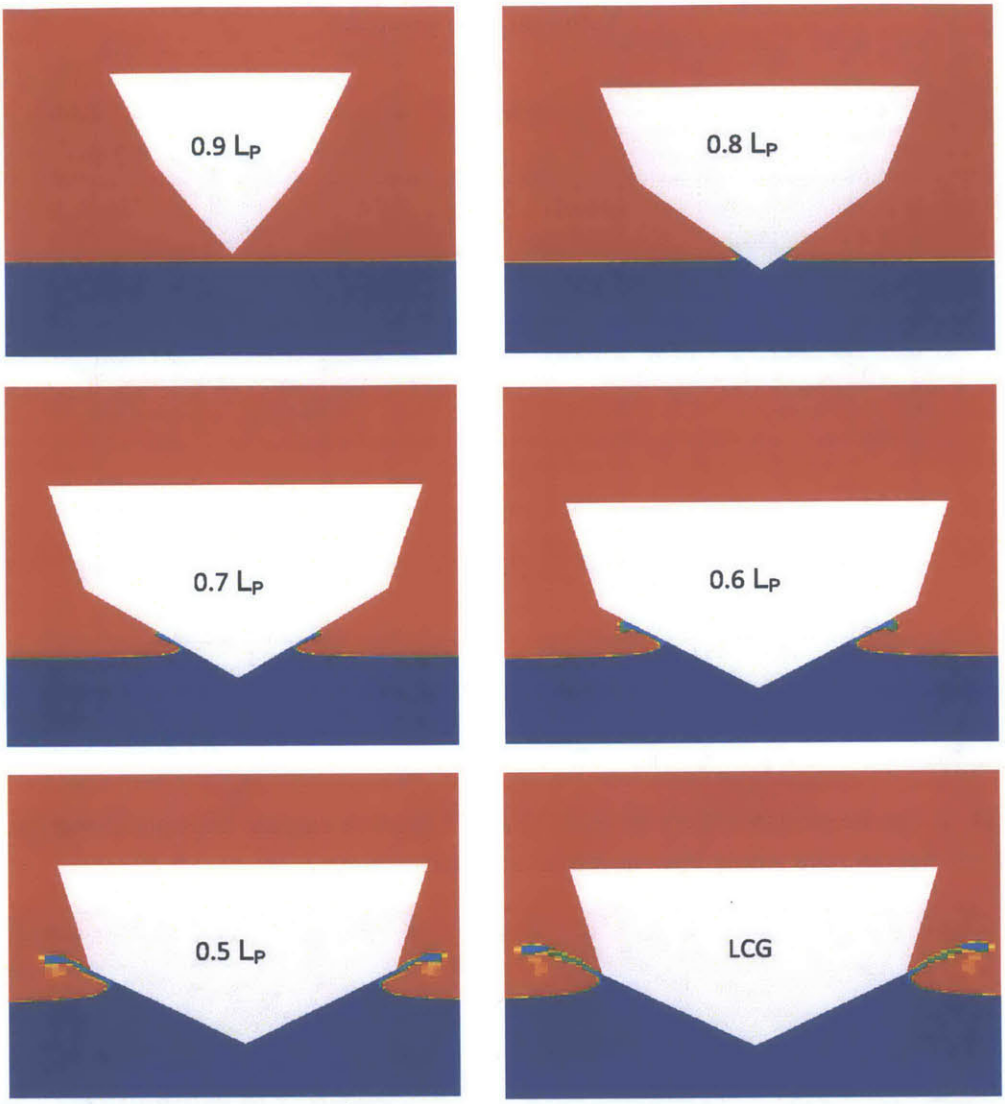

Figure 35. Spray separation transversal cuts.

The sharp interface between water and air is formed in planing mode. Longitudinal cut at centerline of the wave aft of the stern is shown in the non-dimensional graph of Figure 36. It is evident that stern wave is much longer than the hull. The wave height decays almost completely through the computational domain, indicating that its size was chosen correctly. The imposed outflow boundary condition, in fact, is the hydrostatic pressure distribution corresponding to the calm water.

Initial depth of cambered step was chosen using equation (3.11). Original method [41] allows to choose depth of the step about 1% of B_{PX}. It was assumed that lack of the spray rails and open sides of the step (intersection between trailing edge and tip of the wing) would provide sufficient ventilation at the design speed.

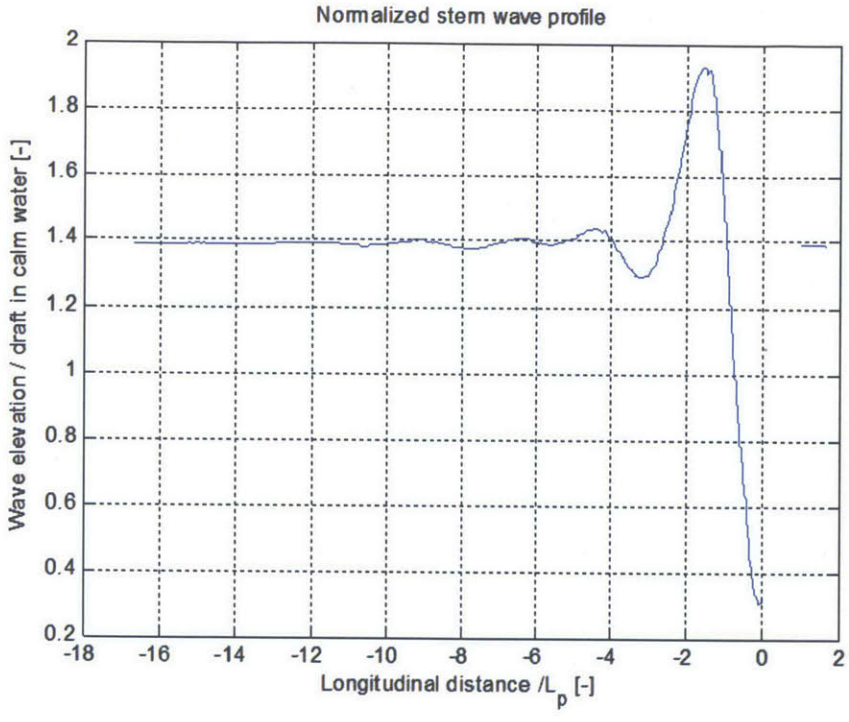

Figure 36. Typical 2D wave profile.

However, as can be seen in Figure 37 and Figure 38 the free surface does not detaches from the edge of the step and the whole bottom remains wetted.

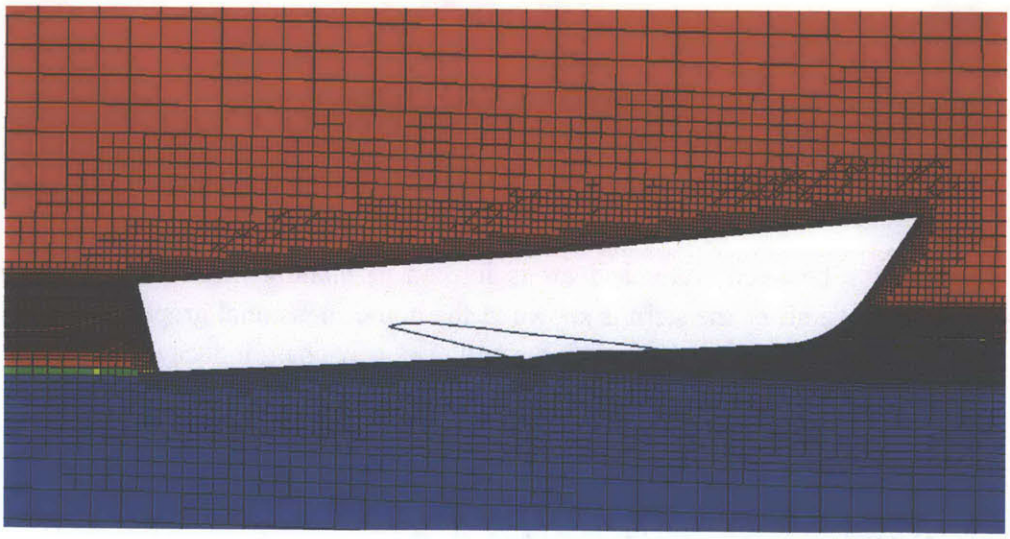

Figure 37. Model 188 with cambered step of height = 1%B_{px} , Fr6.

The wing is far behind the stagnation line and the generated lift barely supports 50% of the displacement. So the hull, naturally, finds a deeper sinkage in order to achieve the required vertical lift force.

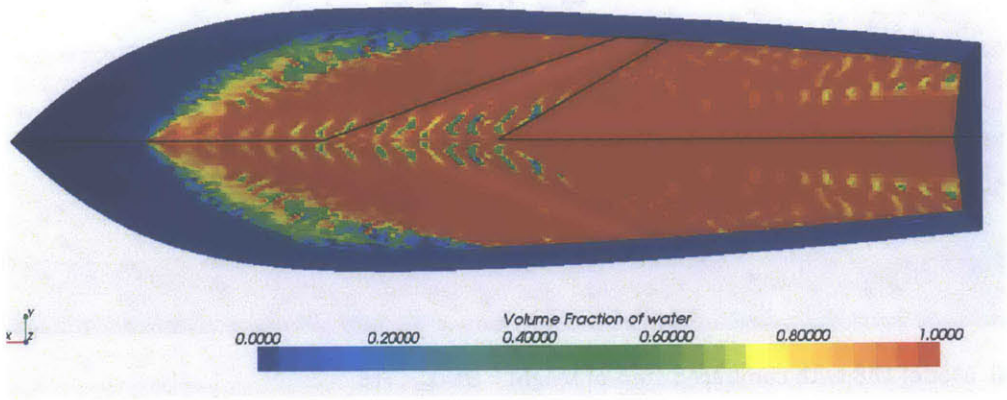

Figure 38. Model 188 step 1%B_{px}, Bottom View.

The pressure distribution on the wing is shown in Figure 39. Running trim angle attained at equilibrium was 3.1°.

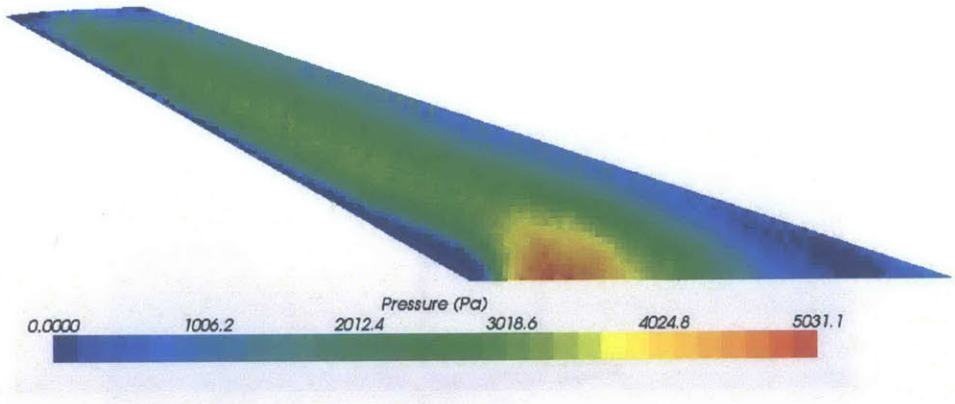

Figure 39. Model 188 step 1%Bpx, Pressure distribution on the wing.

In order to allow easy separation of the flow from trailing edge of the wing the height of the step was increased to 8% of B_{PX}. The geometry change did not alter the constant deadrise of 25°.

After increasing the height of the step proper separation of free surface at trailing edge was not achieved, the results are shown in Figure 40. The lift provided by cambered surface still did not exceed 50% of the displacement.

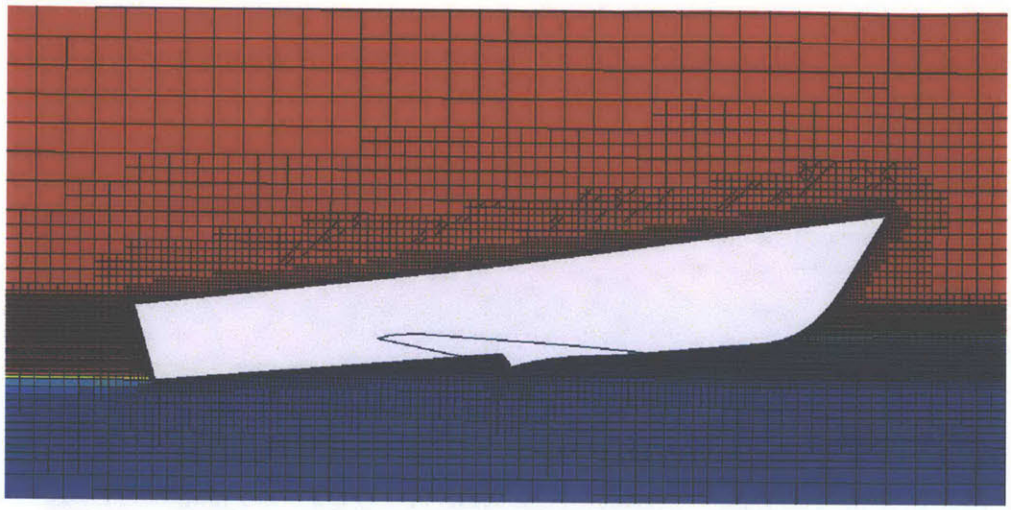

Figure 40. Model 188 with cambered step of height = 8%B_{px} , Fr6.

Given these problems, the hull model was updated using Rhino 3D to incorporate ventilation manifold consisting of 2 vertical pipes connecting to transversal groove cut in the rear side of the step. The ventilation manifold and its position inside the hull are shown in Figure 41 and Figure 42.

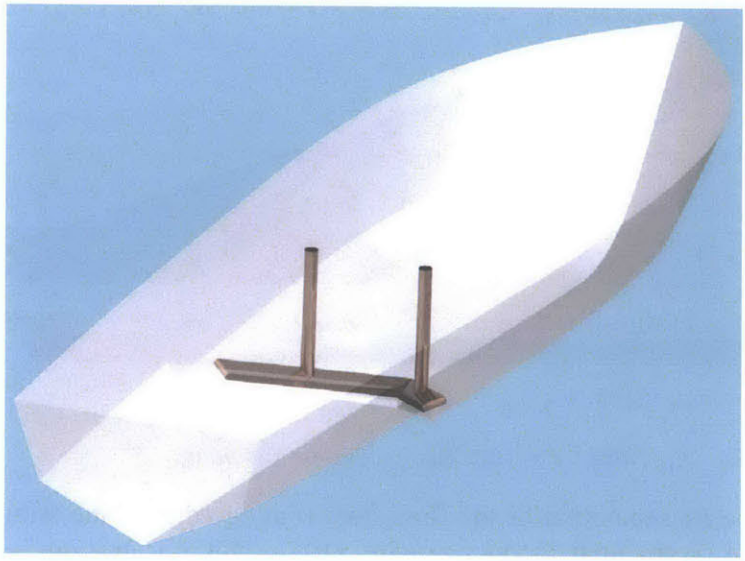

Figure 41. Ventilation manifold configuration.

It is important to notice that the inlet area of the pipes is much smaller than the outlet area in the bottom of the hull, this difference may indicate significant air acceleration on the deck during planing. The connection between the pipes and groove has 90°, therefore vena contracta phenomena may occur, which may lead to deterioration in coating layer of the pipe, enhanced corrosion, structural vibration and noise. For the current preliminary design stage the structure

of the ventilation system is sufficient, as it provides the necessary pressure drop in the vicinity of the trailing edge. In a detail design phase the manifold should be redesigned, taking into account the considerations mentioned above.

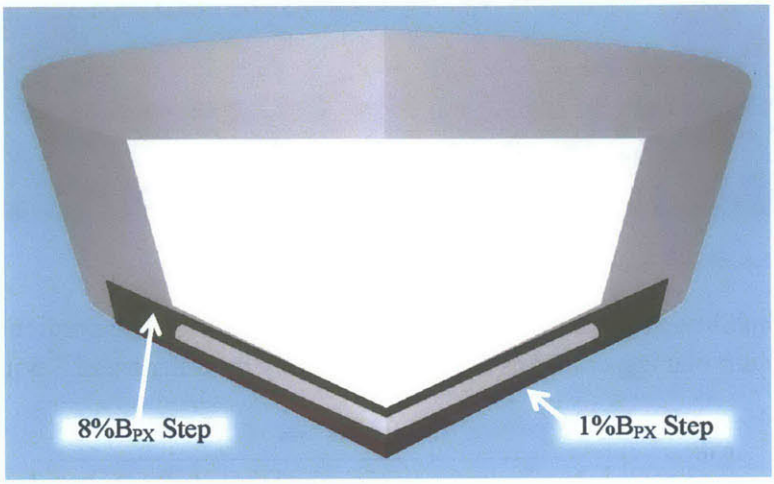

Figure 42. Grooved step - view from transom toward the bow.

The new layout of the bottom of the vessel is illustrated in Figure 43. Full ventilation of the bottom behind the step was achieved after the application of geometrical change. The instantaneous orientation of the hull is shown in Figure 44. After reaching 7 seconds of physical time the simulation did not converge to steady state values, since it was affected by periodic oscillation. The time histories for pitching angle and rise of CG are presented in Figure 45 and Figure 46.

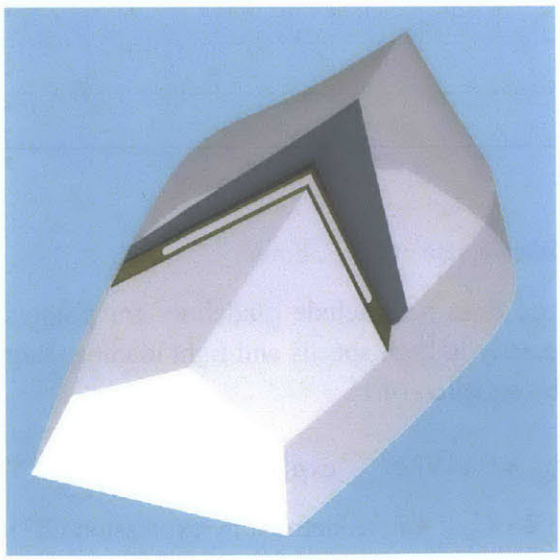

Figure 43. Cambered wing, step and ventilation outlet - bottom view.

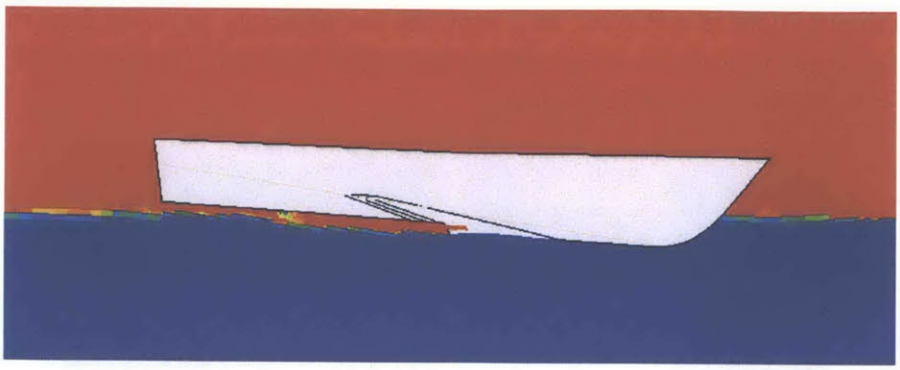

Figure 44. Fully ventilated bottom side view.

The dynamic instability in pitch can be classified as porpoising. The prediction of porpoising inception for modern planing craft was studied extensively by Celano and Savitsky [45], [17].

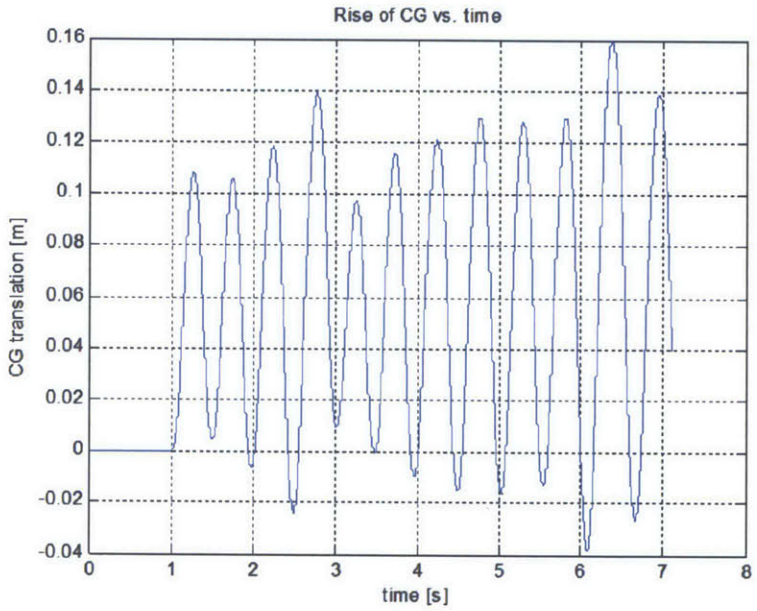

Figure 45. Fully ventilated bottom, rise of CG vs. time.

Although Clement's method does not include guidelines for porpoising limits, such dynamic instability may occur especially at high speeds and light loading. Regression line developed by Celano can be expressed by equation (4.1).

$$\tau_{crit} = 0.1197\beta^{0.7651}\exp\left(15.7132\sqrt{C_{L\beta}/2}\beta^{-0.2629}\right) \tag{4.1}$$

Equation (4.1) is valid for $2 < C_v < 4.7$, as defined by expression (2.1).

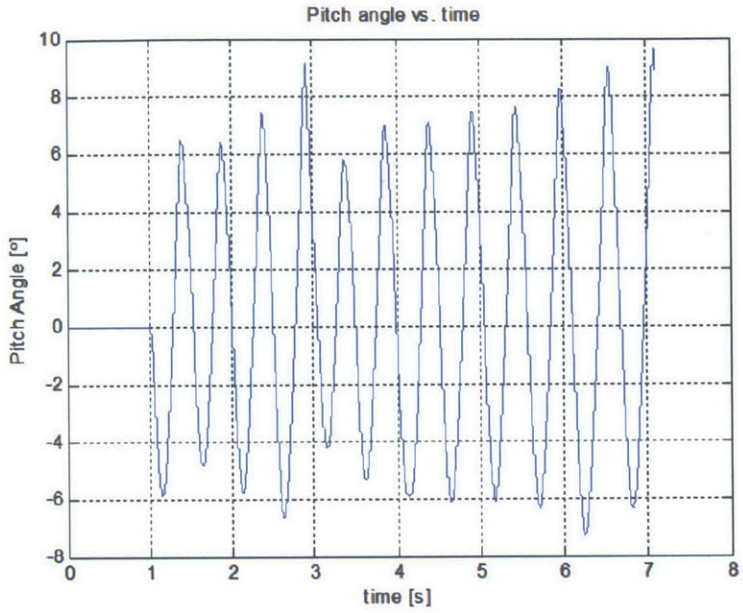

Figure 46. Fully ventilated bottom, pitch angle vs. time.

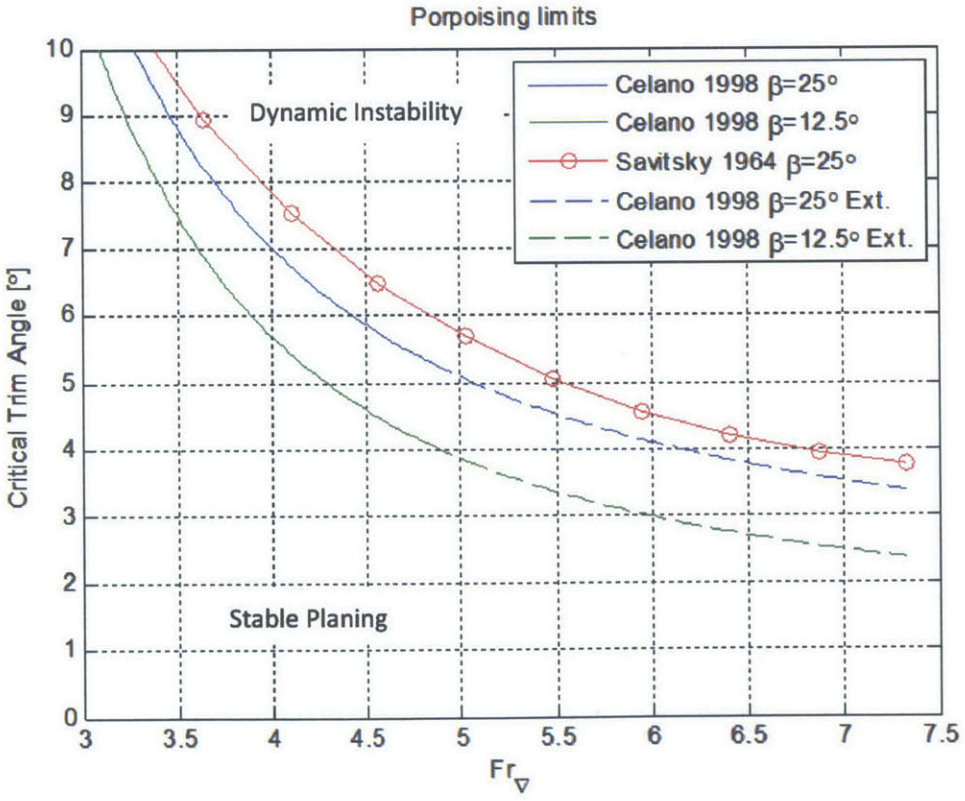

Figure 47. Porpoising limits for prismatic planing hulls.

For the current study the displacement of the vessel is given and so breadth over chines and deadrise, therefore the lift coefficient $C_{L\beta}$ is only function of hull velocity. The critical trim angle for porpoising inception is plotted in Figure 47.

Solid lines indicate the results obtained by Celano, below $Fr_{\nabla} \approx 5$. Above this point the dashed lines indicate the extrapolation of formula (4.1) outside its tested range. Data provided by Savitsky covers the required range of speeds including the design point at $Fr_{\nabla} = 6$, but it refers only to limited deadrise angles of $\beta = 0° - 20°$. The red curve presented in Figure 47 is extrapolation of tested data to $\beta = 25°$. It is important to notice that for the low deadrise angle $\beta = 12.5°$ (original series 62 hull) the porpoising limits are stricter than for high deadrise angle.

With lack of experimental data on porpoising limits in the vicinity of design point, one may assume that running trim angle is above $4°$, therefore it can be expected that the hull orientation doesn't converge to steady state results during the numerical experiment. The minimum angle of attack that is required to lift 90% of the vessel exceeds the porpoising stability limit. In order to confirm or refute this hypothesis an exploration study was done with fixed trim and sinkage.

In order to explore the variation of lift coefficient C_L and drag coefficient C_D (4.2) of cambered wing as function of trim and sinkage 9 additional simulations were performed. The results were organized in 3x3 matrix. Each simulation had fixed trim and sinkage, spanning trim range from $-2°$ to $7°$ rotating about the center of gravity. The sinkage was altered in a range of ± 4 [cm] with respect to static draft.

$$C_L = \frac{F_{lift\_wing}}{1/2\,\rho V^2 A_w} \; ; \; C_D = \frac{F_{drag\_wing}}{1/2\,\rho V^2 A_w} \tag{4.2}$$

C_D	Trim [deg]		
Draft[cm]	-2	2.5	7
-4	-0.008	0.149	0.3
0	-0.008	0.15	0.305
+4	-0.008	0.147	0.303

Table 7. Drag coefficient vs. trim and sinkage (wing only).

C_L	Trim [deg]		
Draft[cm]	-2	2.5	7
-4	0.043	0.027	0.042
0	0.043	0.014	0.035
+4	0.043	0.046	0.05

Table 8. Lift coefficient vs. trim and sinkage (wing only).

Vessel velocity corresponding to $Fr_{\nabla} = 6$ is $10.049[m/s]$, Half wing area $A_w = 3.23 \cdot 10^{-2}[m^2]$. Java macro was written in order to generate 9 simulation files. The macro is based on the validation case simulation. The code of macro script is attached in the Appendix-I. The Java macro was developed using Star-CCM+ java libraries using NetBeans (Integrated Development Environment) tool version 7.3.

The results are presented in Table 7 and Table 8. Wetted portion of the bottom is shown in Figure 48. From the figure it can be seen that in all the runs the stagnation line is far from the leading edge of the wing. At negative trim some backflow occurs, that explains the negative values of C_D. Full ventilation of aft body is achieved in case $(-2°, -4[cm])$ and $(2.5°, 4[cm])$, in all the cases the lift produced by the wing is not sufficient to dynamically support 90% of the body. Table 9 is different representation of the data that was presented in Table 8, and it describes how much lift is actually attained. Recall the design point of $90\%\Delta$. It is important to notice that at trim 7° the vessel will experience porpoising.

F_{lift_wing}/Δ	Trim [deg]		
Draft[cm]	-2	2.5	7
-4	69%	44%	68%
0	69%	23%	57%
+4	69%	74%	81%

Table 9. Provided lift as portion of the displacement.

Exploration study reveals that the key feature in achieving the required lift is the match between wing position and the stagnation line. According Bernoulli's principle the pressure at stagnation line is maximal and necessary lift will be attained. In order to find longitudinal position of the stagnation line for each trim angle at equilibrium, heave degree of freedom was released.

The position of stagnation line was found for fixed trim at 3,6,9 degrees, converged results are shown in Figure 50. The results indicate that the match between stagnation line and the wing will occurs between trim angles of 3 and 6 degrees.

Narrowing the search of matching stagnation line with wing position additional simulations were performed for fixed trim angles 3.5,4,4.5,5 degrees. Close match was achieved at last tested point, as shown in Figure 49. The figure shows that the hull is almost completely supported by the wing (90%). White arrows indicate normalized shear stresses over the bottom. Examining direction of shear allows determining exact position of stagnation line.

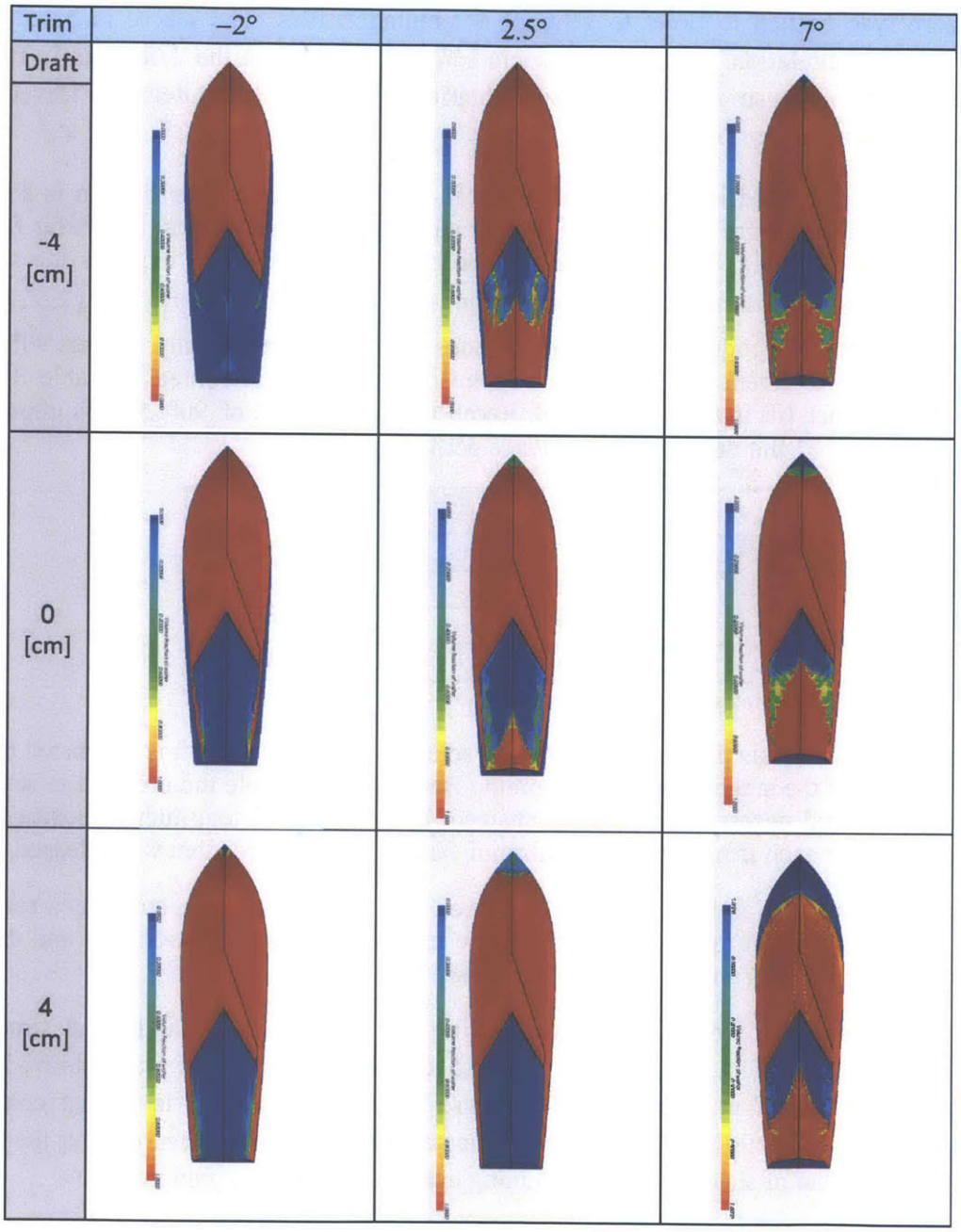

Figure 48. Separation of free surface from bottom as function of trim and sinkage.

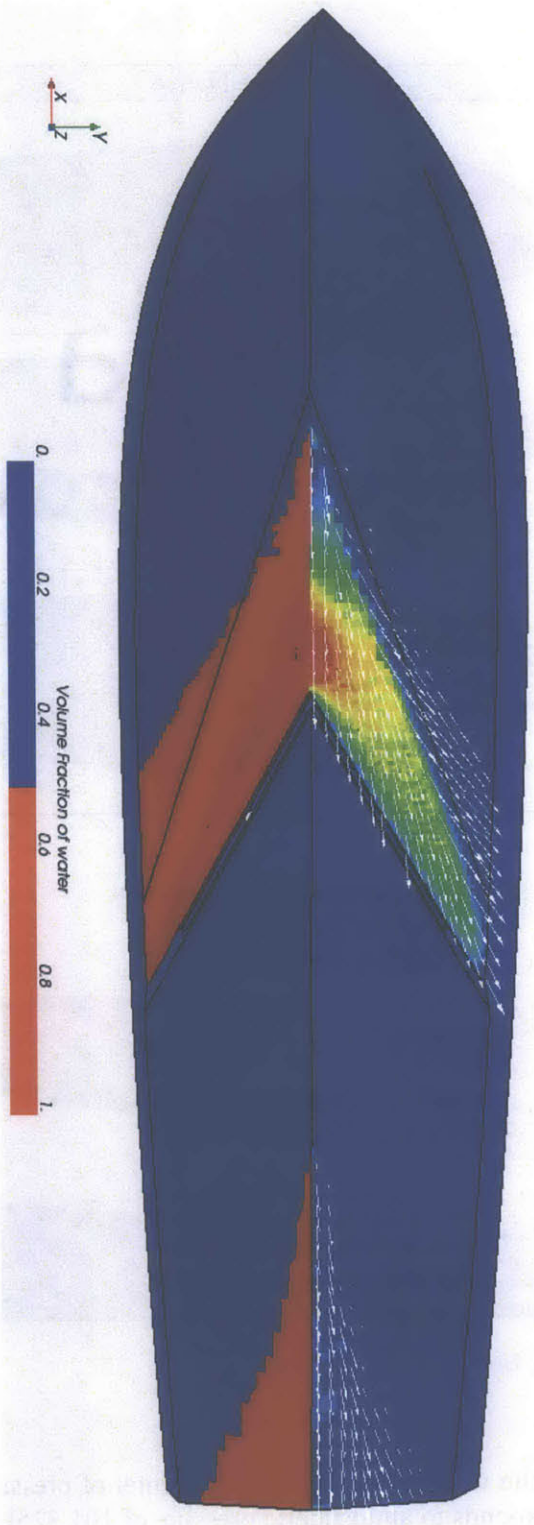

Figure 49. Stagnation line formation - free heave, fixed pitch 5[deg].

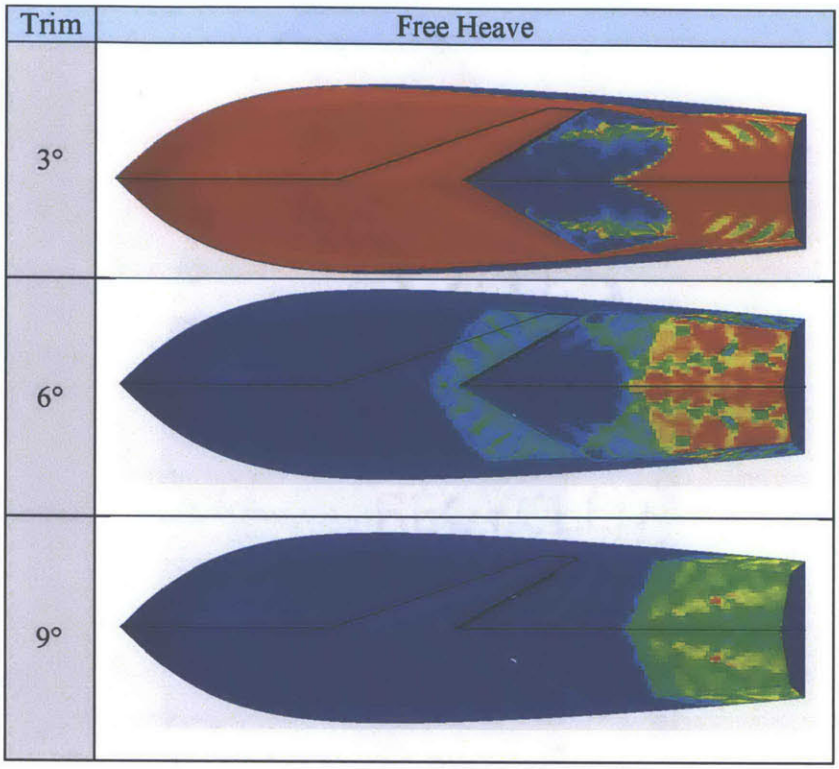

Figure 50. Position of the stagnation line as function of trim anle.

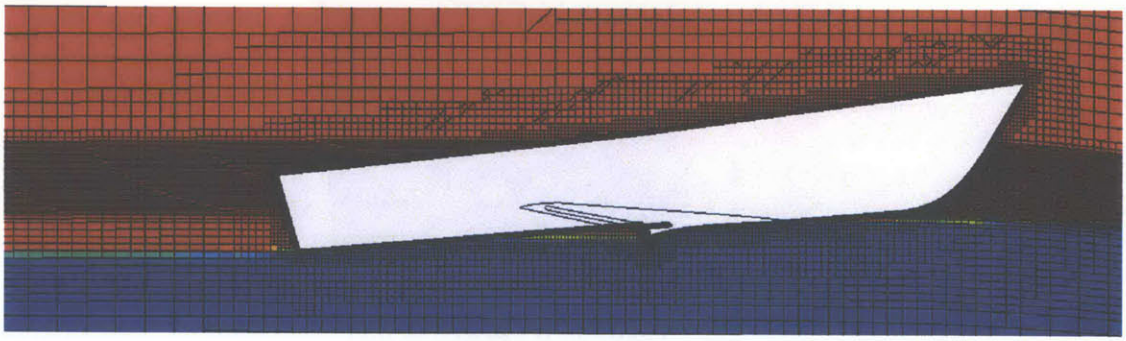

Figure 51. Fixed pitch 5[deg], free heave - side view.

Pressure distribution over the wing is indicative of the center of pressure position. Zero pressure level at leading edge corresponds to atmospheric pressure of 101.325kPa.

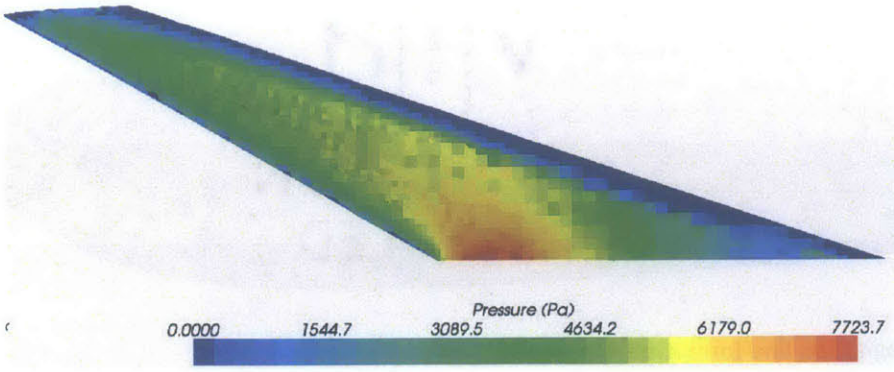

Figure 52. Pressure distribution over the wing, fixed trim 5[deg].

Hydrodynamic lift forces created by the wing at fixed trim of 5° provide sufficient lift to support 90% of the hull. Analyzing the results from 5° run, one can conclude that the geometry of the hull may yet be improved. Wetted aft part of the hull introduces additional drag as can be seen in Figure 49, this portion of the bottom may be raised or removed. Furthermore, we can superimpose the position of the wing, initially created by Clement's method and the location of stagnation line obtained from validation study at design speed. Rhino outline sketch is superimposed on Star-CCM+ VOF screenshot of original hull model 188 at $Fr_{\nabla} = 6$ in Figure 53.

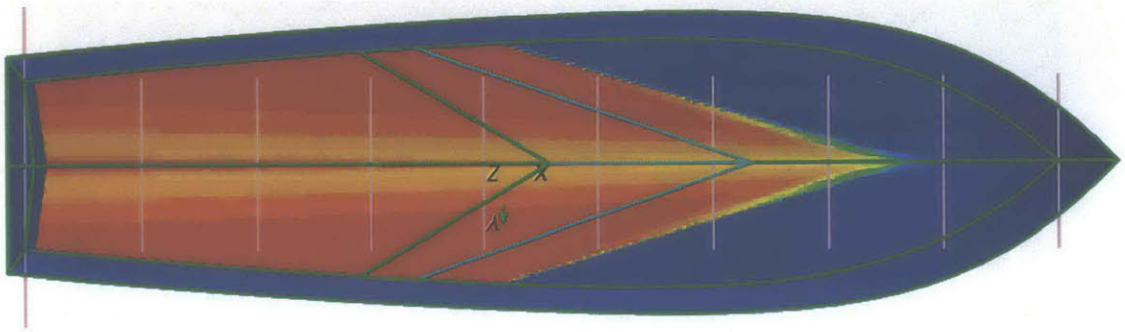

Figure 53. Model 188 Bottom view at Fr=6.

In order to match the outline of the vessel the screenshot was taken in parallel projection with camera oriented to –Z in ship fixed reference frame. It is evident that the wing is behind stagnation line. The shear stress vector field is plotted in Figure 54, and it allows to determine the position of the stagnation line.

Red shaded area at upper part of the hull represents wetted portion of the bottom. Red shaded area at lower part of the hull represents areas with high pressure, thus the spray root is marked as wetted area it does not contribute to pressure field/lifting force. The red area near the bow corresponds to air drag during planing.

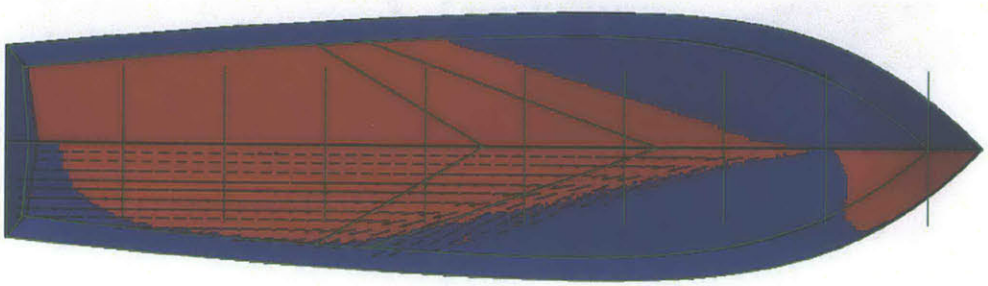

Figure 54. Stagnation line formation Model 188, Fr=6.

From Figure 53 and Figure 54 it is evident that the location of the wing can be moved significantly forward in order to match the position of the stagnation line. At this stage of the design the wing was translated 200[mm] in positive X direction (forward). The new final Rhino model is shown in Figure 55.

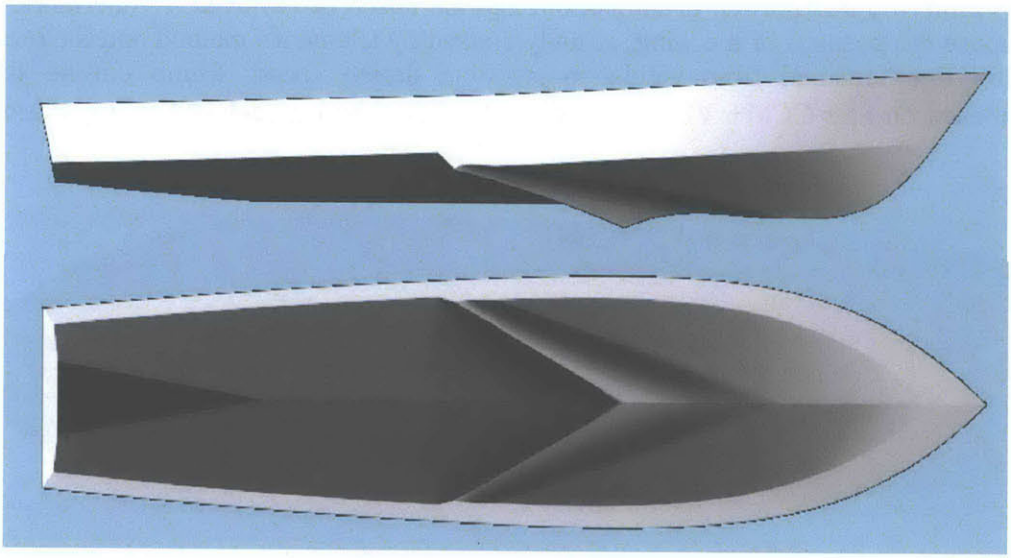

Figure 55. Hull modifications - raised stern, updated camber.

The feasibility of the design is in question as running trim angle of 5° brings it into porpoising regime. Reducing trim angle while keeping the same lift can be achieved by increasing wing camber. 2D lift coefficient of 3-term Johnson's profile is given by (4.3) according to [46]. This coefficient was calculated by Clement's method eq. (3.9).

$$C_{lb0}(\tau) \sim \frac{\pi}{2}(\tau + const.) \tag{4.3}$$

Assuming decrease of running trim angle from 5° to 3.5° in order to avoid porpoising the change in camber can be easily calculated.

$$C_{lb0}(5°)-C_{lb0}(3.5°)\sim\frac{\pi}{2}(5°-3.5°)\frac{\pi}{180°}\Big/\cos(\beta)\approx 0.05 \qquad (4.4)$$

Following eq. (4.4) and (3.9) new value of $C_{lb0}=0.15$ is obtained. From Figure 29 the corresponding camber has $C_{L,d}=0.37$, for aspect ratio of 2. Camber update was incorporated into design; this update is illustrated in Figure 55.

Configuration and validation of the Hydrofoils

Trim control of planing vessel is a key factor in dynamic stability and ride quality. Plum's stabilizer could be used to achieve adequate trim control, as tested by Clement [41]. Main disadvantages of the device are large amount of moving parts such as pistons, springs, pivot joints. The stabilizer requires complicated hydraulic system to control piston position. Clement in his study suggested installation of V surface piercing hydrofoil. Originally designed by Baker and Lang the hydrofoil is based on NACA 16-510 profile. In the current design, state of the art supercavitating hydrofoils designed by Prof. Brizzolara were chosen. The procedures of foil design and test results obtained in TU Berlin Cavitation tunnel (K27) are discussed in [47].

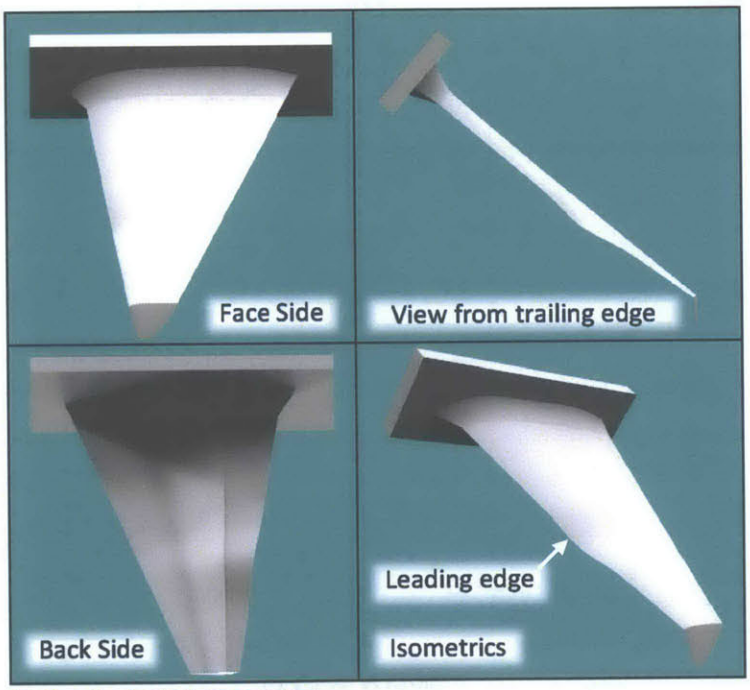

Figure 56. Supercavitating hydrofoil geometry.

Major advantages of the supercavitating hydrofoils are high L/D ratio in cavitating regime, fixed geometry, roll stabilizing effect. The foils can be designed not to exceed overall beam of the vessel. The lower part of the foils can be kept above the baseline. The dimension requirements are very important for planing craft operating in shallow water or confined areas.

Foil breadth requirement is important for safe berthing of the vessel or mooring alongside to other ships.

RANSE simulation was performed on single foil piercing free surface at zero angle of attack. The results were compared to the full scale experiment, before attaching the foils to the hull. Figure 56 illustrates the geometry of the foils; Figure 57 shows lift and drag coefficients obtained in cavitation tunnel.

First phase in hydrofoil RANSE simulation is the definition of computational domain and estimation of prism layer thickness. Reynolds number is defined based on foil chord length $c_{foil} = 215[mm]$ at designed draft by eq.(4.5) with inflow velocity $V_f = 10.5[m/s]$.

$$\mathrm{Re}_{foil} = \frac{V_{foil} c_{foil}}{\nu_{fw}} = 2.358 \cdot 10^6 \tag{4.5}$$

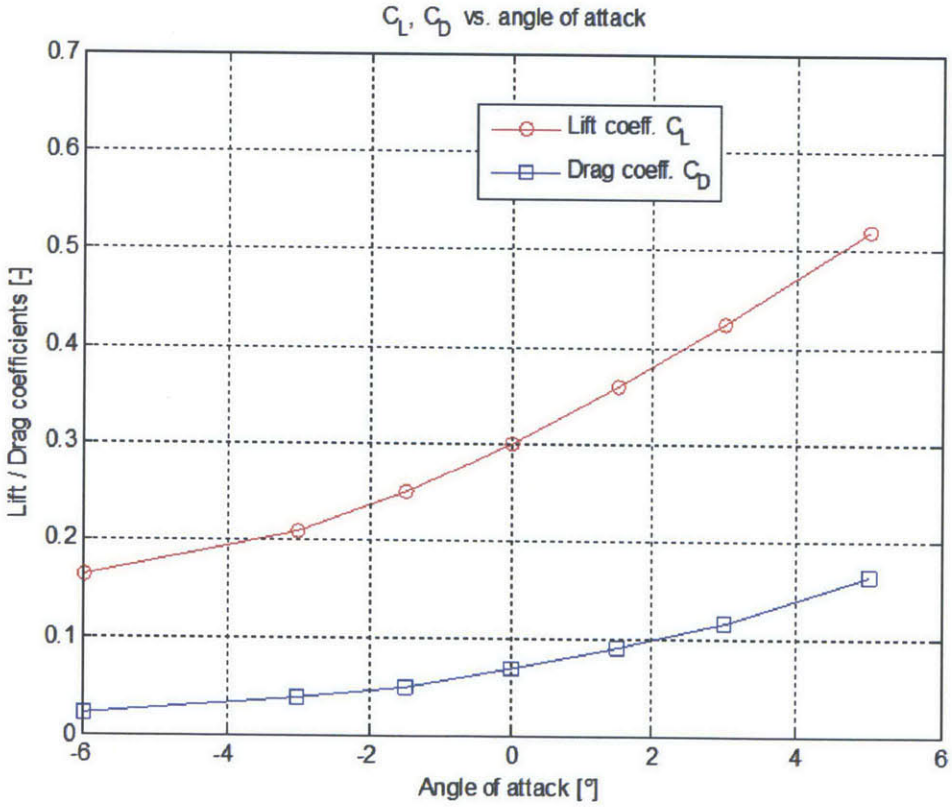

Figure 57. Hydrofoils' Lift & Drag vs. angle of attack. Tunnel testing results.

In hydrofoil simulation, similar to pervious cases the size of the first cell was chosen to maintain y+ of 30, as defined by equation (2.28). Wall shear stress was estimated as

$\tau_{w\_foil} = C_{f\_foil}\rho V_f^2/2 = 216.2[Pa]$, with $C_{f\_foil} = 3.923 \cdot 10^{-3}$ evaluated by equation (2.6). Consequently, the thickness of the first layer was 0.062[mm].

Supercavitating hydrofoil develops large cavity behind the trailing edge, in order to capture this phenomena the domain extended 23 chord lengths behind the trailing edge. The dimensions of computational domain were normalized by hydrofoil chord length at designed draft, and are given in Figure 58. Breadth of the computational domain was 8 chord lengths. The domain was discretized by 0.9M cells. Axis origin in Figure 58 indicates the position of the free surface at calm water. In this validation case all boundaries are defined as rigid, no mesh morphing was enabled. Unsteady transient solver was used with time step $5 \cdot 10^{-5}$[s] and five inner iterations. The run was configured as multiphase case with water/air segregated phases; due to surface piercing setup no transition model between the phases was defined.

Figure 58. Hydrofoil validation - size of computational domain.

After 800000 iterations and 160000 time steps 8 seconds physical time was reached. The comparison between experimental measurements and CFD prediction, for drag and lift coefficients at zero angle of attack is presented at Table 10.

	CFD	Cavitation tunnel	Error [%]
Lift Coefficient	0.34±0.015	0.3	13
Drag Coefficient	0.063±0.002	0.068	7.3

Table 10. Hydrofoil validation - comparison between CFD and tunnel test.

Although, the errors both for drag and lift are relatively large, CFD results provide good engineering estimation for further design. The problem under consideration is unsteady; the cavity extended from a foil may fluctuate with specific natural frequency as the foil shed vortices into the fluid. One way to resolve this behavior is to estimate the Strouhal number of the fluctuations and then modify the time step within the simulation. Major parameter however would be a number of inner iterations as the transient response becomes important. Over prediction of the lift coefficient is due to inadequate resolving of the cavity at suction face of the foil, as presented in Figure 59. Side view of whole computation domain is presented on top part of the figure, while the lower part zooms into the region of interest. Zoomed area is indicated by rectangular box.

Additional foil simulation was executed with much finer grid of 17.5M cells. The simulation run in parallel on 96 CPU's, reaching physical time of 0.6[s]. The results were almost half on both lift and drag coefficients. $C_L = 0.144$, $C_D = 0.04$. The discrepancies between first and second hydrofoil simulation may be explained by examining the form of the cavity and the free surface. Free surface for both runs without the foil is shown in Figure 61.

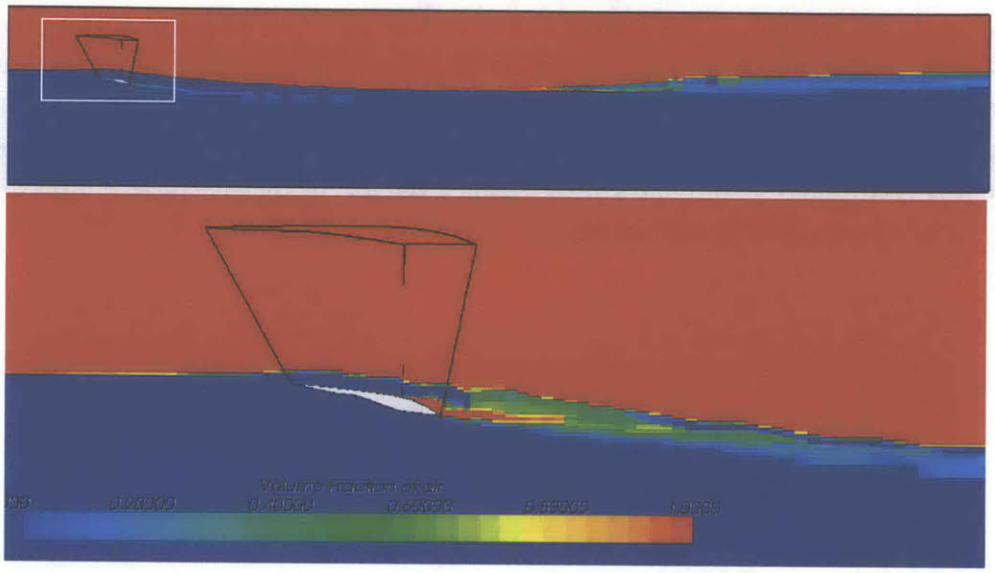

Figure 59. Hydrofoil VOF - cavity capture after 8[s] run, medium mesh.

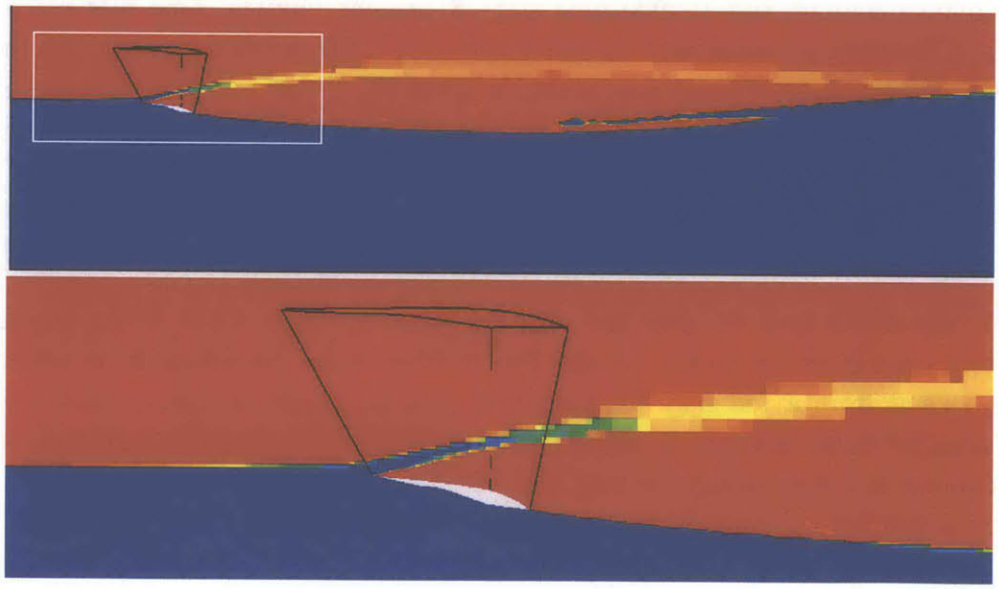

Figure 60. Hydrofoil VOF - cavity capture after 0.6[s] run, fine mesh.

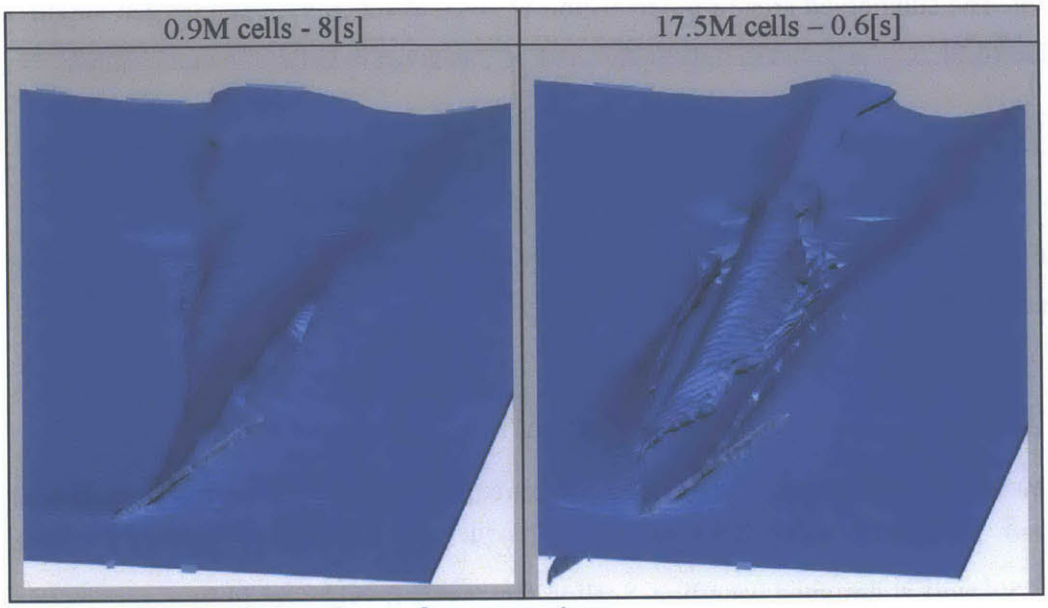

Figure 61. Hydrofoils simulation - free surface comparison.

By comparing the figures presented above it is clear that for finer mesh transient effects are still dominant. The jet generated by the foil did not collapse yet and did not reach the outlet. It is assumable that the results obtained from fine mesh simulation will be comparable to coarse mesh results and experiment after reaching larger physical time. Though, the process is computationally and time consuming. It was decided to use the medium mesh in the vicinity of the foils during integration of foils with the hull because of better agreement with the experiment and the fact that for current design phase we are interested in steady state values. It is important to notice that for maneuvering part of vessel design the transient effects of hydrofoils should be investigated.

Foil and hull integration

The main challenges in integrating the foils with the hull are the fact that the foils operate in hull's wake, the shape of the wake is unknown, the hull is inherently unstable at required trim angle. One of the major requirements of the foils is to stabilize the hull at trim angle such that sufficient lift will be generated by main wing.

The force produced by the foils depends on angle of attack α and submerged area, equation (4.2) can be rewritten

$$C_{Lf}(\alpha) = \frac{F_{lift\_foil}(\alpha)}{1/2\,\rho V^2 A_{sub}(\alpha)} \tag{4.6}$$

At current design phase we neglect the induced velocities and assume that incoming velocity is constant. The submerged area of the hydrofoil is given as function of submerged length L_{sub} by equation (4.7). L_{sub} is given in millimeters and A_{sub} is given in units of meters square.

$$A_{sub} = 0.1768\left(\frac{L_{sub}}{1000}\right)^2 + 0.0613\left(\frac{L_{sub}}{1000}\right) \tag{4.7}$$

Assuming both foils support 10% of the displacement each foil carries $5\%\Delta = 1.17[kg]$, the area required to carry the load is defined by equation (4.8)

$$A_f = \frac{1.17g}{1/2\rho V^2 C_{Lf}(0)} = 757.6[mm^2] \tag{4.8}$$

The new foil should be scaled to reflect the load requirements at zero angle of attack. Originally validated hydrofoil had designed $A_{sub} = 0.029[m^2]$ and corresponding submergence $L_{sub} \approx 250[mm]$ at designed waterline. Scaling factor is defined by eq. (4.9).

$$\lambda_f = \sqrt{\frac{A_f}{A_{sub}}} = 0.162 \tag{4.9}$$

Trim control requirements for longitudinal stability can be derived numerically. The derivation applied to main wing and foils was adopted from aerodynamics theory of stable flight. Clancy provides detailed description of the method in reference [48], chapter 16. Marchaj provides examples of foil installation on the hull in reference [49]. Assume pitch disturbance causing a change in trim angle. This trim change will affect moment equilibrium defined in(2.25). For stable ride, increase in τ (bow-up disturbance) will create bow down resulting pitching moment (wing plus foils). In the same manner decrease in τ (bow-down disturbance) will create bow up resulting pitching moment. Numerically this relation is defined by eq. (4.10)

$$\frac{\partial M}{\partial \tau} < 0 \tag{4.10}$$

Simplified free body diagram is shown in Figure 62. Wing force is applied in center of pressure of the wing. Foil forces are applied in center of pressure of the foils. Gravitational force is acting through the center of gravity. x_g denotes the distance between CG and longitudinal center of pressure on the main wing. l_{tail} is the longitudinal distance between foil and wing lifting forces.

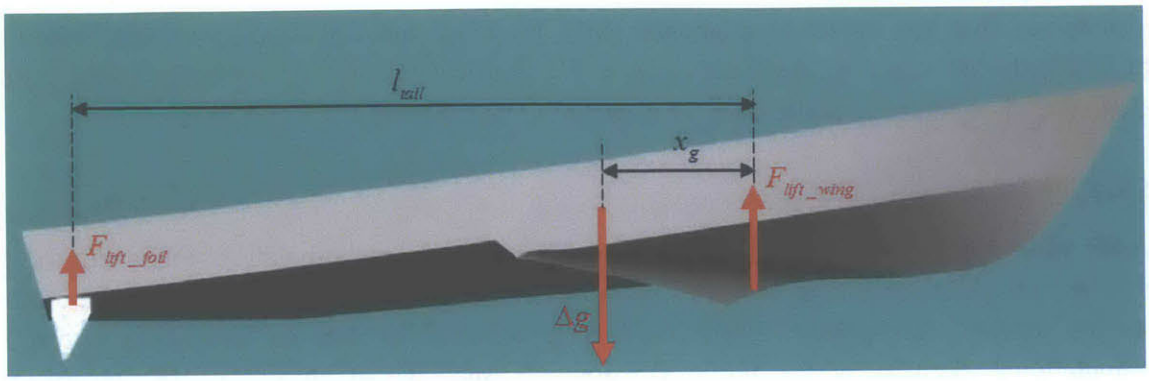

Figure 62. Longitudinal stability - aircraft theory.

Moment equilibrium about CG results:

$$M = F_{lift\_wing} x_g - \left(l_t - x_g\right) F_{lift\_foil} \tag{4.11}$$

Recalling (4.6), the forces generated by wing and foils may be expressed using wing and foils lift coefficients C_L , C_{Lf} respectively:

$$F_{lift\_wing} = \frac{1}{2}\rho V^2 A_w C_L(\tau) \;;\; F_{lift\_foil} = \frac{1}{2}\rho V^2 A_f(\tau) C_{Lf}(\tau) \tag{4.12}$$

It is important to notice that in eq. (4.12) the area of the wing represents full wing and area of the foils is given for both foils.

Incremental form of eq. (4.11) provides eq.(4.13)

$$\frac{\partial M}{\partial \tau} = x_g \frac{\partial F_{lift\_wing}}{\partial \tau} - \left(l_{tail} - x_g\right) \frac{\partial F_{lift\_foil}}{\partial \tau} \tag{4.13}$$

Pitching moment defined by equation (4.11) is often expressed as total lift force applied at some distance h ahead of CG:

$$M = h\left(F_{lift\_wing} + F_{lift\_foil}\right) \rightarrow \frac{\partial M}{\partial \tau} = h\left(\frac{\partial F_{lift\_wing}}{\partial \tau} + \frac{\partial F_{lift\_foil}}{\partial \tau}\right) \tag{4.14}$$

Equating (4.13) and (4.14) parameter h is obtained. In aircraft terminology this parameter denotes longitudinal stability static margin. For stable flight h must be negative.

$$h = x_g - l_{tail} \frac{\left(\partial F_{lift\_foil}/\partial \tau\right)}{\left(\partial F_{lift\_wing}/\partial \tau\right) + \left(\partial F_{lift\_foil}/\partial \tau\right)} \tag{4.15}$$

Considering that the vessel is supported only by wing and foil forces, aircraft theory is applicable. In order to evaluate h the slope of lift coefficients and foils submerged area should be calculated. x_g and l_{tail} are known, A_w assumed to be constant.

Foils submergence estimation

Steady wake field was extracted to STL file from previously run simulation. Fixed trim of 5° and free heave were chosen as baseline. As shown in Figure 49 the wetted portion of the bottom satisfies design requirements. Wake field is represented by free surface, it is a part of computational domain where phase fraction of water equal to phase fraction of air, $c_{water} = c_{air} = 0.5$. The flow detaches almost completely behind the wing. Longitudinal position of the wing is very close to LCG, therefore we may assume that for small perturbations in trim the shape of the wake does not change. Free surface was imported into Rhino 3D modeler and superimposed onto hull model. First the hull was rotated to 5° trim, then its longitudinal location and elevation were adjusted to comply with generated wake. Next, copy of the hull was rotated about CG to 4,3,2,1,0 degrees trim. The results are shown in Figure 63 and Figure 64.

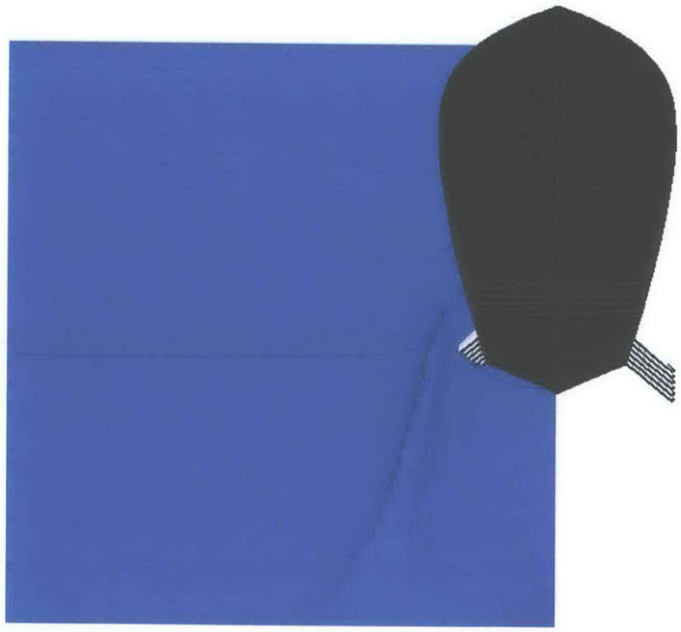

Figure 63. Wake formation behind the hull, submrged foils.

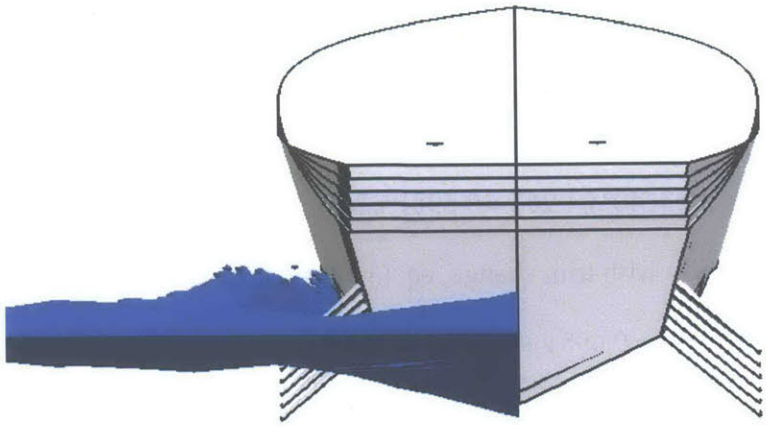

Figure 64. Foil submergence vs. trim 0-5 degrees aft view.

Upper position of the hull corresponds to $0°$ trim lower position to $5°$ trim.

The foils are longitudinally positioned at AP, therefore the vertical increment in foils position is $dz = LCG\sin(\tau)$. Special interest deserves the free surface in the longitudinal position of the foils. By cutting the free surface near AP, spline is obtained, red curve is shown in Figure 65.

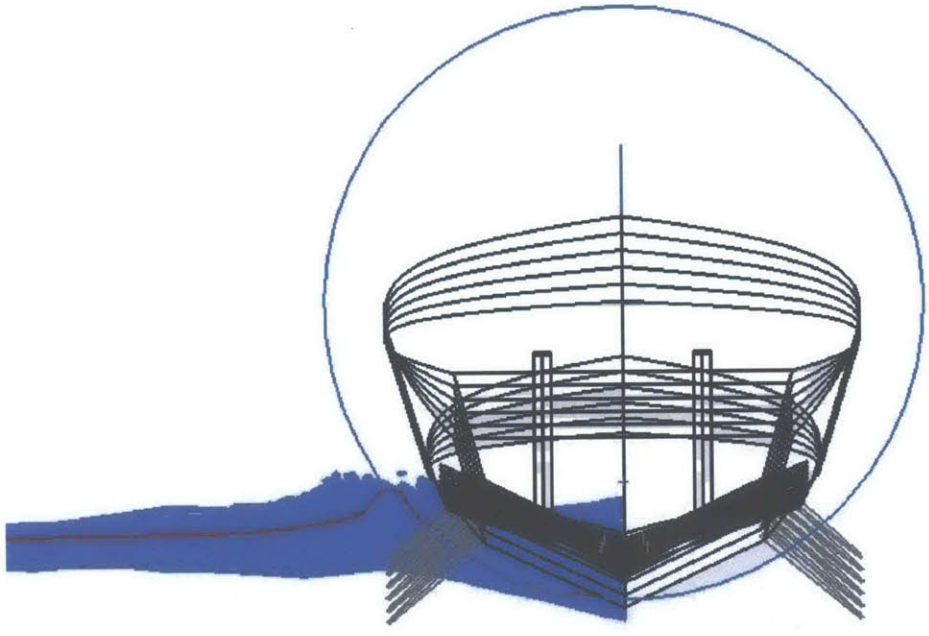

Figure 65. Shape of free surface near the foils.

The curve has circular shape in the vicinity of the foils. This circle can be numerically described by equation (4.16), all numbers in the equation are given in millimeters.

$$(z-350)^2 + y^2 = 278^2 \tag{4.16}$$

The foils have dihedral angle of $40°$, at 0 trim foils coincide with straight line analytically defined by eq. (4.17).

$$z = 40°y + 267 = 0.698y + 267 \tag{4.17}$$

Recalling that foils move vertically with trim change, eq. (4.17) in general form becomes:

$$z(\tau) = 0.698y + 267 - LCG\sin(\tau) \tag{4.18}$$

Assuming that circle position does not change with trim, MathCad solve block was used to solve the system of equations (4.18) and (4.16) with parameter τ. The solution provides coordinates of intersection point between circle (free surface) and line (foil) $-y_1(\tau), z_1(\tau)$. Transversal extent of the foils y_2 is known and it doesn't depend on trim angle. Foil is connected to hull at transversal location y_0. Substituting y_2 into (4.18) $z_2(\tau)$ is obtained. Submerged length of the hydrofoils as function of trim angle is calculated by eq.(4.19). It's important to check at this point that $|y_2| > |y_1(\tau)| > |y_0|$. If not, that means that the foil is completely out the water and $L_{sub}(\tau) = 0$, or is completely submerged, and $L_{sub}(\tau)$ should be assigned its maximum value.

$$L_{sub}(\tau) = \sqrt{\left(z_1(\tau) - z_2(\tau)\right)^2 + \left(y_1(\tau) - y_2\right)^2} \tag{4.19}$$

$L_{sub}(\tau)$ scaled by λ_f is substituted into (4.7) to obtain $A_{sub}(\tau)$ and then scaled again by λ_f^2 to obtain $A_f(\tau)$. This value is used in eq.(4.12).

Estimating lift force generated by foils

Experimental lift coefficient of the foils was plotted in Figure 57, the results may be interpolated by cubic polynomial as follows:

$$C_{Lf}(\alpha) = -10.854\alpha^3 + 6.338\alpha^2 + 2.064\alpha + 0.299 \tag{4.20}$$

In order to minimize drag at design conditions the foils will be at zero angle of attack at $\tau \approx 3.5°$, utilizing this fact and recalling $40°$ dihedral angle eq. (4.20) can be expressed in terms of τ:

$$\begin{aligned} \overline{\tau} &= (\tau - 3.5°)\cos(40°) \\ C_{Lf}(\tau) &= -10.854\overline{\tau}^3 + 6.338\overline{\tau}^2 + 2.064\overline{\tau} + 0.299 \end{aligned} \tag{4.21}$$

Substituting (4.21) into (4.12) and taking derivative with respect to τ one obtains the rate of change in foil lift forces as function of τ expressed in [kg/rad]:

$$\frac{\partial F_{lift\_foil}}{\partial \tau} = \frac{1}{2g}\rho V^2 \frac{\partial}{\partial \tau}\left(A_f(\tau)C_{Lf}(\tau)\right) \tag{4.22}$$

The equation (4.22) was numerically solved using MathCad in range $-2° \div 7°$ / $-0.035 \div 0.122[rad]$. The results are presented graphically in Figure 66.

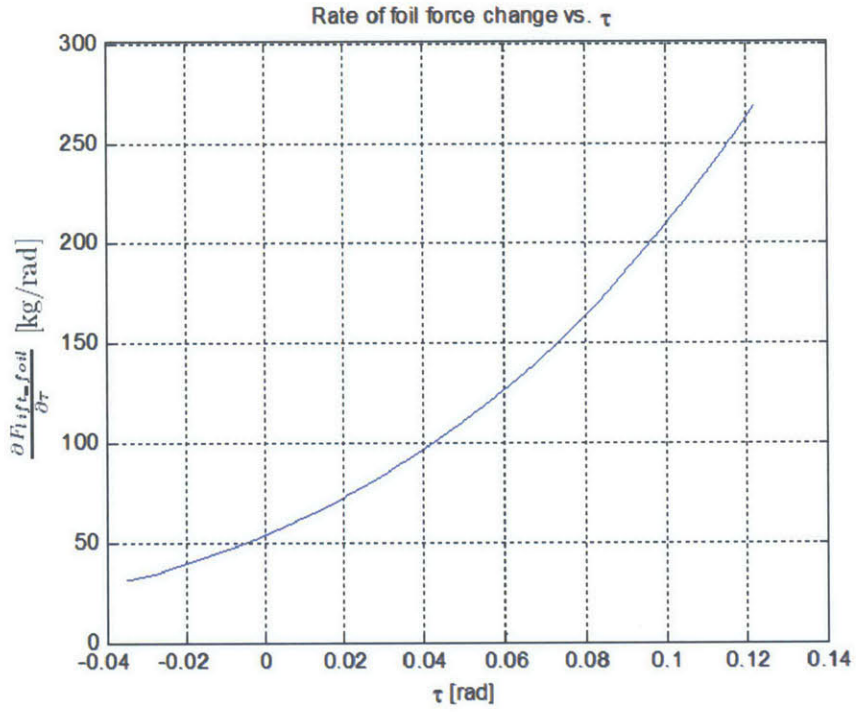

Figure 66. Rate of foil force change vs. trim angle.

Estimating lift force generated by main wing

In order to estimate the variation of lift forces produced by main wing with respect to trim angle we will proceed to analyze data obtained at exploration phase of current study. The data in Table 8 can be interpolated, as shown in Figure 67. Particular interest is the gradient of the surface with respect to τ. Numerically C_L was approximated by 2nd degree polynomial at different drafts relative to static sinkage condition, -4,0,4 [cm] , corresponding indexes 1,2,3:

$$\begin{aligned} C_{L1}(\tau) &= 2.513\tau^2 - 0.2256\tau + 0.03206 \\ C_{L2}(\tau) &= 4.053\tau^2 - 0.4046\tau + 0.02394 \\ C_{L3}(\tau) &= 0.081\tau^2 - 0.0375\tau + 0.04421 \end{aligned} \tag{4.23}$$

Substituting (4.23) into (4.12) and taking derivative with respect to τ one obtains the rate of change in wing lift forces as function of τ expressed in [kg/rad]:

$$\frac{\partial F_{lift\_wing}}{\partial \tau} = \frac{1}{2g}\rho V^2 A_w \frac{\partial}{\partial \tau}\left(C_L(\tau)\right) \tag{4.24}$$

Equation (4.24) was numerically evaluated for three drafts -4,0,4 [cm].

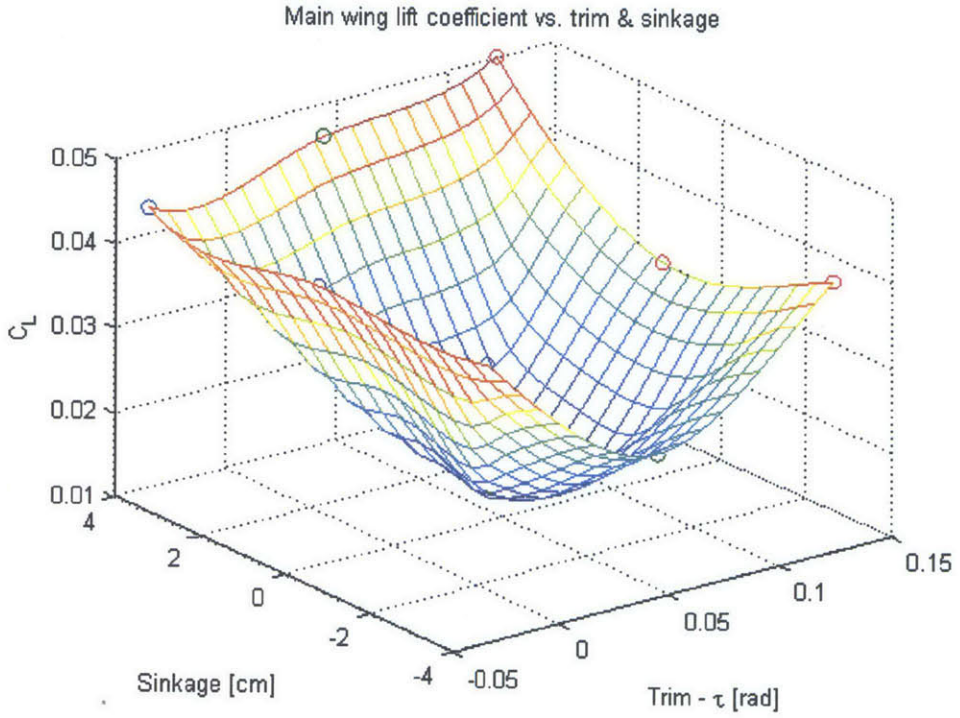

Figure 67. Main wing lift coefficient vs. trim & sinkage.

In current design $x_g = 11[cm]$ and $l_{tail} = 64.8[cm]$, the length of the foils (y_2) was chosen to be larger than A_f requirement for 5%Δ lifting force. This design margin intended to incorporate the uncertainty in real position of free surface and ensure that the foils are not emerge completely in lower trim angles. Numerical values of equation (4.24) were substituted into eq. (4.15) to obtain h parameter for three drafts. The results are shown in Figure 68. Negative values of h indicate that the design of main wing and hydrofoils is stable. It is clear that at low or negative trim angles the stability margin declines, as foils come out the water. For high CG, draft 4[cm], the stability margin grows with trim angle. After full submergence of the foils this tendency will decay.

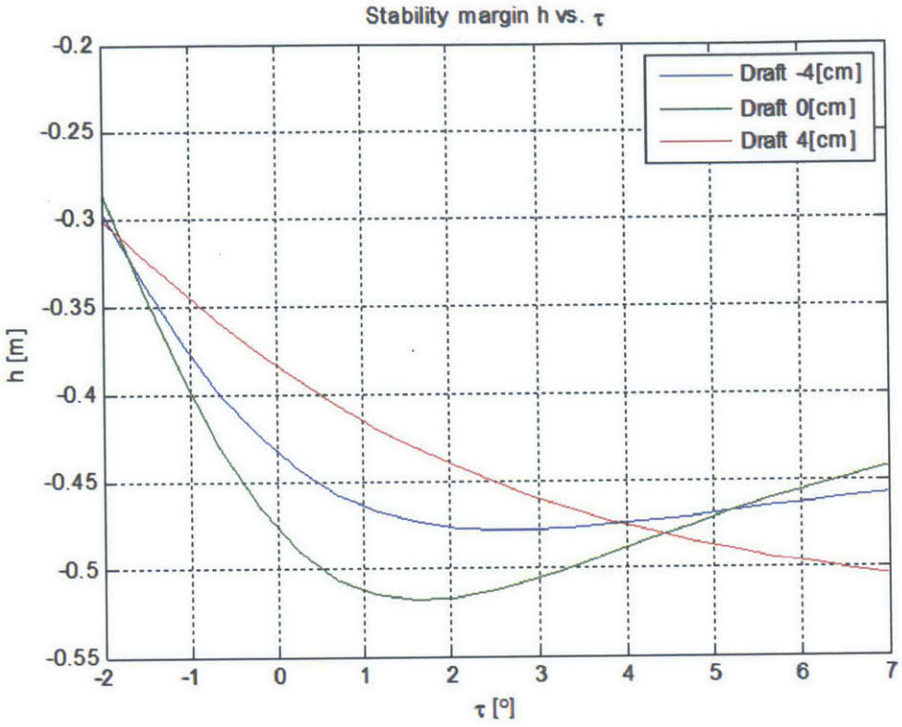

Figure 68. Stability margin h vs. trim angle.

The current approach which takes into account the rate of change of forces on main wing and foils is much more accurate in predicting the behavior of the vessel than the original method, which assumes that the vessel behaves as a beam, statically supported in two points.

Hull with hydrofoils - simulation results

Simulation of hydrofoil supported hull was performed at several configurations.

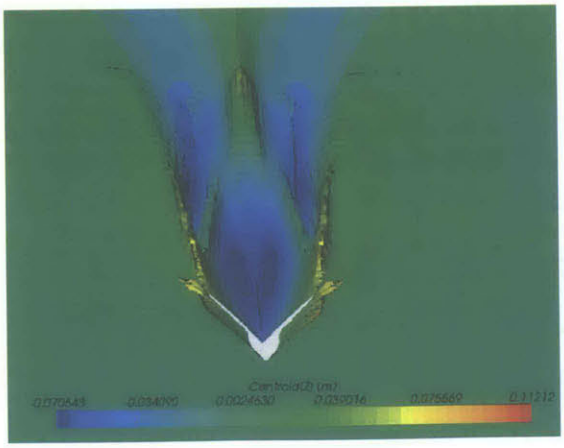

Figure 69. Free surface shape - hull with foils.

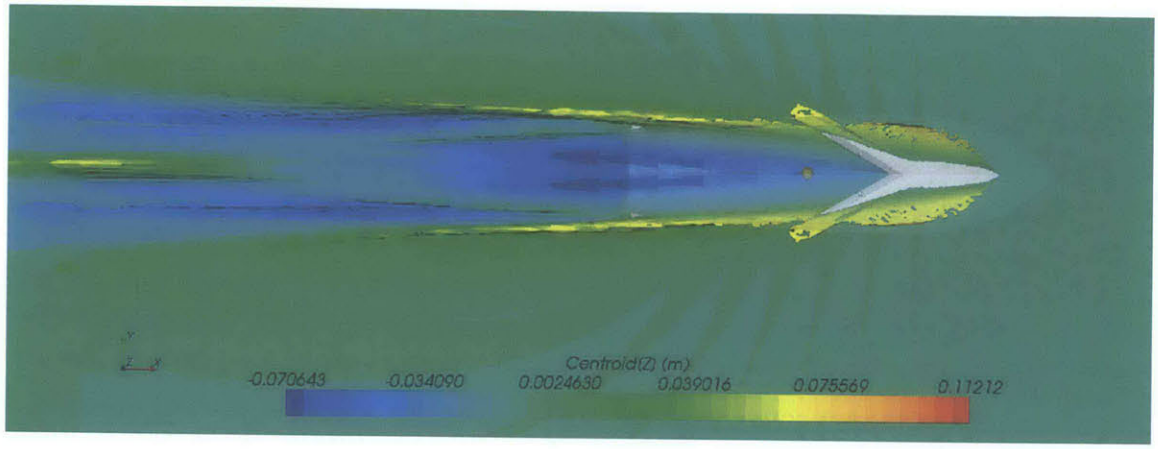

Figure 70. Hydrofoils cavity extend - top view.

Angle of attack of the hydrofoils was aligned with baseline, forward step configuration, Figure 55. Angle of attack of the hydrofoils was aligned with keel line at 3.5° trim, forward step configuration. The AoA of the hydrofoils was aligned with baseline, original step configuration Figure 32. The AoA of the hydrofoils was aligned with keel line at 3.5° trim, original step configuration.

The cavity extent behind the hull is shown in Figure 69 and Figure 70. All configurations reached steady state planing regime. Time histories of the drag forces, trim angle and sinkage are presented in Figure 71 and Figure 72. The vertical axis in Figure 71 is given in units of Newton. The final results were obtained by time averaging the values presented in Figure 71, Figure 72 over the last two seconds of the simulation.

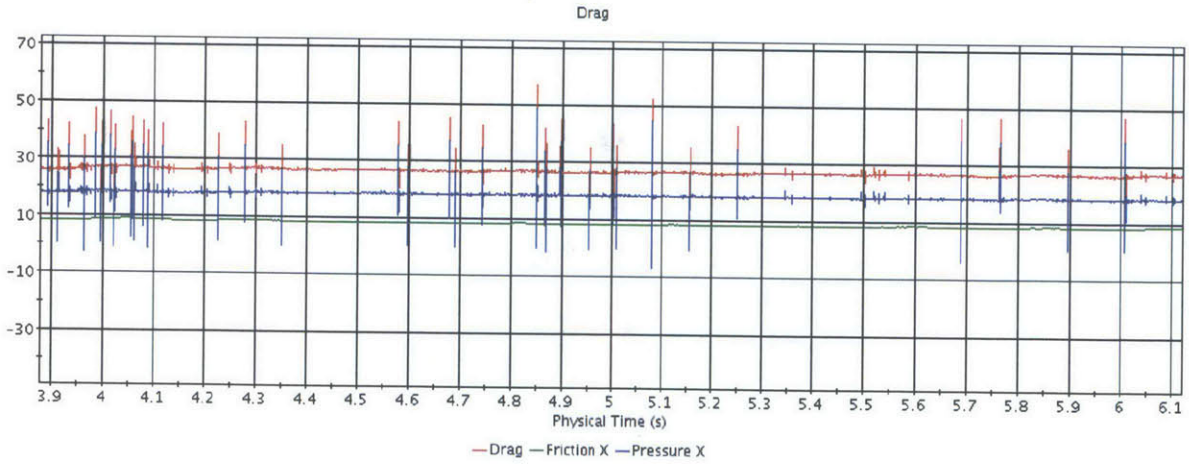

Figure 71. Time history of the Drag forces (Pressure drag, Friction Drag, Total Drag).

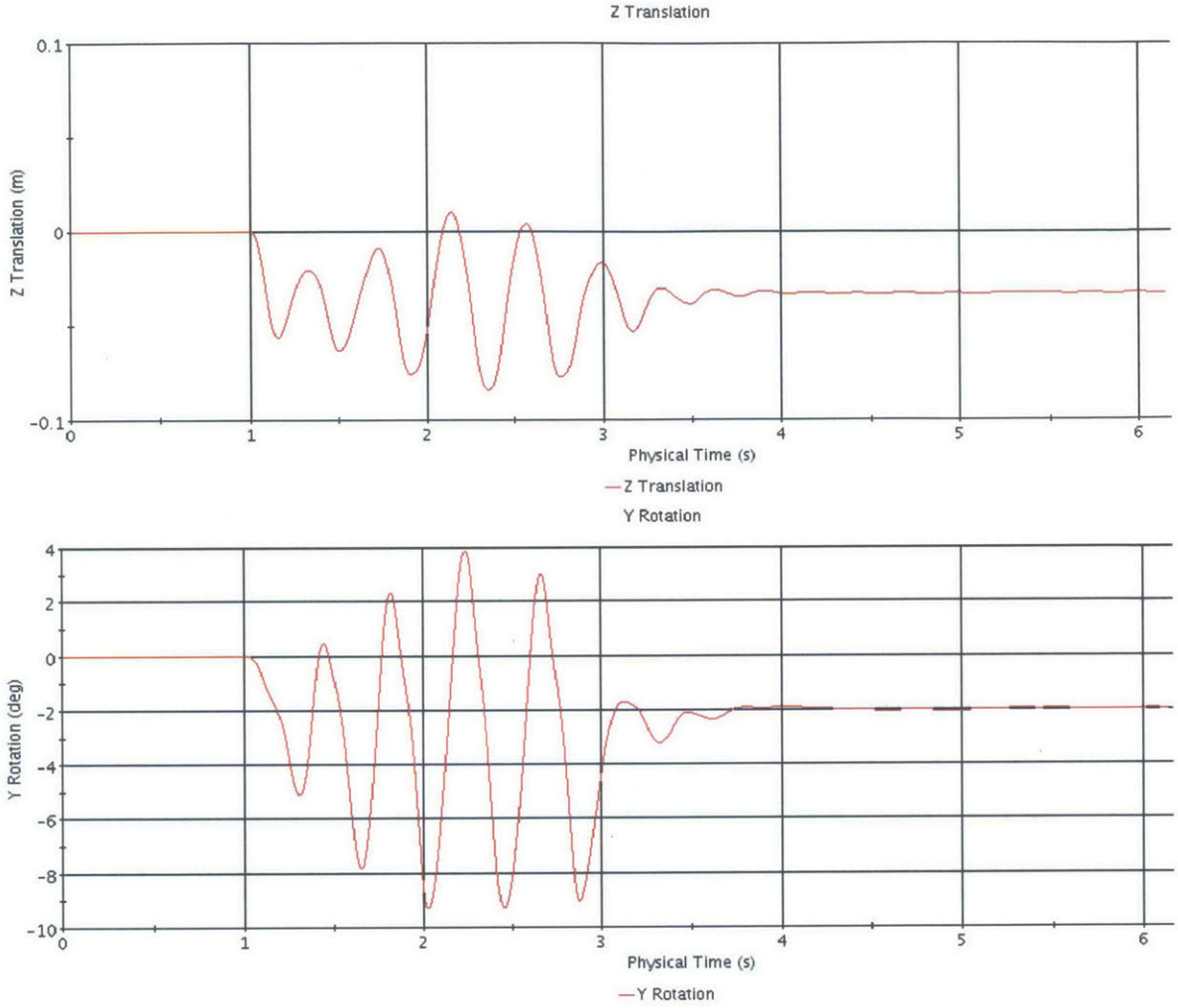

Figure 72. Time history of the sinkage & trim.

The hull was released after 1[s] of simulation in order to achieve developed flow around the body, before activating rigid body solver. Artificial damping force was activated between 2.5[s] and 3.5[s] to enhance the convergence to a steady state.

Transparent silhouette in Figure 70 indicates the position of the hull relative to wake. Sharp wedge on the free surface indicates the portion of the hull in contact with water. Figure 70 shows forward step configuration.

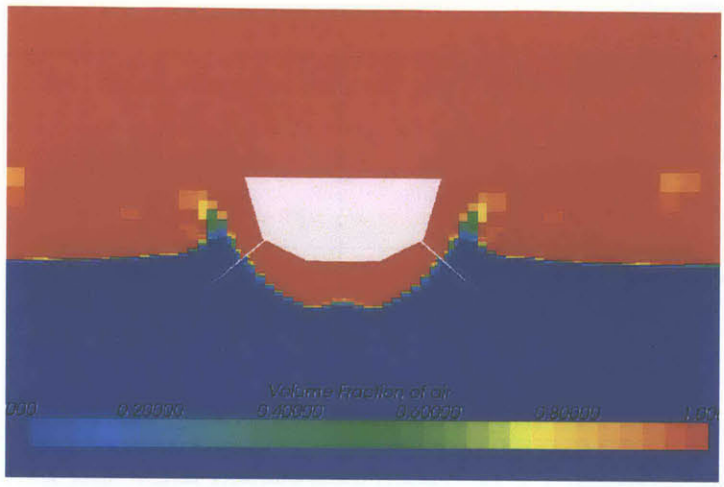

Figure 73. Steady state foils submergence, transverse cut.

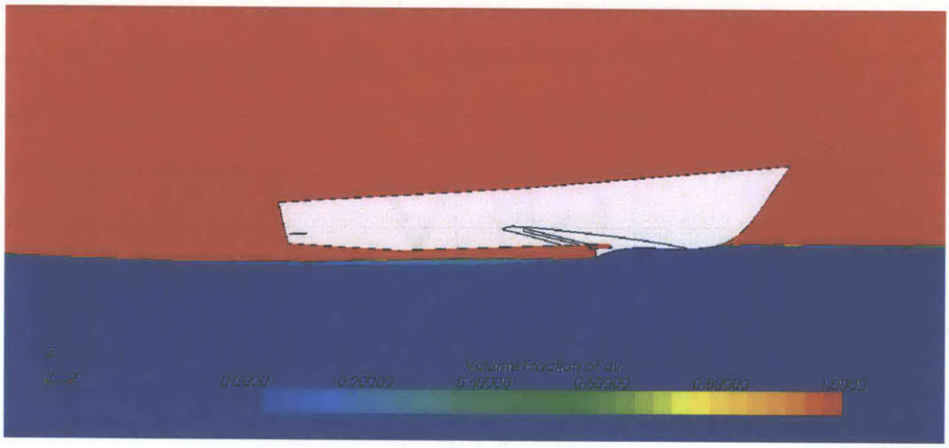

Figure 74. Ventilated body foil supported, forward step.

Although forward wing position allows better match of the stagnation line with the wing, as can be seen in Figure 70, the separation of spray root from the body is not sharp. When the wing is too close to the bow constant deadrise is not maintained, and spray climbs up the bow. The overall drag reduction in this case relative to validation case - I was only 3%. Figure 71 and Figure 72 shows complete separation of the flow behind the wing. The foils operate within the wake according to design. In Figure 75 pressure and shear forces distribution are shown (right part of the figure). The stagnation line matches wing position. Front part of the pressure side of the foil produces the majority of the lift, as designed. The wetted area of the hull is relatively small (left part of Figure 75). The equilibrium trim angle strongly depends on angle of attack of the hydrofoils relative to the hull. Thus, when foils were installed aligned with keel trim of 1.3° was achieved. In case with inclined foils steady state trim was 2°. This trim is lower than designed 3.5° due to the design margin in A_f. This margin was taken to incorporate the uncertainty in actual free surface location.

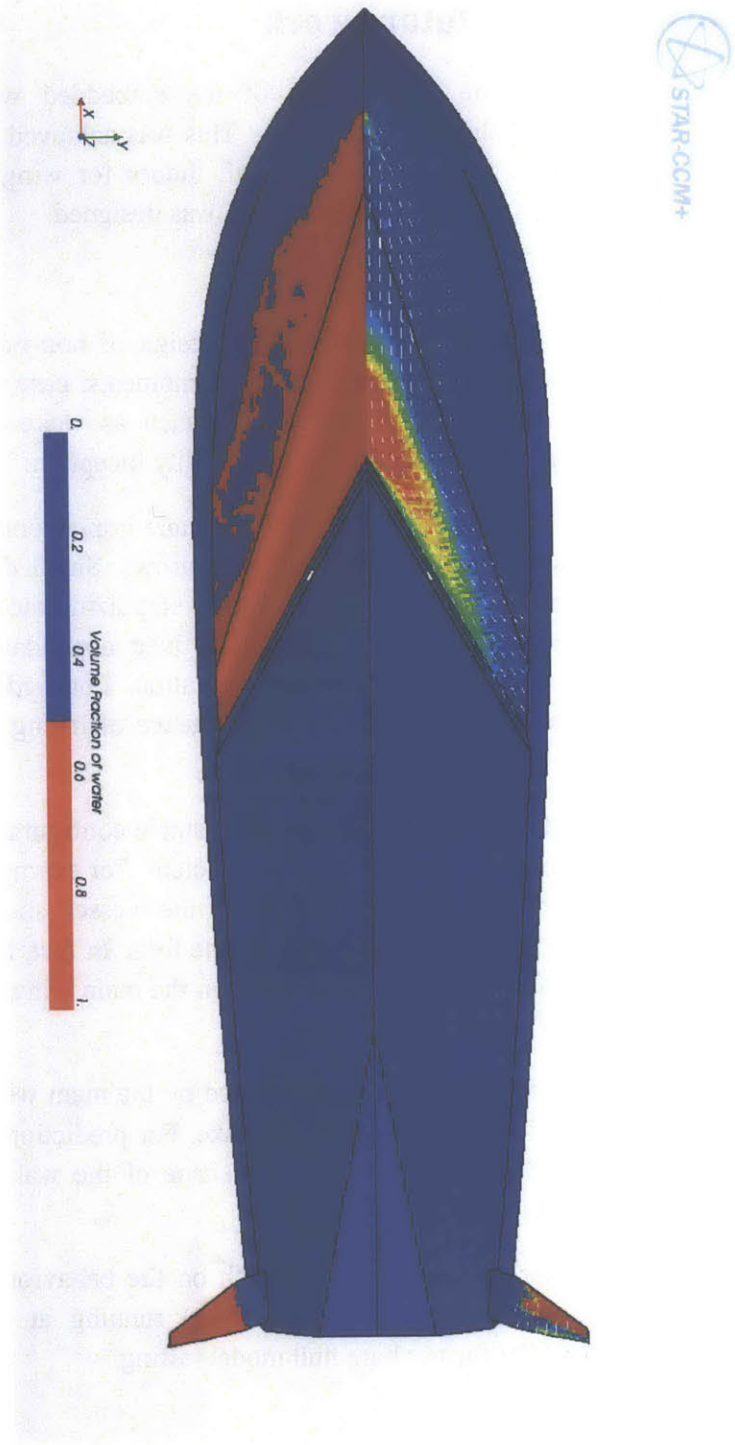

Figure 75. Pressure, Shear forces and VOF distribution on the bottom of modified hull.

Chapter 5 - Conclusions and future work

The current research demonstrated the applicability of the embedded wing (Dynaplane configuration) on deep-V hull as a method to reduce drag. This was achieved using a RANSE CFD solver, 3D CAD modeler in conjunction with aircraft theory for wing/tail stability. A dynamically stable configuration with reduced Lift/Drag ratio was designed.

The current research work emphasized the following points:

A RANSE CFD solver is a major tool for preliminary design of non-traditional planing seagoing vessels. Beyond pressure distribution, forces and moments, case studies based on properly validated numerical setup provide information such as wake geometry, exact position of stagnation line, spray separation, dynamic instability inception.

Dynamic instabilities in pitch are major limiters for Dynaplane implementation on deep-V planing hulls. As speed increases, inception to porpoising grows. Small disturbances may drive the vessel into resonant oscillations; therefore a robust stabilizing mechanism for trim control is essential. Although the mechanism may be a fixed appendage, it should be responsive to a wide range of trim angles without saturation. For hydrofoils cause of saturated response can be complete emergence or submergence of lifting surface, or stall angle of attack.

Through the research process, it became obvious that for a stable configuration of wing and foils, static considerations for load distribution are not sufficient. For example, the guidance provided by the baseline method suggested designing the vessel such that 90% of displacement load will be taken by the wing and 10% by the foils. In fact, beyond the static considerations, rate of change of forces due to trim angle on the main wing and foils should be considered.

At design speed, the hydrofoils operate in the wake created by the main wing, and the foils submerged length depends heavily on the shape of the wake. For prediction of running trim angle and load distribution on the wing and foils, the shape of the wake should not be neglected.

The numerical data collected during the current research on the behavior of deep-V hull with embedded wing and foils (Dynaplane configuration) running at design speed is sufficient to produce a prototype for further bare hull model testing.

Future research perspectives:

Proximity of lifting surfaces to sea level introduces strong nonlinearity in generated forces. The area of lifting surfaces is small relative to conventional planing craft, rapid changes of submerged area can contribute to instability of the vessel. In particular, as part of future

work the influence of incoming waves must be studied. Transient effects of hydrofoils must be examined, as the development of the cavity behind the foils is not a steady process. This phenomenon may influence the maneuvering qualities of the vessel. Due to a high non linearity of the problem robustness to initial conditions should be studied more extensively.

Another important aspect of vessel development would be attachment and simulation of the propulsor. Change of the thrust line according to type and position of the propulsor should be incorporated in the design and performance prediction. The influence of the propulsor on wake generation should also be investigated as part of further development. Complementary study of a vessel's behavior in off-design condition should be performed. It is assumed that the vessel will operate at top speed only for a small amount of time, while the majority of time will be spent at cruise speed.

A less acute but still significant part of further development would be structural analysis with emphasis on the appendages. A major concern in hydrofoils is a supercavitating profile with very thin leading edge. Due to the fluctuating nature of the loadings structural strength of the foils needs to be investigated. Typical propeller material may be used for prototyping the foils such as NiBrAl casting into a 3D printed mold.

In the current work, the design of ventilation duct was simplified and limited to providing necessary ventilation by equating the pressures on deck and beneath the bottom. As a future development, the shape of the duct may be modified to achieve smooth flow, reduced head losses in pipe bends and reduced noise.

Bibliography

[1] D. L. Blount, "Achievements with Advanced Craft," *Naval Engineer Journal,* vol. 09, pp. 49-59, 1994.

[2] J. N. Newman, Marine Hydrodynamics, Cambridge MA: MIT Press, 1977.

[3] K. W. Eggers, S. D. Sharma and L. W. Ward, "An assessment of some experimental methods for determining the wavemaking characteristics of a ship form," *SNAME Transactions,* vol. 75, pp. 112-157, 1967.

[4] M. Rabaud and F. Moisy, "Ship wakes: Kelvin or mach angle," *Physical Review Letters,* vol. 110, no. 21, 2013.

[5] T. Gillmer and B. Johnson, Introduction to Naval Architecture, Annapolis: US Naval Institute Press, 1982.

[6] S. W. Barnaby, "Note on the cavitation of screw propultion," *Minutes of the Proceedings,* vol. 165, pp. 299-308, 1906.

[7] D. Savitsky, "Planing craft," *Naval Engineers Journal,* vol. 2, pp. 113-141, 1985.

[8] E. P. Clement and J. G. J. Koelbel, "Progress during the past century toward the developemnt of efficient load carrying, stepped planing boats," in *SNAME Fifth Biennal Power Boat Symposium*, New Jersey City, 1993.

[9] J. Plum, "Automatic Stabilizer for Watercraft". US, Washington D.C. Patent 3260229, 25 Feb 1965.

[10] D. Savitsky and J. A. White, "Seakeeping Prediction of USCG Hard Chine Patrol Boat," *SNAME New York Metropolitan Section* , vol. 463, pp. 1-59, 1988.

[11] D. Savitsky, "The effect of bottom warp on the performance of planing hulls," in *The Third Chesapeake Power Boat Symposium*, Annapolis, 2012.

[12] J. C. Rose and C. F. Kruppa, "Methodical Series Model Test Results," in *FAST - Fast Sea Transportation*, Trondheim Norway, 1991.

[13] J. Allison, "Marine Waterjet Propulsion," *SNAME Transactions,* vol. 101, pp. 275-335, 1993.

[14] D. Savitsky and J. Gore, "Re-evaluation of planing hull form," *Journal of Hydronautics,* vol. 14, no. 2, pp. 34-47, 1980.

[15] R. McLeavy, Naval Fast Strike Craft and Patrol Boats, Poole UK: Blandford Press, 1979.

[16] Jane's Information Group, Jane's high-speed marine transportation, Coulsdon, Surrey, UK: Jane's Information Group, 2011.

[17] D. Savitsky, "Hydrodynamic design of planing hulls," *Marine Technology,* vol. 1, no. 1, pp. 71-95, 1964.

[18] J. B. Hadler, "Prediction of power performance on planing craft," *Society of Naval Architects and Marine Engineers -- Papers,* vol. 74, no. SNAME Meeting, pp. 563-610, 1966.

[19] D. L. Blount, "Resistance characteristics of 70 foot hydrofoil missile range patrol boat," DTMB Report 1607, Bethesda, Maryland, 1962.

[20] E. P. Clement and D. L. Blount, "Resistance tests of systematic series of planing hull forms," in *SNAME Transactions*, New York, Nov 14-15 1963.

[21] K. Garme and A. Rosen, "Time domain simulations and full scale trials of planing hulls in waves," *Int. Shipbuild. Progr., 50, no. 3,* pp. 177-208, 2003.

[22] J. A. Keuning and J. Gerritsma, "Resistance tests of series of planing hull forms with 25 degrees deadrise angle," *International Shipbuilding Progress,* pp. 222-249, 1982.

[23] B. R. Savander, "Design & Analysis of Integrated Propulsion Systems for High-Speed Craft," in *Chesapeake Power Boat Symposium*, New York, 2008.

[24] B. Friedhoff, R. Henn, T. Jiang and N. Stuntz, "Investigation of planing craft in shallow water," in *9th International Conference on Fast Sea Transportation, FAST*, Shanghai, China, 2007.

[25] A. S. Perelmutr, "Materials for design high speed planing craft (In Russian)," *TsAGI Transactions n.554,* pp. 5-62, 1953.

[26] E. P. Clement and J. G. Hoyt, "A Parametric Study of Dynaplane-Type Planing Motorboats," in *The first Chesapeake power boat symposium*, Annapolis, Maryland, 2008.

[27] L. Larsson and H. Raven, Ship Resistance and Flow PNA Series, New Jersey: SNAME, 2010.

[28] L. Larsson and R. E. Eliasson, Principles of Yacht Design, London: Adlard Coles Nautical, 2000.

[29] S. V. Patankar, Numerical Heat Transfer and Fluid Flow, Taylor & Francis, 1980.

[30] H. K. Versteeg and W. Malalasekera, Finite Volume Method, Harlow: Longman Group, 1995.

[31] H. Tennekes and J. L. Lumley, The first course in turbulence, Cambridge: MIT Press, 1970.

[32] D. C. Wilcox, Turbulence modeling for CFD, La Canada: DCW Industries Inc, 1994.

[33] S. B. Pope, Turbulent flows, Cambridge: Cambridge university press, 2000.

[34] P. Spalart and C. L. Rumsey, "Effective inflow conditions for turbulence models," *AIAA Journal,* vol. 45, no. 10, pp. 2545-2553, 2007.

[35] T. H. Shih, J. Zhu and J. L. Lumley, "A new Reynolds stress algebraic equation model," *Computational methods in applied mechanics and engineering,* vol. 125, pp. 287-302, 1995.

[36] T. H. Shih, W. W. Liou, A. Shabbir, Z. Yang and J. Zhu, "A new k-epsilon viscosity model for high reynolds number turbulent flow," *Computers Fluid,* vol. 24, no. 3, pp. 227-238, 1995.

[37] D. A. Anderson, J. C. Tannehill and R. H. Pletcher, Computational fluid mechanics and heat transfer, Washington DC: Hemisphere Publishing Taylor & Francis, 1997.

[38] M. Peric and S. Muzaferija, "Computation of free surface flows using interface tracking and interface capturing methods.," in *Nonlinear Water Wave Interaction*, Southhampton, Computational Mechanics Publications, 1998, p. Chap. 2.

[39] J. Gerritsma, "Shipbuilding laboratory of Delft university of technology," *International Shipbuilding Progress,* vol. 4, no. 30, pp. 61-72, 1957.

[40] D. Savitsky and W. Brown, "Procedures for hydrodynamic evaluation of planing hulls in smooth and rough water," *Marine Technology,* pp. 381-400, October 1976.

[41] E. P. Clement, How to design efficient planing boat - Dynaplane Boat, Asheville, NC: Clement, 2006.

[42] E. P. Clement and J. D. Pope, "Stepless and stepped planning hulls - graphs for performance prediction and design. DTMB Report 1490," David Taylor Model Basin, Bethesda MD, 1961.

[43] S. F. Hoerner, Fluid Dynamic Lift, Vancouver: Hoerner Fluid Dynamics, 1985.

[44] V. E. Johnson, "Theoretical and Experimental Investigation of Supercavitating Hydrofoils Operating near Free Surface TR-43," NASA Technical Reports, Washington D.C., 1961.

[45] T. Celano, "The Prediction of Porpoising Inception for Modern Planing Craft," *SNAME Transactions,* vol. 106, pp. 269-292, 1998.

[46] V. E. Johnson, "Theoretical and experimental investigation of supercavitating hydrofoils operating near the free water surface.TR R-93," NASA, Langley Field. VA, 1961.

[47] S. Brizzolara and C. Chryssostomidis, "The Second Generation of Unmanned Surface Vehicles: Design Features and Performance Predictions by Numerical Simulations," in *ASNE Day 2013, "Engineering America's Maritime Dominance"*, Arlington, VA, 2013.

[48] L. J. Clancy, Aerodynamics, London: Pitman Publishing Limited, 1975.

[49] C. A. Marchaj, Aero-Hydrodynamics of sailing, New York: Dodd, Mead & Company, 1980.

Appendix

```
// STAR-CCM+ macro: new_vent.java
// Written by Zvi Sheingart STAR version 8.04.007

package macro;
import java.util.*;
import star.common.*;
import star.base.neo.*;
import star.vis.*;
import star.meshing.*;

public class new_vent extends StarMacro {

    public void execute() {
        execute0();
    }

    private void execute0() {

// Create empty array of 9 Simulations

         Simulation[] mysim = new Simulation[9];
         int ct = 0;

// Create draft array and trim array

         double[] mydraft = {-0.04, 0.0, 0.04};
         double[] mytrim = {-0.07, -0.087, -0.157};

for (int i = 0; i < 3; i++) {
    for (int j = 0; j < 3; j++) {

// Continue from existing simulation
mysim[ct]= new Simulation(resolvePath(".\\188_v3_vent_Fr6.sim"));
        setActiveSimulation(mysim[ct]);
        Units units_0 = mysim[ct].getUnitsManager().getPreferredUnits(new
IntVector(new int[]{0, 0, 0, 0, 0, 0, 0, 1, 0, 0, 0, 0, 0, 0, 0, 0, 0, 0,
0, 0, 0, 0, 0}));
        Units units_1 =
mysim[ct].getUnitsManager().getPreferredUnits(new IntVector(new int[]{0, 1,
0, 0, 0, 0, 0, 0, 0, 0, 0, 0, 0, 0, 0, 0, 0, 0, 0, 0, 0, 0, 0}));



        LeafMeshPart leafMeshPart_0 =
//Get the hull part:
                ((LeafMeshPart)
mysim[ct].get(SimulationPartManager.class).getPart("hull_vent"));

        LabCoordinateSystem labCoordinateSystem_0 =
mysim[ct].getCoordinateSystemManager().getLabCoordinateSystem();
```

```
        CartesianCoordinateSystem cartesianCoordinateSystem_0 =

                ((CartesianCoordinateSystem)
labCoordinateSystem_0.getLocalCoordinateSystemManager().getObject("Boat-
CSys"));

        MeshActionManager meshActionManager_0 =
mysim[ct].get(MeshActionManager.class);

//Get the domain part (block):

        SimpleBlockPart simpleBlockPart_0 =
        ((SimpleBlockPart)
mysim[ct].get(SimulationPartManager.class).getPart("Block"));

        LeafMeshPart leafMeshPart_2 =

//Assuming the file already have block minus hull and BC set:

                ((LeafMeshPart)
mysim[ct].get(SimulationPartManager.class).getPart("Subtract"));

/*Rotate and translate */
          mysim[ct].get(SimulationPartManager.class).rotateParts(new
NeoObjectVector(new Object[]{leafMeshPart_0}), new DoubleVector(new
double[]{0.0, 1.0, 0.0}), new NeoObjectVector(new Object[]{units_1, units_1,
units_1}), mytrim[i - 1], cartesianCoordinateSystem_0);
                mysim[ct].get(SimulationPartManager.class).translateParts(new
NeoObjectVector(new Object[]{leafMeshPart_0}), new DoubleVector(new
double[]{0.0, 0.0, mydraft[j - 1]}), new NeoObjectVector(new
Object[]{units_1, units_1, units_1}), labCoordinateSystem_0);

//Execute Boolean between the domain and the hull:
LeafMeshPart leafMeshPart_1 =                          (LeafMeshPart)
meshActionManager_0.subtractParts(new NeoObjectVector(new
Object[]{simpleBlockPart_0, leafMeshPart_0}), simpleBlockPart_0, "Discrete");

                PartSurface partSurface_0 =
leafMeshPart_1.getPartSurfaceManager().getPartSurface("Block Surface");

//Create new boundary conditions for the subtracted part:
leafMeshPart_1.getPartSurfaceManager().splitPartSurfacesByAngle(new
NeoObjectVector(new Object[]{partSurface_0}), 89.0);

                PartSurface partSurface_1 =
leafMeshPart_1.getPartSurfaceManager().getPartSurface("Faces");

                PartRepresentation partRepresentation_0 =
((PartRepresentation)
mysim[ct].getRepresentationManager().getObject("Geometry"));

//Extract the wing surface as new Boundary, replace 1247 face by //the face
of interest in your model, (fins/foils/props) check //face number before
```

running the macro

```
leafMeshPart_1.splitPartSurfaceByPatch(partSurface_1, new IntVector(new
int[]{1247}), "wing");
```

//Define new boundaries

```
                partSurface_1.setPresentationName("hull");
                partSurface_0.setPresentationName("outlet");
                PartSurface partSurface_2 =
leafMeshPart_1.getPartSurfaceManager().getPartSurface("Block Surface 2");

                partSurface_2.setPresentationName("symmetry");

                PartSurface partSurface_3 =
leafMeshPart_1.getPartSurfaceManager().getPartSurface("Block Surface 3");

                partSurface_3.setPresentationName("bottom");

                PartSurface partSurface_4 =
leafMeshPart_1.getPartSurfaceManager().getPartSurface("Block Surface 4");



                partSurface_4.setPresentationName("side");
                PartSurface partSurface_5 =
leafMeshPart_1.getPartSurfaceManager().getPartSurface("Block Surface 5");
                partSurface_5.setPresentationName("top");
                PartSurface partSurface_6 =
leafMeshPart_1.getPartSurfaceManager().getPartSurface("Block Surface 6");
                partSurface_6.setPresentationName("inlet");
                PartSurface partSurface_7 =
leafMeshPart_1.getPartSurfaceManager().getPartSurface("venta");

                RootDescriptionSource rootDescriptionSource_0
=((RootDescriptionSource)
mysim[ct].get(SimulationMeshPartDescriptionSourceManager.class).getObject("Ro
ot"));
```

//Export new subtract part to separate dbs file:

```
rootDescriptionSource_0.exportDbsPartDescriptions(new NeoObjectVector(new
Object[]{leafMeshPart_1}), resolvePath(".\\sub_vent.dbs"), 1, "sub_vent");
```

//Delete new subtract part from simulation tree:

```
mysim[ct].get(SimulationPartManager.class).removeParts(new
NeoObjectVector(new Object[]{leafMeshPart_1}));
```

//Reimport method (replace part) allows to replace geometry //keeping all BC definition in Region Section intact. The linkage //is done by name.

```
PartImportManager partImportManager_0 =
mysim[ct].get(PartImportManager.class);
```

```
partImportManager_0.reimportDbsPart(leafMeshPart_2,
resolvePath(".\\sub_vent.dbs"), units_1, true, 1);

//Restore the initial position of the hull before starting next //iteration,
this is done in order not to deal with increments //within the loops->
translate and rotate back.

mysim[ct].get(SimulationPartManager.class).translateParts(new
NeoObjectVector(new Object[]{leafMeshPart_0}), new DoubleVector(new
double[]{0.0, 0.0, -1 * mydraft[j - 1]}), new NeoObjectVector(new
Object[]{units_1, units_1, units_1}), labCoordinateSystem_0);
mysim[ct].get(SimulationPartManager.class).rotateParts(new
NeoObjectVector(new Object[]{leafMeshPart_0}), new DoubleVector(new
double[]{0.0, -1.0, 0.0}), new NeoObjectVector(new Object[]{units_1, units_1,
units_1}), mytrim[i - 1], cartesianCoordinateSystem_0);

//Create output file of the 3x3 matrix:

                mysim[ct].saveState(resolvePath(".\\188_v3_vent_" + i + j +
"Fr6.sim"));

//Kill current simulation:

                mysim[ct].kill();

//Advance the counter within simulation array:

                ct = ct+1;
            }
        }
    }
}
```